Design and Optimization of Phononic Crystals and Metamaterials for Flow Control and Other Applications

by

Osama R. Bilal

B.S., Cairo University, 2006

M.S., Cairo University , 2010

A thesis submitted to the

Faculty of the Graduate School of the

University of Colorado in partial fulfillment

of the requirements for the degree of

Doctor of Philosophy

Department of Aerospace Engineering Sciences

2015

This thesis entitled:
Design and Optimization of Phononic Crystals and Metamaterials for Flow Control and Other
Applications
written by Osama R. Bilal
has been approved for the Department of Aerospace Engineering Sciences

_____

Prof. Mahmoud I. Hussein (Chair)

_____

Prof. Sedat Biringen (Co-chair)

_____

Prof. Carlos Felippa

_____

Prof. Kurt Maute

_____

Prof. Todd Murray

Date _____

The final copy of this thesis has been examined by the signatories, and we find that both the
content and the form meet acceptable presentation standards of scholarly work in the above
mentioned discipline.

Bilal, Osama R. (Ph.D., Aerospace Engineering Sciences)

Design and Optimization of Phononic Crystals and Metamaterials for Flow Control and Other
    Applications

Thesis directed by Prof. Mahmoud I. Hussein (Chair)

Transmission of everyday sound and heat can be traced back to a physical particle, or wave, called a "phonon". Understanding, analyzing and manipulating phonons across multiple scales/disciplines can be achieved using phononic materials. That is a class of material systems featuring a basic pattern that repeats spatially. Among many qualities, it exhibits distinct frequency characteristics such as band gaps, where vibrational waves of certain frequencies are prohibited from propagation. These properties can benefit a multitude of applications, ranging from vibration isolation and converting waste heat into electricity to exotic concepts like acoustic cloaking. Using unit-cell design and optimization, phononic materials/devices with extraordinary properties may be realized. Since many of these applications are based on band-gap utilization, a critical design objective is to widen band-gap size or precisely synthesize its characteristics. Approaching this problem at the unit cell level is advantageous in many aspects, mostly because it provides a complete picture of the intrinsic local dynamics which is often obscured when analyzing the structure as a whole. Moreover, it is computationally less expensive than designing an entire structure. Unit-cell dispersion engineering is also scale independent; an optimized unit cell may be used to manipulate waves ranging from a few Hz to GHz, or higher, with proper scaling. In order to keep the structure/device size as small as possible, the band-gap central frequency is tuned to be as low as possible.

The objective of this thesis is to explore and advance unit-cell design and optimization of phononic materials in one, two and three-dimensions for a broad range of applications. In particular, an application for flow control is investigated where a phononic material is shown to manipulate and alter a flow field in a favorable manner. Results involving unit-cell design and coupled fluid-

structure simulations (as part of a collaborative project) are presented and analyzed. The potential impact for a passive, inexpensive and practical technology for flow control is substantial. It can facilitate the delay/advancement of transition, prevention/provocation of separation and the suppression/enhancement of turbulence. A successful control scheme for one or more of these three flow phenomena will lead to drag reduction, lift enhancement, mixing augmentation and noise suppression, among other beneficial functions.

Dedication

To my mother who taught me why and how to learn.

Acknowledgements

Contents

Chapter

Tables

Table

Figures

Chapter 1

Introduction

One main measure of advancement of the human race is the ability to understand, control and manipulate matter. This motivates the classification of historical periods according to the usage of natural materials in daily activities (i.e., stone, bronze, iron, and silicon ages). In order to predict what is next, we should have a closer look at where we stand now. Most of the technological breakthroughs that emerged in the last century were results of our understanding of and ability to control two main fundamental particles: electrons and photons. The manipulation of electrons in semi-conductors enabled the existence of laptops and cell phones, while controlling photons with fiber optics and more recently with photonic materials/crystals permitted a wide range of applications from the internet to wireless technology. A more recent trend with tremendous potential is related to the utilization of yet another atomic-scale particle or wave, namely the phonon, using *phononic materials* [1]. Numerous studies have investigated phononic materials as cloaks for submarines, efficient thermoelectrics, thermally insulated buildings, and protection from environmental noise and earthquakes, to name a few applications [2].

1.1 Phononic materials

Phononic materials are periodic systems composed of a basic building block, the unit cell, that repeats in space. These materials exhibit distinct frequency characteristics, band gaps, which are frequency ranges where elastic/acoustic waves are prohibited from propagation. Phononic materials can be further divided into two subcategories based on the band-gap formation mechanism,

phononic crystals (PnC) and acoustic metamaterials[1] (AMs). Wave attenuation in PnCs is a result of Bragg scattering (i.e., scattering due to periodicity). For AMs, band gaps exist due to the local resonance phenomena. Owing to the different physics of band gap creation, the ratio between unit cell size and affected wavelength is different for each category. AMs with subwavelength resonances can attenuate waves with wavelength orders of magnitude larger than the unit cell size, while PnCs have unit cells on the same order as the targeted wavelength.

	1D	2D	3D
Phononic Crystals			
Metamaterial			
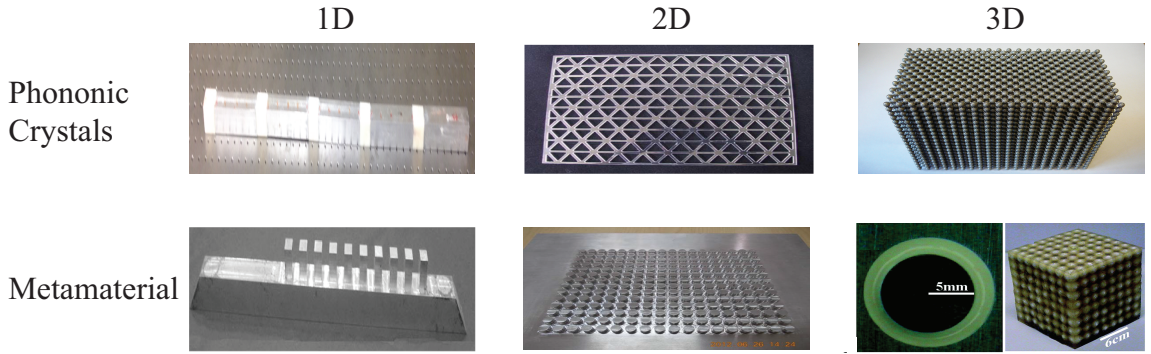
Figure 1.1: Realization of PnCs and AMs in one, two and three dimensions

Phononic materials can be modeled, analyzed and realized in different dimensions see Fig. 1.1. Apart from dimensionality, phononic materials are modeled in either continuum form (e.g., rod, beam, plate, shell or bulk material) or discrete form (e.g., lumped mass system); however, to demonstrate most of its important dynamical characteristics, a simple one-dimensional (1D) spring-mass model is sufficient. A 1D model of a PnC is represented by two masses m_1 and m_2 connected in series by springs k_1 and k_2 (Fig. 1.2.a). The equations of motion for the system are presented in eqs. 1.1 and 1.2 for m_1 and m_2, respectively,

$$m_1 \ddot{u}_1^j + k_1(u_1^j - u_2^{j-1}) + k_2(u_1^j - u_2^j) = 0 \tag{1.1}$$

$$m_2 \ddot{u}_2^j + k_1(u_2^j - u_1^{j+1}) + k_2(u_2^j - u_1^j) = 0 \tag{1.2}$$

where u is the displacement, j is the unit cell index and $(\ddot{\cdot})$ is the second derivative of $(.)$ with

---

[1] If the material admits elastic waves, a more accurate term is "elastic metamaterial".
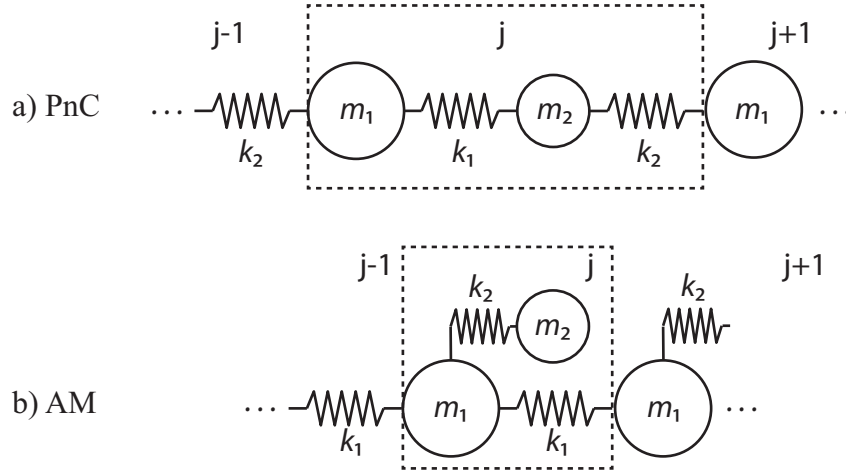
Figure 1.2: Schematic models for PnCs and AMs

respect to time.

For the AM, the same number of masses and springs are used, albeit connected differently (Fig. 1.2.b). The equations of motion for the system are presented in eqs. 1.3 and 1.4 for m_1 and m_2, respectively.

$$m_1 \ddot{u}_1^j + k_1(2u_1^j - u_1^{j-1} - u_1^{j+1}) + k_2(u_1^j - u_2^j) = 0 \tag{1.3}$$

$$m_2 \ddot{u}_2^j + k_2(u_2^j - u_1^j) = 0 \tag{1.4}$$

Assuming a generalized Bloch solution of the form $\mathbf{u}^{j+n} = U e^{i(\omega t + n\kappa a)}$, where ω is the frequency, κ is the wavenumber and a is the unit cell size (i.e., lattice spacing) and collecting together the equations of motion for both systems yields a complex generalized eigenvalue problem in the form:

$$(\omega^2 \mathbf{M} + \mathbf{K}(\kappa))\mathbf{u} = \mathbf{0} \tag{1.5}$$

where mass and stiffness of each system matrices are written as:

$$\mathbf{M}_{PnC} = \begin{bmatrix} m_1 & 0 \\ 0 & m_2 \end{bmatrix}, \mathbf{K}_{PnC}(\kappa) = \begin{bmatrix} k_1 + k_2 & -(k_1 e^{-i\kappa a} + k_2) \\ -(k_1 e^{i\kappa a} + k_2) & k_1 + k_2 \end{bmatrix} \tag{1.6}$$

$$\mathbf{M}_{AM} = \begin{bmatrix} m_1 & 0 \\ 0 & m_2 \end{bmatrix}, \mathbf{K}_{AM}(\kappa) = \begin{bmatrix} 2k_1(1 - \cos(\kappa a)) & -k_2 \\ -k_2 & k_2 \end{bmatrix} \tag{1.7}$$

In order to obtain statically equivalent models for the PnC and AM, the spring stiffness should be adjusted such that the speed of sound c of each model matches in the long-wavelength limit [3]:

$$c = \lim_{\kappa \to 0} \frac{\omega}{\kappa} \tag{1.8}$$

By using the values in table 1.1 for both systems we solve the eigenvalue problem in Eq. 1.5, and obtain the dispersion curves of the two material systems that correlate frequency to wavenumber (Fig. 1.3).

Table 1.1: Summary of parameters for PnCs and AMs unit cells

Cell	$m_1[kg]$	$m_2[kg]$	$k_1[N/m]$	$k_2[N/m]$	$c(\kappa \to 0)[m/s]$
AM	1	2	10,000	10,000	57.73
PnC	1	2	20,000	20,000	57.73
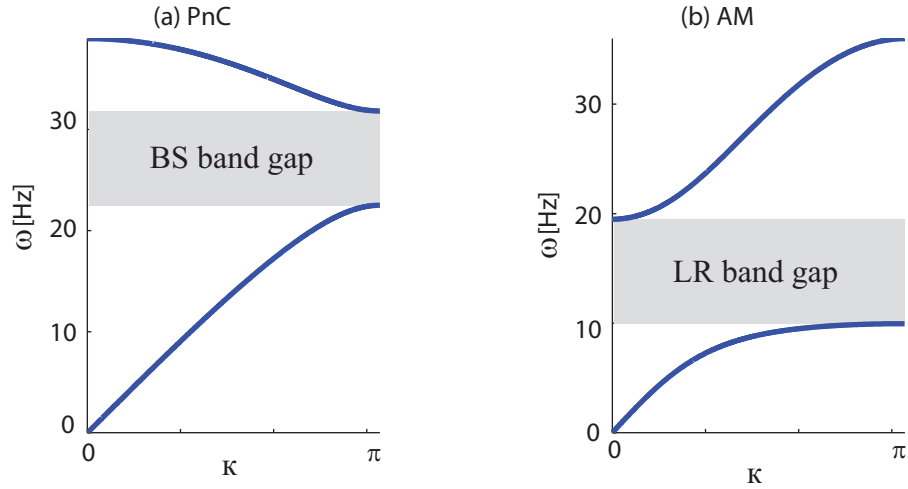
Figure 1.3: Dispersion curves for PnC and AM systems

The two dispersion curves have the same slope (i.e., group velocity) in the first branch for small κ values (i.e., the long wavelength limit). However, the group velocity decays quicker in the AM as κ increases, due to a hybridization between the first branch (a.k.a., the acoustic branch) and the local resonance mode. The band gaps are highlighted in gray. The PnC band gap ranges

from 22-31 Hz, while for a statically equivalent AM system the band gap exists at a lower frequency range, 10-20 Hz.

PnC and AM cells can also be analyzed as a finite structure, with the number of cells in the material system denoted by N_{cell}. In this setting, one can formulate the problem in two different ways; vibration analysis and wave propagation. In the first model, steady-state and harmonic excitation are assumed to obtain a frequency response function (FRF).
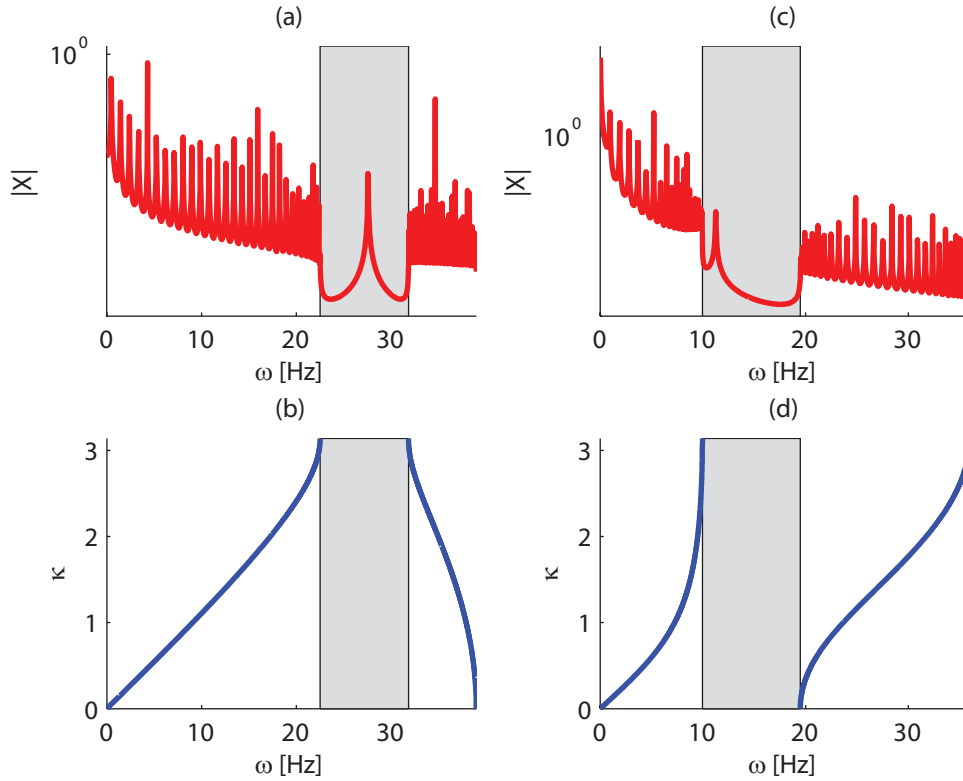
Figure 1.4: Dispersion and FRF for (a-b) Phononic Crystal and (c-d) Acoustic Metamaterial; gray shaded area represents a band gap

The FRF and dispersion curves for both cells are presented in Fig. 1.4. It is worth noting that in the FRF for both systems, there appears to be an anomaly within the band gap, which can be attributed to breaking the symmetry of the system due to finite size truncation. Apart from this anomaly, the FRF follows the dispersion in that when the frequency of excitation occurs in a band gap, the response exhibits a minimum for both the PnC and AM cells. The FRF provides a verification to the unit cell dispersion analysis.

The study of wave propagation in phononic materials can be done integrating the equations of motion based on the same $\mathbf{M}$ and $\mathbf{K}$ matrices for this finite structure using the Newmark method given by Eqs. 1.9- 1.11.

$$\mathbf{D_{i+1}} = \mathbf{D_i} + \mathbf{\Delta t V_i} + (\mathbf{\Delta t})^2 \left[\left(\frac{1}{2} - \beta \right) \mathbf{A_i} + \beta \mathbf{A_{i+1}} \right], \tag{1.9}$$

$$\mathbf{V_{i+1}} = \mathbf{V_i} + \mathbf{\Delta t} \left[(1 - \gamma) \mathbf{A_i} + \mathbf{A_{i+1}} \right], \tag{1.10}$$

$$\mathbf{M A_{i+1}} + \mathbf{K D_{i+1}} = \mathbf{F_{i+1}}, \tag{1.11}$$

where $\mathbf{D_i}$, $\mathbf{V_i}$, and $\mathbf{A_i}$ represent the displacement, velocity, and acceleration vectors at the ith time-step. The value of Δt is chosen such that the simulation is both accurate and stable for a given forcing frequency ω. By selecting $\gamma = 1/2$ and $\beta = 0$, the Newmark method becomes a fully explicit scheme with accuracy on the order of $O(\Delta t^2)$. The solution method is as follows. First, the new displacement is obtained through Eq. 1.9. After which, Eq. 1.11 is inverted for the unknown acceleration $\mathbf{A_{i+1}}$. Finally, Eq. 1.10 is used to obtain the updated velocity, after which the simulation is marched forward in time and the process repeated for a specified amount of time.

The response of the system considered earlier is obtained by integrating the equations of motion using the Newmark method applying fixed-free boundary conditions with $N_{cell} = 60$. A case of prescribing a displacement on m_1 of the first unit cell is considered

$$D(1)_{m_1} = A \sin (2\pi\omega t), \tag{1.12}$$

where $D(1)_{m_1}$ represents the displacement of the first mass m_1 of the first unit cell. The forcing frequency ω is in units of [Hz], $A = 1 \ [m]$ is the amplitude of displacement, and t represents time. The total time of integration $t_f = 1.42 \ [s]$ is selected for both the AM and PC systems such that reflections from the fixed boundary condition of $D(N_{cell})_{m_1}$ do not pollute the response.
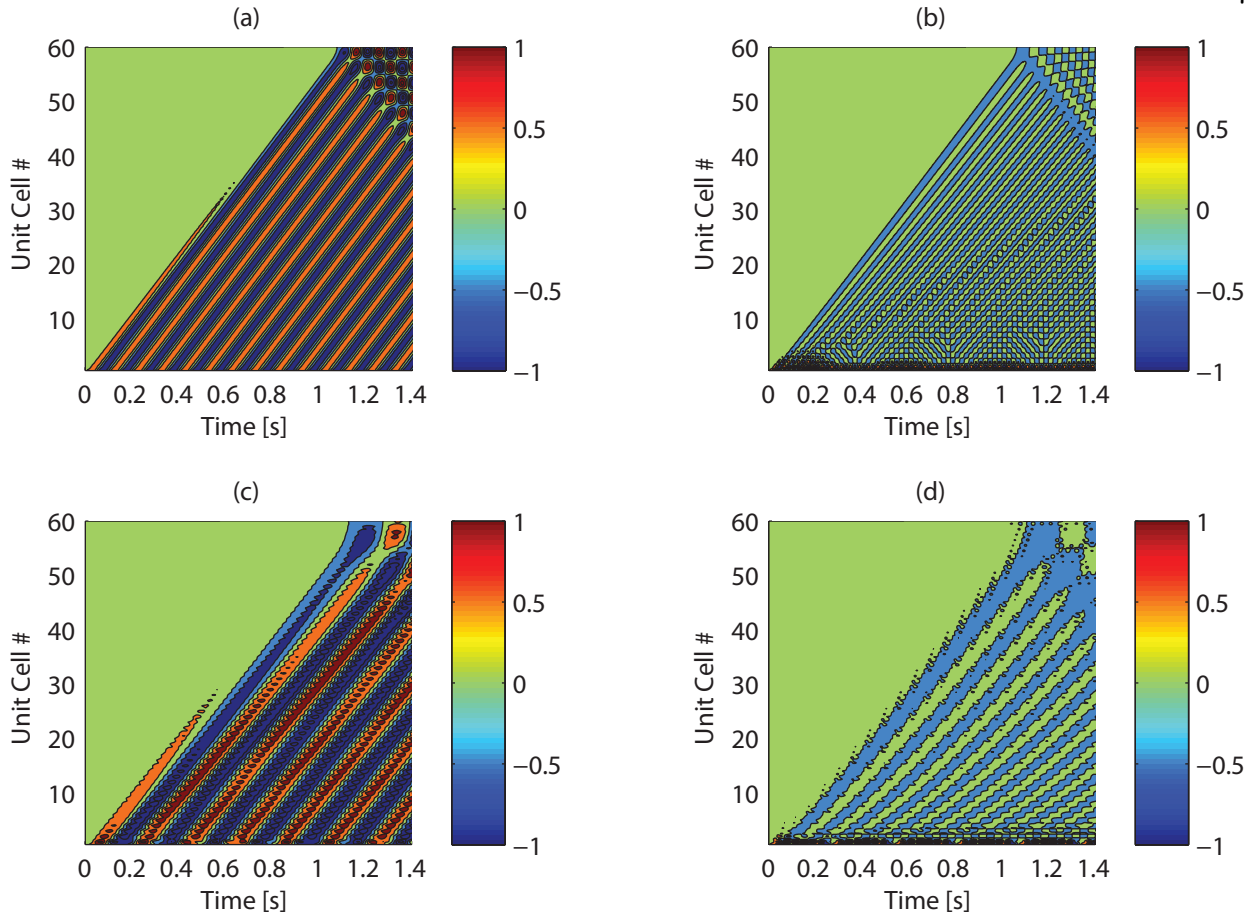
Figure 1.5: Space-time contours of (a) PnC excited at $\omega = 10$ [Hz] (pass band); (b) PnC excited at $\omega = 25$ [Hz] (stop band) (c) AM excited at $\omega = 5$ [Hz] (pass band); (d) AM excited at $\omega = 15$ [Hz] (stop band)

Spatial-temporal contours of displacement are presented in Fig. 1.5 for both the PnC and AM cases, with prescribed displacements occurring at frequencies in both a pass band and a stop band to observe the global response of the system. It is evident that the response throughout the system is high when excited in a pass band and relatively low when excited in a stop band for both systems. In addition, these contours provide a visualization of wave reflections on the fixed boundary, and is clearly shown in the PnC system at approximately $t = 1.1$ [s] in Fig. 1.5(a).

Observing the displacements of mass 1 and mass 2 in the 30th unit cell in Fig. 1.6, we see that in a pass band the displacements are rather large, and even exceed the amplitude of the prescribed displacement which indicates a large transmission of energy through the structure. In a stop band,

however, the displacements are drastically reduced. It is interesting to note that for both the PnC and AM cases, mass 1 and mass 2 appear to be in-phase with one another. In addition, when the AM system is excited in a pass band, the resonating mass m_2 has higher amplitude than the "outside" mass m_1.
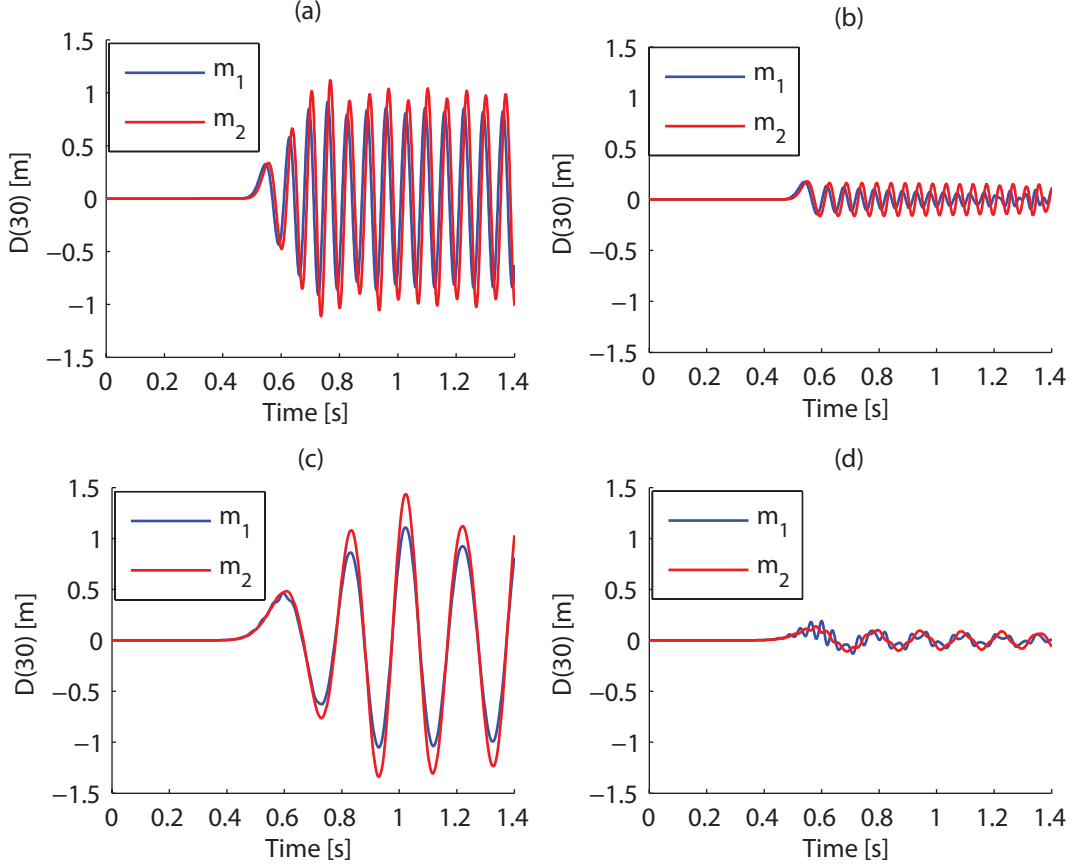
Figure 1.6: Displacement of the 30th unit cell (a) PnC excited at $\omega = 10Hz$ (pass band); (b) PnC excited at $\omega = 25Hz$ (stop band) (c) AM excited at $\omega = 5Hz$ (pass band); (d) AM excited at $\omega = 15Hz$ (stop band)

As stated earlier, one-dimensional models of PnC and AM are sufficient to explain most of the basic concepts. In 1D, the range of wavenumbers defining the fundamental period of the dispersion relation encompassing half of the unit-cell due to the symmetry of the dispersion relation is called the irreducible Brillouin zone (IBZ). However, when dealing with higher dimensional models, lattice symmetry plays a more subtle role in defining the boundaries of IBZ. Figure 1.7 shows the IBZ for square and hexagonal lattices with C_{4v} symmetry [4] imposed at the unit-cell level. Subsequently,

design representation is needed in only a portion of the unit cell and the band-structure calculation is limited to the corresponding IBZ (Fig. 1.8).
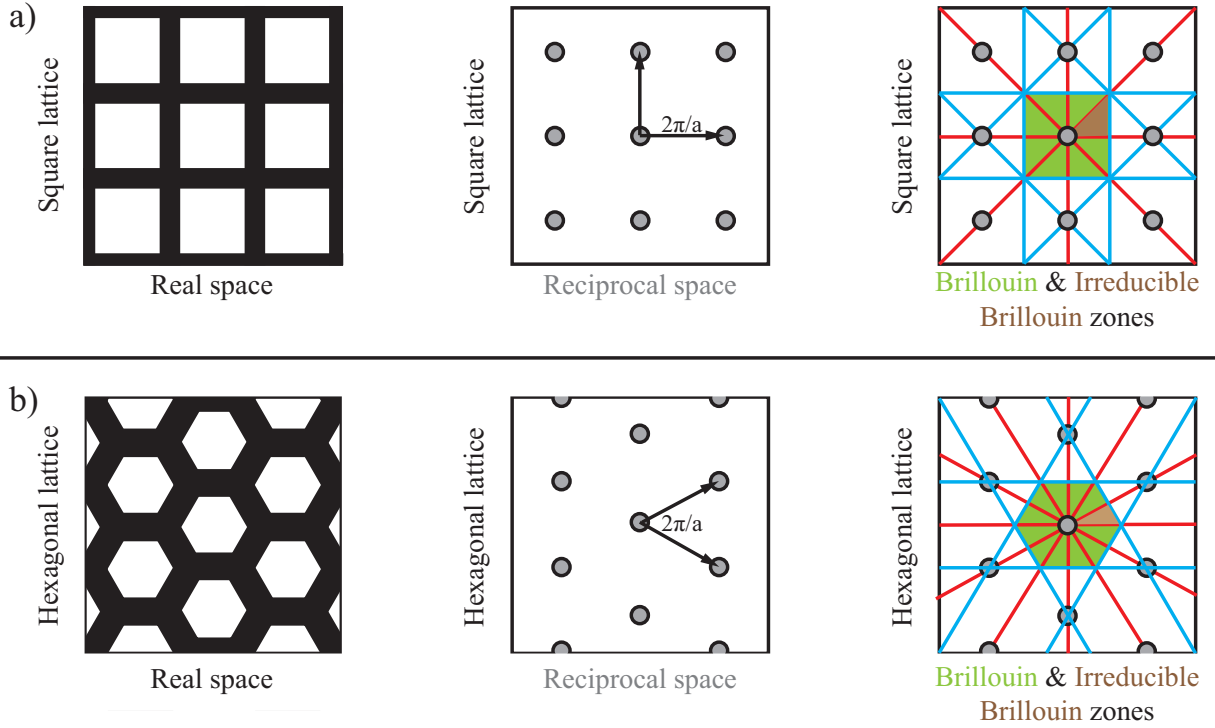
Figure 1.7: The irreducible Brillouin zones for (a) square (b) hexagonal unit cell in real and reciprocal space

1.2 Motivation

Applications of phononic materials include elastic or acoustic waveguiding and focusing, vibration minimization, sound collimation, frequency sensing, acoustic cloaking, acoustic rectification, opto-mechanical waves coupling in photonic devices, thermal conductivity reduction in semiconductors, among others [1]. These applications require well defined characteristics of phononic materials, hence unit cell design and optimization can lead to the discovery of better performing phononic materials/devices. Since many of these applications are based on band gap utilization, an important design objective is to widen the band gap. Designing the phononic material on the unit cell level is advantageous in many aspects. It is computationally less expensive than designing an entire

a) Two-dimentional Square lattice
(Real Space)

b) Irreducible Brillouin Zone
(Reciprocal Space)

c) Dispersion Curves
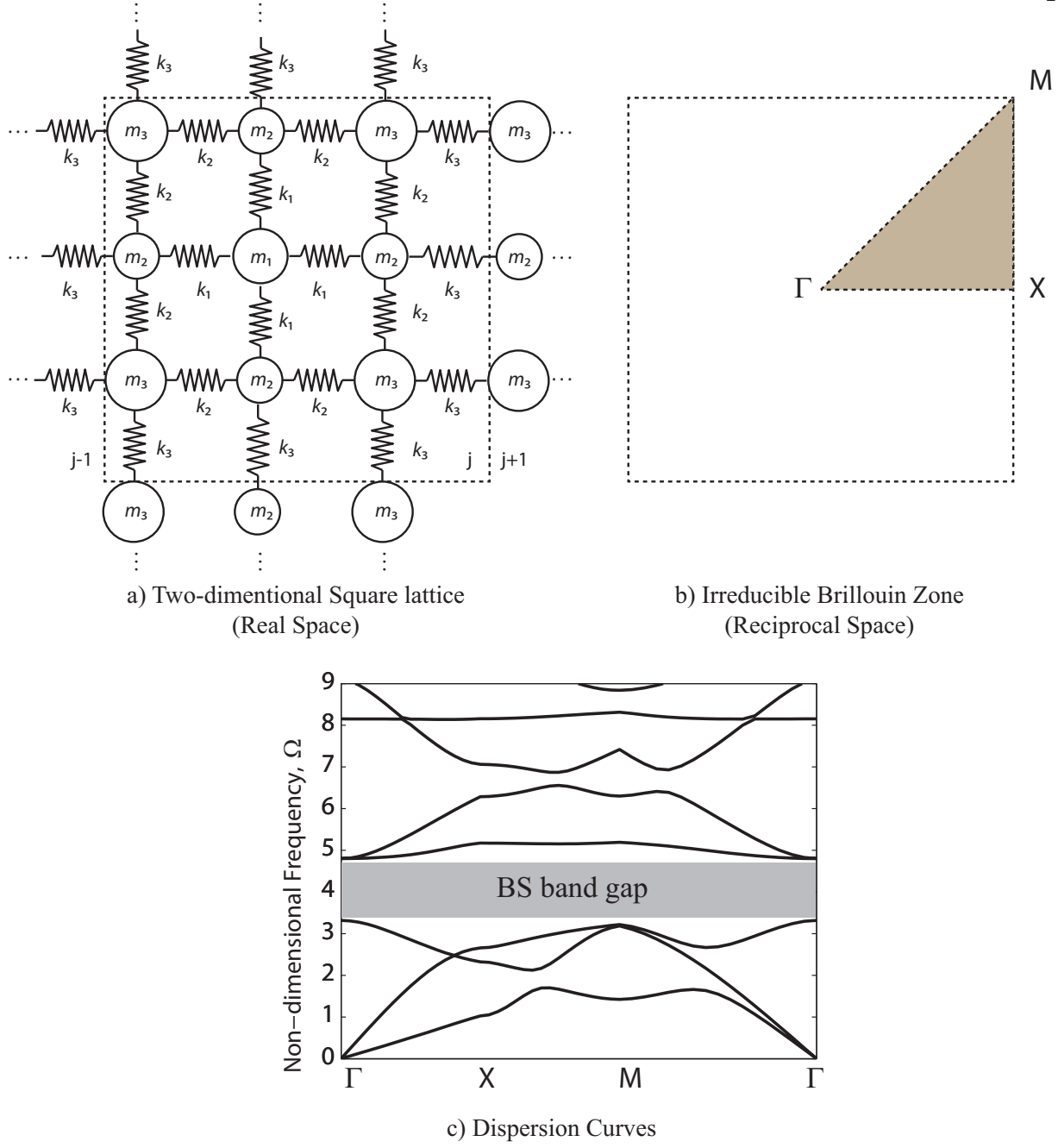
Figure 1.8: Two-dimensional phononic crystals arranged in a square lattice and its corresponding irreducible Brillouin zone

structure. It is also scale independent (i.e., you can use an optimized unit cell to attenuate waves of a few Hz or GHz with proper scaling). This is why keeping the band gap central frequency as low as possible reduces the total material/device size.

Unit-cell design optimization for a desired objective can be carried out using three approaches as presented in Fig. 1.9. One approach is parametric sweeping, that is, given a particular unit cell shape and geometry, the unit cell attributes/parameters are varied systematically while preserving its shape. Another approach is to start with a certain topology (i.e., fixed number of holes), and vary their shape to improve the design without changing its topology. The third approach is to have no assumptions about the unit cell topology a *priori*, leaving the job of defining the topology to the optimization algorithm. The latter is the most general of the three and the approach considered in chapters 2 and 3. Since both shape and topology approaches involve varying design parameters throughout the optimization process, modern classifications consider parametric sweeping a subclass of either one.
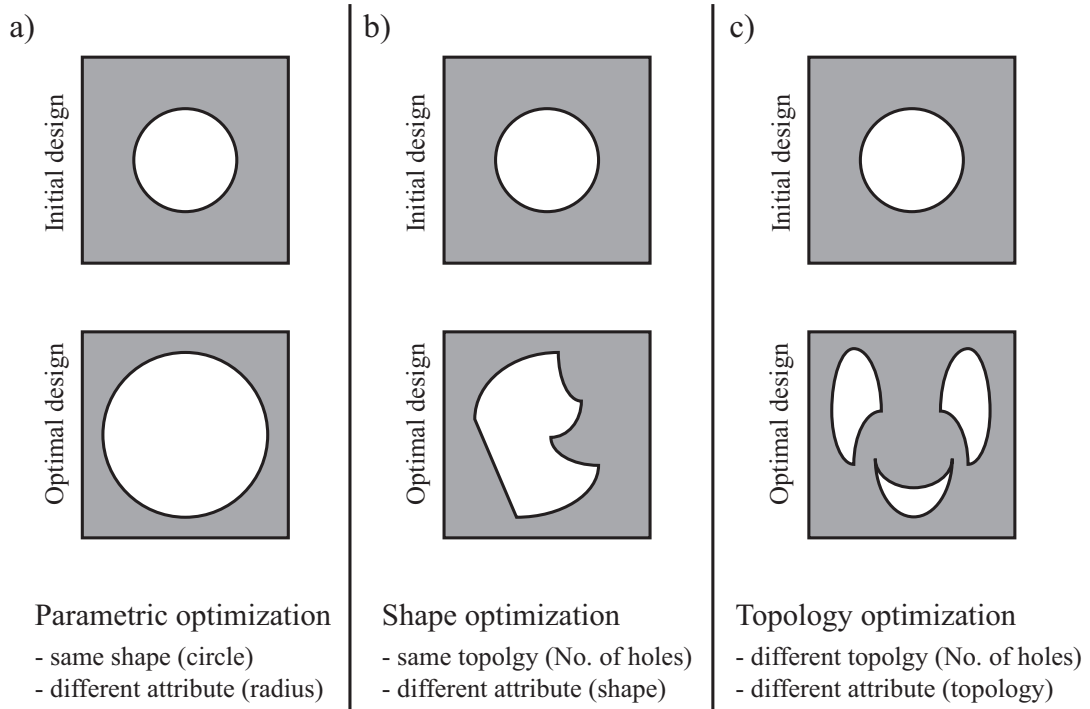
Figure 1.9: Unit cell optimization approaches

This thesis covers the unit cell design and optimization problem in one, two and three-dimensions. Aside from the optimization technique, the design domain for two or three-dimensional crystals is typically divided into uniformly sized pixels allowing a material phase to be allocated to

each pixel. Regarding the one-dimensional case, the representation of the material topology within a layered unit cell needs to incorporate the number of material phases, the number of layers, and the thickness of each of the layers.

The design space for the problems at hand is intractable, thus considering all the alternatives is unfeasible. Considering a simple 2D unit cell with 32×32 pixels, the number of possible designs exceeds 10^{40} as shown in Fig 1.10. A computer that could test a single design per second and commencing its calculations at the beginning of time, approximately, 14 billion years ago at the onset of the Big Bang, would have examined fewer than 1% of all the possibilities by the present time! Due to the presence of eigenvalue multiplicities and the non-convexity nature of the objective functions considered, gradient-based methods suffer from low regularity and non-differentiability. This suggests that the problem of band gap optimization is multi-modal in nature and manifests a complex design landscape. Evolutionary algorithms are therefore a natural choice for this problem.
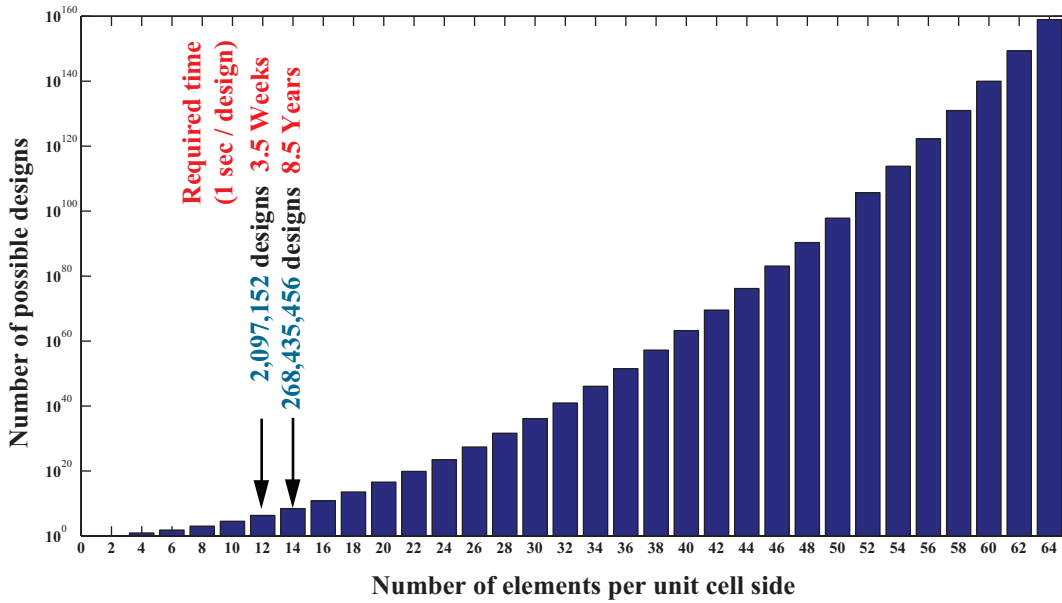
Figure 1.10: Search space size for a simple n×n two-dimensional unit cell

1.3   Literature search

The following section includes a general outline of the field and its application. A more focused literature search is provided in chapters 2-5 for the specific problems studied.

1.3.1   Phononic materials

The study of wave propagation in periodic media was first formulated by Floquet [5] in one-dimension. Bloch generalized the work of Floquet to three dimensions in what is now known as Floquet-Bloch theory, or Bloch's theorem for short. However the systematic study of phononic crystals started with the work of Sigalas and Economou in [6] and Kushwaha *et. al.* [7]. The introduction of acoustic metamaterials by Liu *et. al.* occurred almost a decade later [8].

In a phononic crystal, band gaps are generated by Bragg scattering for which an underlying constraint is that the wavelength has to be on the order of the lattice spacing [7, 9]. In a locally resonant acoustic/elastic metamaterial, on the other hand, band gaps may be generated by the mechanism of hybridization between local resonances and the dispersion properties of the underlying medium, and this in turn may take place at the subwavelength regime [8]. These unique dispersion properties may sufficiently be utilized in numerous applications involving wave filtering, [10, 11, 12] localization, [13, 14] guiding, [14, 15] focusing, [16, 17, 18] collimation, [19, 20] among others. The applications of locally resonant acoustic/elastic meteamterials are, in turn, far from conventional, e.g., subfrequency wave isolation, [21] subwavelength focusing and imaging, [22, 23] and cloaking, [24, 25] to name a few.

Unit cell optimization has been considered in the literature in one dimension [26, 12] as well as two dimensions [27, 28, 29, 30, 31, 32] by using gradient-based [27, 28, 29, 30] as well as non-gradient-based [12, 31, 32] techniques. While there are numerous studies on band-gap maximization for phononic crystals, less work has been done for locally resonant acoustic/elastic metamaterials. However, previous studies [12, 33, 34] and preliminary investigations [35, 36] have suggested that the general problem of band gap optimization is multi-modal in nature and manifests a complex

design landscape.

1.3.2   Flow control

Flow control, not to be confused with flow-rate control in valves, is the ability to manipulate/alter a flow field in desired way. This manipulation can be divided into three main classes. The control of: (1) transition, delaying or advancing laminar flow transition to turbulence; (2) separation, preventing or provoking flows to separate from bodies in relative motion with the flow; (3) turbulence, suppression or enhancement of a turbulent flow. By achieving one or more of these three objectives, many applications can be improved. In particular, certain engineering challenges can be met (e.g., drag reduction, lift enhancement, mixing augmentation and noise suppression).

Different classification criterion exist for flow-control methods. One criteria is to consider whether the technique is applied at the wall or away from it. Wall surface parameters can influence the flow due to roughness, shape, curvature, rigid-wall motion, compliance, temperature, and porosity [37]. Flow control strategies can also be divided in two categories based on energy expenditure (1) active flow control [38] (2) passive flow control [39].

Inspired by the exceptional swimming efficiency of dolphins, Kramer proposed using a compliant coating layer covering the body of moving objects to reduce drag, speculating that a dolphin's body may have a very low drag coefficient [40]. His experiments showed a substantial reduction in drag of up to 50% using a compliant coating modeled from dolphin's skin. Benjamin did theoretical analysis on the effectiveness of compliant coatings for drag reduction in the turbulent boundary layer instead of using them in the laminar boundary layer, where the dolphin is believed to be able to reduce the skin-friction drag by delaying transition to turbulence [41]. Attempts to replicate Kramer's original experiment and achieve similar drag reduction percentages were pursued with no success [42]. Carpenter verified Kramer hypothesis for both Tollmien-Schlichting (TS) type instabilities [43] and flow-induced surface instabilities [44]. Multi-layer compliant walls were first introduced in Refs. [45] and [46]. Semenove [47] formulated two necessary conditions of modeling and the choice of viscoelastic coatings for drag reduction. Carpenter studied optimizing compliant

coatings using different panels [48], but it was not until 1997 when Choi *et. al.*[49] experimentally demonstrated the ability, in principle, of compliant surfaces to reduce the skin-friction drag and surface-flow noise in a turbulent boundary layer. Carpenter used a short compliant panel to suppress two-dimensional TS waves propagating along a wall shear layer using direct numerical simulation (DNS) [50].

Other passive flow control methods can be found in the literature [51, 52]. A well-known approach is the use of riblets [53], that is, small surface protrusions aligned with the direction of the fluid mean flow. Chu *et. al.* [54] and Goldstein [55] carried out a direct numerical simulation of laminar and turbulent flow over riblet-mounted surfaces. A review by Dean *et. al.* [56] summerizes the recent work done on riblets.

All of the previously mentioned methods have been extensively studied computationally and experimentally as a potential means for flow control, particularly drag reduction; but have not conclusively proven to be useful in applications, particularly in the aerospace industry [57]. Xu *et. al.* [58] showed that, for compliant surfaces, the benefits gained are very small and there is little change in the very long-time behavior of the turbulent skin friction drag and little modification to the near-wall turbulent coherent structures. In addition, from a practical point of view, compliant coatings do not offer the load bearing capacity needed. Moreover compliant surfaces performance in drag reduction generally deteriorates with the age of the coatings [59, 60]. For riblets, durability tests in airline service showed major complications [57].

1.4   Thesis objectives

The thesis explores the fertile ground of phononic materials through design and optimization and investigates its applicability to control a flow field. This exploration can be outlined as follows:

- Develop an optimization framework that has the capacity to produce unit cell designs/topologies with particular dispersion characteristics of interest.

- Utilize this optimization framework for different design studies in one, two and three-

dimensions and analyze the results to gain a deeper understanding of the problem physics.

- Explore different practical design mechanisms for enlarging super/subwavelength band gaps for phononic materials.

- Investigate the ability of phononic materials, in general, to manipulate a flow field in a favorable manner.

1.5 Thesis organization

The thesis is organized as follows: chapters 2-4 are reprints of completed/published work. Chapter 2 covers an optimization study for a one-dimensional phononic crystal modeled as a rod for different objective functions [61]. In chapter 3, the optimization study of a two-dimensional unit cell for different wave polarizations is included [62, 36]. A novel design concept for enlarging a subwavelength band gap for a metamaterial [63] based on reducing the base compliance is presented in chapter 4. Chapter 5 presents the investigation of using phononic crystals for flow control. The last chapter draws conclusions on the work and outlines possible future directions.

Chapter 2

On the properties of optimized layered phononic crystals[1]

2.1   Abstract

A periodic material is composed of two or more different elastic materials laid out in space in a repeated fashion. The properties of a periodic material depend on the arrangement of materials within its basic building block (i.e., unit cell). Periodic materials are commonly characterized by their dispersive frequency spectrum. With appropriate spatial distribution of the constituent material phases, spectral stop bands can be generated. Moreover, it is possible to control the number, the width, and the location of these bands within a frequency range of interest. This study aims at exploring the relationship between the unit cell configuration and its frequency spectrum characteristics. A subcategory of periodic systems that affects mechanical waves, *phononic materials*, is considered. Focusing on a layered configuration and longitudinal wave propagation in a direction normal to the layering. the unit cell features of interest are the number of layers, material phase and relative thickness of each layer. An evolutionary search for multi-phase cell designs exhibiting a wide stop band, or a series of wide stop bands, is conducted using a specially formulated representation and a set of operators that break the symmetries in the problem. The designed phononic materials are excellent candidates for use in a wide range of applications including the development of vibration and shock isolation structures, sound isolation pads/partitions, multiple band frequency filters, among many other applications.

---

[1] This chapter is drawn from Ref. [61] and has been adapted to suit the style and the notation of the dissertation.

2.2   Introduction

Phononic crystals are composite materials consisting of a periodic spatial distribution of constituent material phases, usually a stiff, high density phase and a compliant, low density phase. The characteristics of elastic wave propagation through these crystals is frequency-dependent. Within stop bands (also referred to as band gaps), a medium effectively prohibits elastic wave propagation, and the converse takes place at pass band frequencies. These bands are commonly identified through a frequency spectrum diagram relating frequency to wavenumber. The topological distribution of constituent material phases within a unit cell (the smallest repeatable spatial unit) directly affects the location and width of stop bands and pass bands in the frequency domain. This provides an opportunity for designing composite materials with specific dynamical characteristics that can be utilized for a wide range of traditional applications including sound and vibration filtering [64]. This concept can also be extended to nanoscale crystalline composite materials such as thermoelectric super-lattices which enable solid state energy conversion. In these materials, which usually exhibit layered topologies, engineering of the frequency band structure is an avenue for reducing the thermal conductivity and increasing the energy conversion figure-of-merit [65, 66].

Tailoring a unit cell for a desired band structure can be realized for different types of objective functions depending on the application. Commonly, it is desired to optimize for a band gap with maximum width centered at a given frequency or maximum width centered at a minimum frequency [67]. Optimizing for maximum attenuation at a band-gap frequency or for maximum size of multiple band gaps over a large frequency range has also been considered [12, 64]. Previous studies [33, 34, 12] and a preliminary investigation [35] have suggested that the general problem of band gap optimization (in phononics or photonics) is multi-modal in nature and manifests a complex non-convex design landscape. Evolutionary algorithms are therefore a natural choice for this problem. The challenge is to find *(i) an efficient representation that eliminates degeneracies (ii) effective evolutionary operators.*

Utilization of stop-bands and pass-bands characteristics for materials design has been con-

sidered before by this group [64, 68, 35, 12, 32]. Hussein et al. [12] used a multi-objective Genetic Algorithm (GA) with two alternative formulations, binary and mixed. They considered three separate objectives, in addition to minimizing the number of layers, the first was to maximize wave attenuation, the second was to minimize the transmissibility (i.e., maximizing the number of stop band gaps) and the third was to create band gaps at specified frequency ranges. Although the inherent symmetry in the unit cell design problem was addressed, it was not fully capitalized on. The study of El-Beltagy and Hussein [68] considered the first two objectives in [12] with a single objective problem formulation and the introduction of a new scale-preserving and repair free representation that fully utilize the symmetry of the periodic layered unit cell. The same framework was used in [35] to address the effect of different material properties on the objective functions considered. In the present work an investigation of the same problem with the introduction of new repair-free localized genetic operators that fully utilize the symmetry with capturing the salient features of the problem is carried out. Furthermore, analysis of the properties of the evolved designs and their corresponding objective functions is presented.

In the next section, the mathematical background for wave propagation analysis is briefly described. This is followed by sections on the description of the various objective functions considered, the unit cell chromosome representation, and the developed evolutionary operators. The results are then presented in a separate section, followed by a discussion and a conclusion.

2.3   Frequency spectra computation

The governing equation of motion for longitudinal wave propagation in a 1D heterogeneous solid is

$$\rho \ddot{u} = \sigma + f, \tag{2.1}$$

where $\rho = \rho(x)$, $\sigma = \sigma(x)$, $u = u(x,t)$ and $f = f(x,t)$ denote density, stress, displacement and external force, respectively. The position coordinate and time are respectively denoted by x and t.

Assuming a linear elastic material,

$$\sigma = Eu \tag{2.2}$$

where $E = E(x)$ is the elastic modulus. To model a phononic crystal, we consider an infinite general multilayered medium where an arbitrary layer j is positioned between an adjacent layer $j-1$ at its left and an adjacent layer $j+1$ at its right. The interface between the layers is assumed to be ideal. The jth layer has thickness $d^{(j)}$, density $\rho^{(j)}$, elastic modulus $E^{(j)}$, and longitudinal velocity

$$c_p^{(j)} = \sqrt{E^{(j)}/p^{(j)}}, \tag{2.3}$$

respectively. The boundary conditions that must be satisfied at the layer interfaces are (i) continuity of the displacement u and (ii) continuity of the stress σ. Furthermore, no external forces are permitted, i.e., $f = 0$, in 2.1.

The solution of 2.1 in the jth layer can be written as a superposition of forward and backward traveling waves with harmonic time dependence:

$$u(x,t) = \left[A_+^{(j)} e^{ik_p^{(j)}} + A_-^{(j)} e^{-ik_p^{(j)}} \right] e^{-i\omega t} \tag{2.4}$$

where $i = \sqrt{-1}$, $k_p^{(j)} = \omega/c_p^{(j)}$, ω is the temporal frequency, and $A_\pm^{(j)}$ are complex coefficients. The stress component is given by

$$\sigma(x,t) = E^{(j)}(x) = \frac{\partial u(x,t)}{\partial x} \tag{2.5}$$

Let x^{jL} and x^{jR} denote the position of the left and right boundaries of layer j, respectively. From 2.4 and 2.5, and using the relation

$$x^{jR} = x^{jL} + d^{(j)}, \tag{2.6}$$

the values of the displacement u and stress σ at x^{jL} are related to those at x^{jR}. Through a *transfer matrix* $\mathbf{T}_j$, where

$$\mathbf{T}_j = \begin{bmatrix} \cos\left(k^{(j)}d^{(j)}\right) & \left(1/Z^{(j)}\right)\sin\left(k^{(j)}d^{(j)}\right) \\ -Z^{(j)}\sin\left(k^{(j)}d^{(j)}\right) & \cos\left(k^{(j)}d^{(j)}\right) \end{bmatrix}, \tag{2.7}$$

and $Z^{(j)} = \rho^{(j)} c^{(j)^2} k^{(j)}$, this mapping can be repeated recursively to relate the displacements and the stresses across several layers. For a periodic medium with n layers in the unit cell, a cumulative transfer matrix across a cell $\mathbf{T} = \mathbf{T}_n \mathbf{T}_{n-1} \cdots \mathbf{T}_1$ is constructed:

$$\begin{bmatrix} u_1 \\ \sigma \end{bmatrix}_{x^{nR}} = \mathbf{T} \begin{bmatrix} u \\ \sigma \end{bmatrix}_{x^{1L}}. \tag{2.8}$$

The periodicity also allows the application of Floquet-Bloch theory. Denoting the cell length as d, that is $d = d^{(1)} + d^{(2)} + \ldots + d^{(n)}$, the time harmonic response in two adjacent cells are related by

$$\begin{bmatrix} u \\ \sigma \end{bmatrix}_{x+d} = e^{ikd} \begin{bmatrix} u \\ \sigma \end{bmatrix}_{x}, \tag{2.9}$$

where k is a complex wavenumber. Applying 2.9 at $x = x^{1L}$ and coupling it with (2.8) results in the eigenvalue problem

$$\left[\mathbf{T} - \mathbf{I} e^{ikd} \right] \begin{bmatrix} u \\ \sigma \end{bmatrix}_{x^{1L}} = 0, \tag{2.10}$$

which is solved for the dispersion curves (ω versus k). It is advantageous for these curves to be represented in a non-dimensional form, that is,

$$\Omega = \omega d / \sqrt{E_1/p_1} \tag{2.11}$$

for the dimensionless frequency (subscript "1" denotes lowest elasticity modulus and density phase), and

$$\xi = \xi_{\text{real}} + i\xi_{\text{imag}} = kd. \tag{2.12}$$

or the dimensionless wavenumber.

2.4 Unit cell analysis

Since the problem in hand is periodic, the rod is treated as an infinite number of repeated unit cells. Each unit cell is composed of n layers. The layers could be a low stiffness material (matrix) or a high stiffness one (fiber). Fig. 2.1 shows only one unit cell of width d with n layers.
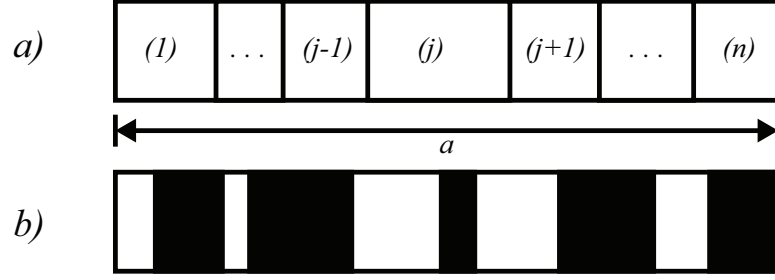
Figure 2.1: (a) A general one-dimensional unit cell consisting of n layers (layer number indicated in parenthesis) (b) Example of one-dimensional unit cell consisting of 10 layers.

For our problem formulation, without any loss of generality, the first unit cell is the widest fiber layer in the composite. Unit cells with different numbers of layers have been considered in separate optimization runs, in order to understand the effect of the number of layers on the maximum band gap value.

For the simplicity of argument, we consider here the fundamental case that involves the design of a two-phase phononic material. The unit cell can be represented either by (a) having a chromosome of zeros and ones representing the different material types for a given number of 0/1 slots (binary approach), or (b) specifying the number of layers and the phase and width of each layer (mixed approach) [12]. Both of these approaches underutilize the fact that we are dealing with a periodic material and hence a large number of apparent cell designs are equivalent. This is clearly demonstrated in the example given in Fig. 2.2.

2.5   Problem formulation

The problem of designing a one-dimensional phononic structure can be represented mathematically as follows:

Decision Variables:

d_j: The width of layer j in the design $\overline{d}$.
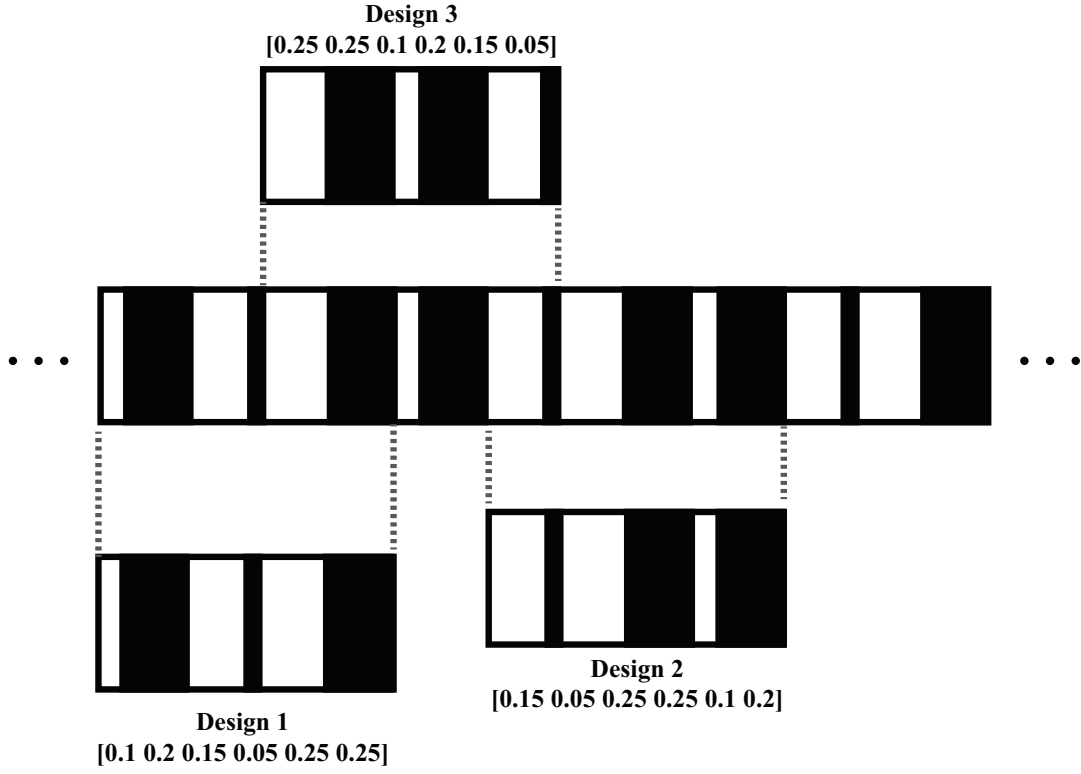
Figure 2.2: Due to the symmetry of the problem, many different unit cell representations can produce the same layered material. The three identified designs have unique layer width, yet they represent the same composite material.

1st Objective Function:

$$Minimize \ \ f(\overline{d}) \tag{2.13}$$

Subject to:

$$\sum_{j=1}^{n} d_j = 1, \tag{2.14}$$

$$d_1 > d_j, \ \ j = 3, 5, ..., n-1, \tag{2.15}$$

$$mod(n, 2) = 0, \ \ n \ is \ an \ even \ number, \tag{2.16}$$

$$d_j \geq w, \ \ j = 1, 2, ..., n, \ \ w = minimum \ width \ allowed, \tag{2.17}$$

$$d_j \in R_n, \tag{2.18}$$

where $f(\overline{d})$ represents any of the four objective functions considered. The objectives involve maximizing the attenuation at a given frequency, and maximizing the percentage of stop bands within a specified large frequency range for minimum transmissibility. Some of these objectives were explored in previous work [12]. In this work, we report better performing designs and draw some conclusions regarding the search space of the problem and the properties of the emerging designs.

Maximizing the attenuation at a given non-dimensional frequency Ω^* makes use of the fact that the strength of spatial attenuation of an incident wave at a stop band frequency is exponentially related to the value of the corresponding imaginary wavenumber (which is negative). Hence the first objective to be minimized is:

$$\min f_1(d) = \xi_{imag}\left(\Omega^*\right). \tag{2.19}$$

The second objective involves minimizing the transmissibility, this is defined as the percentage of the sum of frequency ranges where a pass band exists to the total frequency range $\Omega_{\min} \leq \Omega^* \leq \Omega_{\max}$ of interest. The objective is formulated as follows:

$$\min f_2(d) = 100 \times \frac{\displaystyle\int_{\Omega_{\min}}^{\Omega_{\max}} H\left(\xi_{real}(\Omega)\right) d\Omega}{\Omega_{\max} - \Omega_{\min}}, \tag{2.20}$$

where $H(\xi_{real}(\Omega))$ is hard limit function defined as

$$H(\xi_{real}(\Omega)) = \begin{cases} 1 & \text{if } \xi_{real} > 0 \ (pass\ band) \\ 0 & if\ \xi_{real} < 0 \ (stop\ band) \end{cases} \tag{2.21}$$

Maximizing the width of the first stop band relative to its central frequency (the third objective) is expressed as

$$Maximize\ f_3(d) = \frac{(\Delta\Omega)_1}{\Omega_{c1}}, \tag{2.22}$$

where $(\Delta\Omega)_1$ is the width of the first stop band and Ω_1 is its central frequency.

The fourth objective considered is maximizing the sum of the first 10 band gaps relative to their corresponding central frequency:

$$Maximize\ f_4(d) = \sum_{i=1}^{10} \frac{(\Delta\Omega)_i}{\Omega_{ci}}. \tag{2.23}$$

2.6   Genetic algorithm

The general-framework evolutionary computation offers a multitude of possibilities with regards to the ways in which a given problem is represented. Careful choice of problem representation that is based on keen insight into the nature of the design space can often improve optimization efficacy. Though the standard operators of evolutionary computation work reasonably well over a large number of problems, they can often yield poor results if the practitioner is unaware of potential complications they might introduce into the problem.

Initial Population   The standard way is choosing the layer widths for each individual (design) randomly from the allowed set of values.

Selection Operator   Tournament selection has been used here. A group of l individuals have been randomly selected. These l individuals then take part in a tournament, i.e., the individual with the best fitness is selected and the process is repeated again with other k individuals to choose the second parent.

Crossover Operator   The order and scale preserving crossover [68] has been used here as an initial step to explore the search space of such problems: The crossover operator takes two parent designs represented by d^1 and d^2 to generate a new design d' that preserves the ordering relationship. The crossover operator executes the following steps:

(1) Generate a uniformly distributed random integer j between 1 and n.

(2) Set the new layer h, $h = d_j^1 + \alpha(d_j^2 - d_j^1)$ where α is a random number between -0.25 to 1.25 (uniformly distributed).

(3) If j is odd, $j > 1$, $h > d_1^1$ and $h > 0$, go to step 1 {butting larger layer into the middle of the design which violates the assumption }.

(4) If $j = 1$, $h < d_i^1$ for any i = 2...n and $h > 0$, go to step 1.

(5) Set $d'_i = d^1_i + d^1_i * \dfrac{1 - \sum\limits_{k=1, k \neq j}^{n} d^1_k - h}{\sum\limits_{k=1, k \neq j}^{n} d^1_k}$ for $i = 1...n, i \neq j$.

(6) Set $d'_j = h$.

step 3 and 4 will ensure that the first layer is always the widest fiber layer. While step 5 and 6 will ensure that: $\sum\limits_{i=1}^{n} d_i = 1$.

A more *localized* crossover operator is implemented in this study that mimics the spirit of the scale preserving operator but in a rather confined way, i.e., to two layers only without stretching the rest of the design. This localized version is more similar to the traditional single point crossover operator in binary representation schemes.

(1) Generate a uniformly distributed random integer j between 2 and n-1.

(2) Set $d'_i = d^1_i$ for $i = 1,2, ..., j$-1.

(3) Set $d'_i = d^2_i$ for $i = j$+1, j+2, ..., n.

(4) Calculate the left width LW $= \sum\limits_{i=1}^{j-1} d^i_1$.

(5) Calculate the right width RW $= \sum\limits_{i=j+1}^{n} d^i_2$.

(6) Calculate the stretch factor $S = \dfrac{1 - LW - RW}{d^1_{j-1} + d^2_j}$.

(7) Set $d'_{j-1} = d^1_{j-1} * S$.

(8) Set $d'_j = d^2_j * S$.

Mutation Operator   The order and scale-preserving mutation [68] has been used with both types of crossover operators implemented here. The mutation operator is applied with various probabilities on a random design x in order to generate a new design d' that still preserves the order and scale. The mutation operator executes the following steps:

(1) Generate a uniformly distributed random integer j between 1 and n.

(2) Set $h = d_j + 0.2(2\alpha - 1)$ where α is a random number between 0 and 1 (uniformly distributed).

(3) If j is odd, $j > 1$, $h > d_1^1$ and $h > 0$, go to step 1 {butting larger layer into the middle of the design}.

(4) If $j = 1$, $h < d_i^1$ for any $i = 2...n$ and $h > 0$, go to step 1.

(5) Set $d_i' = d_i^1 + d_i^1 * \dfrac{1 - \sum\limits_{k=1,k\neq j}^{n} d_k^1 - h}{\sum\limits_{k=1,k\neq j}^{n} d_k^1}$ for $i = 1...n, i \neq j$.

(6) Set $d_j' = h$.

step 3 and 4 will ensure that the first layer is always the widest fiber layer. While step 5 and 6 will ensure that: $\sum\limits_{i=1}^{n} d_i = 1$

New Generation Selection After the mutation step, the fitness function of the offspring is calculated. Then a percentage of the initial population survive to the next generation while the remainder of the next population will be filled with the best offspring produced.

Termination The process terminates either at convergence or when the generation counter reaches the maximum number of generations.

2.7   Results

The process of designing a phononic crystal involves selecting different material phases. This can be a cumbersome process, due to the wide range of available options. But, since the ratio between material properties (i.e., ρ and E) dictates the performance of the designed phononic material, we investigate the effect of varying the densities and Young's moduli of material phases on the previously described objective functions. We carry out a large-scale optimization study considering all the binary combinations of ρ_{ratios} and E_{ratios} varying from 2 - 12 for (I) maximum wave-attenuation at a given frequency, (II) minimum transmissibility for a predefined frequency-range, (III) maximum relative width of the first band gap, and (IV) the sum of the former objective

over the 10 first stop bands [2.19-2.23]. We implement this methodology for layered unit cells constructed of 2 to 12 layers with a 2-layer increment (i.e., 2, 4, 6,..., 12), which reveals some counter intuitive conclusions about the objective functions considered. The results presented here are compared with those in [68, 12] using the binary and mixed-integer formulations mentioned above. In the scale-preserving and localized repair free formulation we set the population size to 120, the number of generations to 50, the crossover probability to 0.02, and the results presented are the best of 5 runs. These parameters are identical to those used in both [68, 12].

Figure 2.3(a) presents the optimal objective values for f_1, given in [Eq.2.19], as a function of the number of layers in the unit cell for a particular ratio of Youngs modulus and density. Figure 2.3(b) shows a surface plot for f_1 as a function of E and ρ for n = 6, 10 and 12 layers. In this figure (as well as in similar figures to follow), subscripts 1 and 2 are used to denote the material phases. The localized crossover operator produces a perfectly linear improvement in the attenuation coefficient. This suggests an excellent agreement with the physics of the problem, as the dispersion is a result of the impedance mismatch at the interface of the layers. Therefore, as n increases, f_1 should keep decreasing. While an increase in both the Youngs modulus and density ratios leads to an almost monotonic decrease in the objective that is to be minimized, the density ratio is shown to have a stronger impact.

Figure 2.4 shows the results for the f_2 objective function, given in [Eq. 2.21]. For the selected ratio of E and ρ presented in Fig. 2.4(a), the localized operator generates better designs compared to all other operators. However, as n exceeds 10 layers, f_2 levels out around 5%. This could be due to reaching the Bragg limit of the design, which means a global optimal, but a more rigorous mathematical proof is needed. For the surface plot, the Youngs modulus and density ratios appear to have an almost identical effect on the objective value. The rate at which the objective value decreases is very high at low values of phase property contrast, indicating that the benefits of increasing the contrast and the number of layers begin to diminish at ratios of around 5 to 6.

Although, f_3 is the most studied objective function in the optimization literature of both photonic and phononic crystals in two- and three-dimensions, Fig. 2.5 contains rather shocking
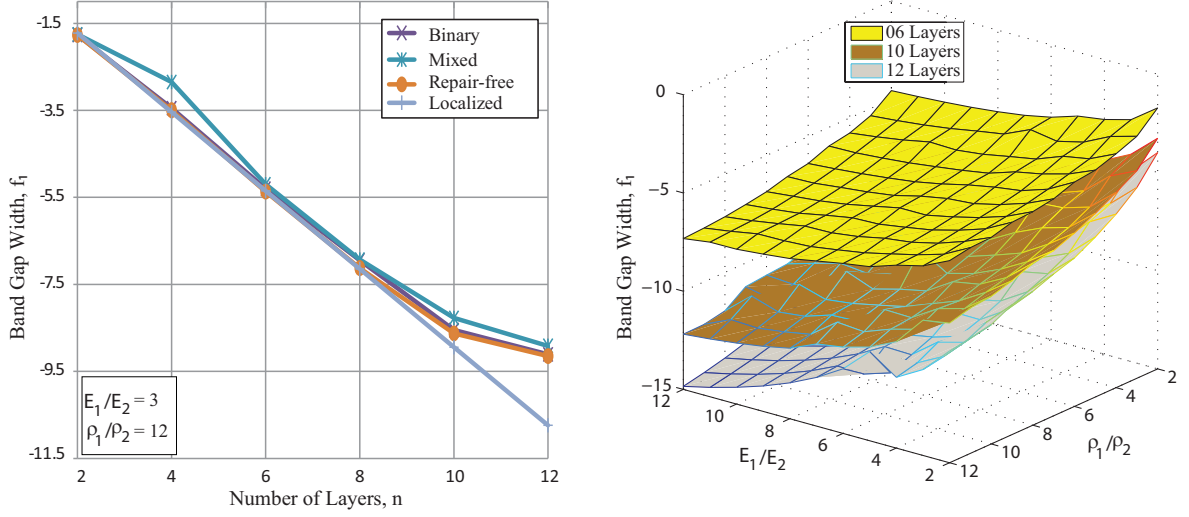
Figure 2.3: (a) Pareto diagram for the maximization of stop-band attenuation at $\Omega^* = 20$ for different number of layers at given ratio of ρ and E, (b) Surface plot of the same objective f_1 as a function of the ratio of material properties for 6, 10 and 12 layers.
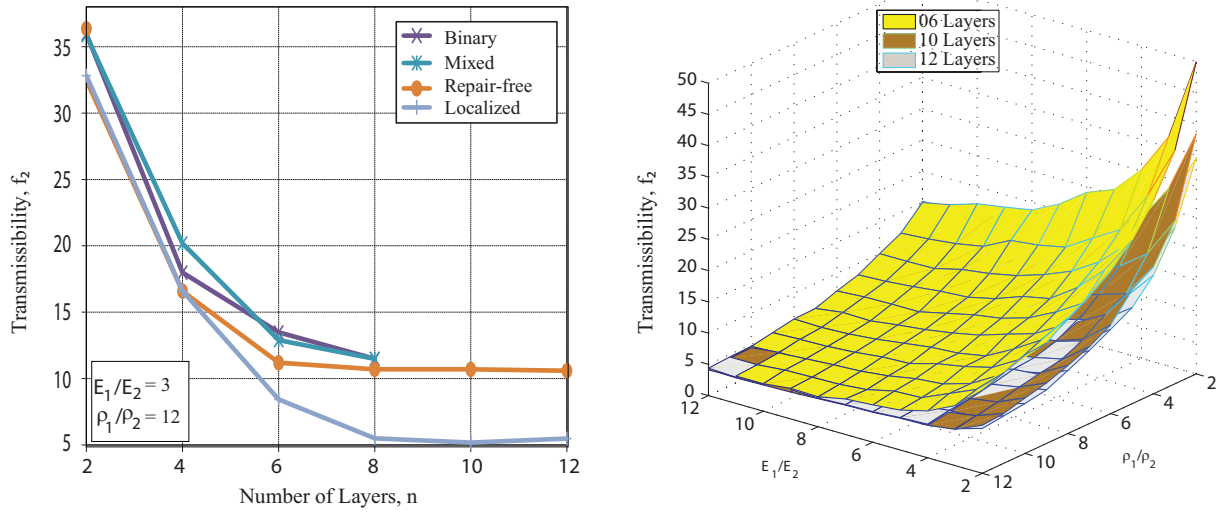
Figure 2.4: (a) Pareto diagram for the minimization of transmissibility for a broadband pulse spanning $0 \leq \Omega^* \leq 50$ for different number of layers at given ratio of ρ and E, (b) Surface plot of the same objective f_2 as a function of the ratio of material properties for 6, 10 and 12 layers.

and counter-intuitive results. Both (a) and (b) subplots show no significance of the number of layers on f_3 across all the different material ratios. In some cases, the 2-layer designs are better than the

ones with more design variables (i.e., n). Therefore the obtained designs with only two-layers are global optima. This means that two layers can open the widest band gap, normalized to its central frequency. When we try to add more layers to the design, this requires reducing the width of the layers, which decreased the affected wave length and the band gap width in the same time.
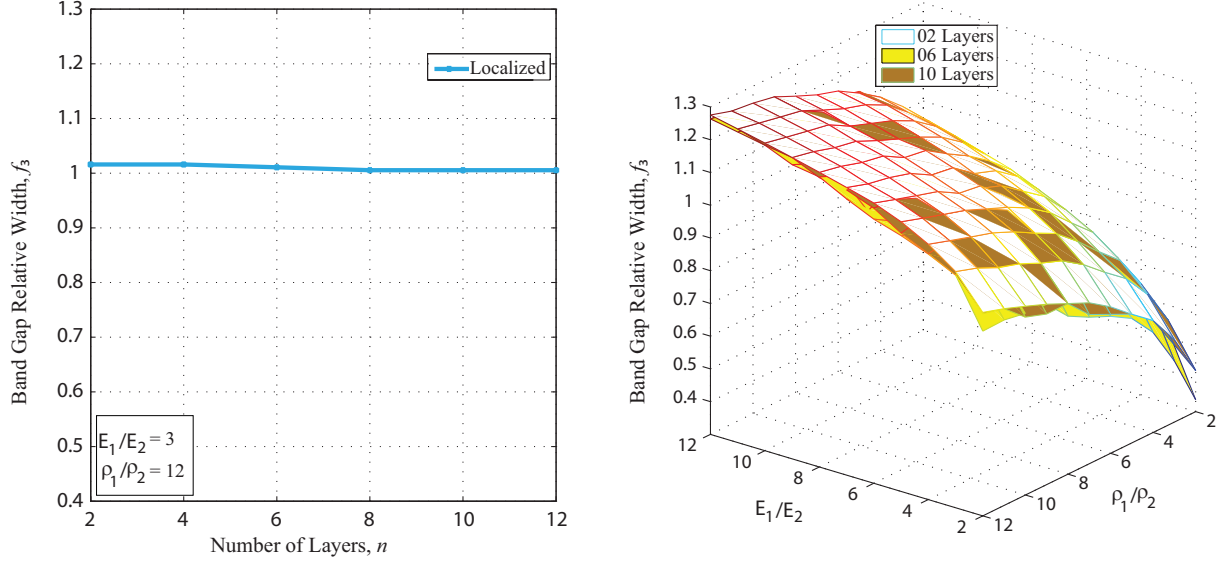
Figure 2.5: (a) Pareto diagram for the maximization of the width of the first stop-band normalized to its central frequency for different number of layers at given ratio of ρ and E, (b) Surface plot of the same objective f_3 as a function of the ratio of material properties for 2, 6 and 10 layers.

The optimization results of objective function f_4, given in [Eq. 2.23], is presented in Fig. 2.6. Both Youngs modulus and density ratios appear to have similar effect on the objective value. This time the optimizer was able to discover better designs with bigger n and the number of layers begin to have a profound effect at ratios bigger than 5 to 6.

2.8   Conclusion

The problem of unit cell topology optimization for multi-phase layered phononic materials has been formulated and a novel localized scale-preserving, repair-free representation has been implemented. The results show an improvement in the band gap width at a fixed frequency value of 17% compared to [68]. For the second objective considered here (i.e., transmissibility), an improve-
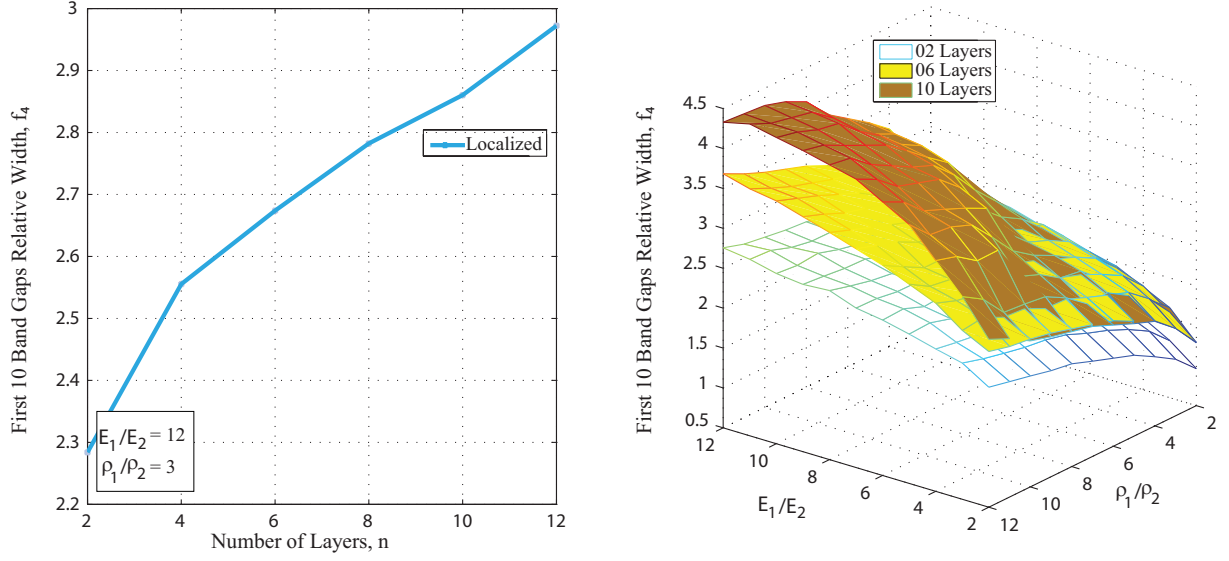
Figure 2.6: Pareto diagram for the maximization of the summation of the width of the first 10 stop-bands normalized to their central frequency for different number of layers at given ratio of ρ and E, (b) Surface plot of the same objective f_4 as a function of the ratio of material properties for 2, 6 and 10 layers.

ment of 48% was achieved with the localized operators compared to [12, 64]. Surprising results were obtained for f_3. The results for f_4 showed a consistent increase due to adding more layers to the design space. This representation efficiently characterizes the design of layered phononic materials consisting of two or more material phases. The objectives considered dealt with frequency isolation of both single harmonic and broadband waves. Finally, series of large-scale evolutionary optimization computations have been conducted to explore the dependence of the optimal objective value upon the ratio of Young's modulus and density for phononic materials.

Chapter 3

Topology optimization of two- and three-dimensional phononic crystals[1]

3.1 Abstract

We consider two-dimensional phononic crystals formed from silicon and voids, and present optimized unit-cell designs for the following modes of elastic wave propagation: (1) out-of-plane, (2) in-plane, (3) combined out-of-plane and in-plane, and (4) flexural (on the basis of Mindlin plate theory). To feasibly search through an excessively large design space ($\sim 10^{40}$ possible realizations) we develop a specialized genetic algorithm and utilize it in conjunction with the reduced Bloch mode expansion method for fast band-structure calculations. Focusing on high-symmetry plain-strain square lattices, we report unit-cell designs exhibiting record values of normalized band-gap size for all four categories. For the case of combined polarizations, we reveal a smoothened design with a normalized band-gap size exceeding 60%. For the thin-plate problem, a manufacturable design is presented with a normalized band gap in excess of 57%.

3.2 Introduction

Phononic crystals (PnCs) are periodic materials that exhibit distinct frequency characteristics, such as the possibility of the formation of *band gaps.* Within a band gap, wave propagation is effectively prohibited. This inherent dynamical phenomenon can be utilized in a broad range of technologies at different length scales. Applications of PnCs include elastic or acoustic waveguid-

---

[1] This chapter is drawn from Refs. [62, 36, 69] and has been adapted to suit the style and the notation of the dissertation.

ing [15] and focusing [18], vibration minimization [70], sound collimation [20], frequency sensing [71, 72], acoustic cloaking [25], acoustic rectification [73], opto-mechanical waves coupling in photonic devices [74], thermal conductivity lowering in semiconductors [75, 66, 76, 77], among others [78].

In general, it is most advantageous to have the frequency range of a band gap maximized while pulling its midpoint as low as possible in order to keep the unit-cell size to a minimum. Selecting the topological distribution of the material phases inside the unit cell provides a powerful means toward reaching this target, and this has been the focus of numerous research studies not only on PnCs but also photonic crystals (PtCs).

The exploration for optimal unit-cell designs was initiated by Cox and Dobson in 1999 [79] (in the context of PtCs). The articles by Burger *et al.* [80] and Jensen and Sigmund [81] provide reviews of subsequent studies concerned with band-gap widening in PtCs. In the area of PnCs, the problem has been treated in a variety of settings and by using several techniques. For example, unit cells have been optimized in one dimension [26, 12] and in two dimensions (2D) [27, 28, 29, 30, 31, 32] by using gradient-based [27, 28, 29, 30] as well as non-gradient-based [12, 31, 32] techniques. Interest in band-gap size maximization has also been treated outside the scope of the unit-cell dispersion problem [28, 82]. In all these optimization studies the focus has been primarily on PnCs based on an infinite thickness model and a material composition consisting of two or more solid (or solid and fluid) phases, with the exception of a few investigations that considered thin-plate single-phase models [29, 30, 83]. Recognizing the practical significance of solid-and-air PnCs with relatively large cross-sectional thicknesses, some studies considered the configuration of a 2D solid matrix with periodic cylindrical voids–modeled under 2D plain-strain conditions [84] or as a three-dimensional continuum with free-surface boundary conditions [85]–and investigated the dependence of band-gap size upon the void radius. For combined out-of-plane and in-plane waves in 2D infinite-thickness PnCs formed from silicon and a square lattice of circular voids, it has been shown that the band-gap size normalized with respect to the mid-gap frequency cannot exceed 40% [84]. On the other hand, for thin-plate flexural waves, the largest normalized band-gap size reported for a practical

(i.e., manufacturable) unit cell is approximately 16% [30]. In this paper we utilize a specialized optimization algorithm in pursuit of the best unit-cell solid-void distributions for the 2D plain-strain and thin plate problems considering high-symmetry square lattices [86]. We cover the cases of (1) out-of-plane waves, (2) in-plane waves, (3) combined out-of-plane and in-plane waves, and (4) flexural waves on the basis of Mindlin plate theory [87, 88].

3.3 Governing equations

The governing continuum equation of motion for a heterogeneous medium is

$$\nabla \cdot \mathbf{C} : \frac{1}{2}[\nabla \mathbf{u} + (\nabla \mathbf{u})^{\mathrm{T}}] = \rho \ddot{\mathbf{u}}, \tag{3.1}$$

where $\mathbf{C}$ is the elasticity tensor, ρ is the density, $\mathbf{u}$ is the displacement vector, $\mathbf{x} = \{x, y, z\}$ is the position vector, ∇ is the gradient operator, ":" is the double contraction operation, and $(.)^{\mathrm{T}}$ is the transpose operation. We assume the wave propagation to be confined to the x-y plane only, that is, $\partial \mathbf{u}/\partial z = 0$. As such, we have two independent sets of equations, one for out-of-plane motion and the other for in-plane motion. To obtain the band structure for a given PnC unit-cell design we assume a Bloch solution to the governing equations in the form $\mathbf{u}(\mathbf{x}, \mathbf{k}; \mathbf{t}) = \tilde{\mathbf{u}}(\mathbf{x}, \mathbf{k})e^{i(\mathbf{k}.\mathbf{x}-\omega \mathbf{t})}$, where $\tilde{\mathbf{u}}$ is the Bloch displacement vector, $\mathbf{k}$ is the wave vector, ω is the frequency, and t is the time.

The governing equation of motion for thin plates based on Mindlin theory [87, 88] is:

$$\left(\nabla^2 - \frac{\rho}{\mu\kappa}\frac{\partial^2}{\partial t^2}\right)\left(D\nabla^2 - \frac{\rho h^3}{12}\frac{\partial^2}{\partial t^2}\right)\bar{w} + \rho h\frac{\partial^2 \bar{w}}{\partial t^2} = 0 \tag{3.2}$$

where h is the plate thickness, μ is the shear modulus, $D = (Eh^3)/[12(1-\nu^2)]$ is the plate stiffness, E is the Young's modulus, ν is the Poisson's ratio, κ is the shear correction factor and $\bar{w} = \bar{w}(x, y, t)$ is the plate's transverse displacement.

Due to lattice symmetry the analysis is restricted to the first Brillouin zone. We consider square lattices and furthermore impose C_{4v} symmetry at the unit-cell level. Subsequently, design representation is needed in only a portion of the unit cell and the band-structure calculation is

limited to the corresponding irreducible Brillouin zone (IBZ). Furthermore, we model only the solid portion of the unit cell. The void portion is not modeled since we permit only contiguous distribution of solid material. In this manner the PnCs considered to exhibit geometric periodicity (with free internal in-plane surfaces) and not material periodicity. In practice, the voids will be either in a vacuum or filled with air. Our model presents an adequate representation of both cases because the elastic waves propagating in the solid will have the dominating effect [85]. In fact, this also suggests that the results we show are practically independent of the choice of the solid material. We numerically solve the emerging eigenvalue problem using the finite-element (FE) method utilizing four-node bilinear quadrilateral elements. In addition, the reduced Bloch mode expansion (RBME) method [89, 90] is applied to the FE model to substantially speed up the band-structure calculations throughout the optimization process. In the RBME implementation we use a two-point expansion scheme. The final reported results, however, are based on full (non-reduced) calculations.

3.4   Unit cell analysis

We represent a square unit cell Y, of side length a, by $n \times n$ pixels forming a binary matrix G. This matrix is then reduced to a vector, g, following the underlying unit-cell symmetry. Each of the pixels can be assigned to either a no-material (void) or a material (silicon), i.e., $g_s \in \{0, 1\}$. Throughout all the intermediate steps of the optimization process, we treat the void pixels as a highly compliant medium as this enables us to conveniently manipulate the unit-cell designs. Once the optimization is complete, we assess the final designs by modeling only the silicon portion of the unit cell as described above.

The objective function is formulated in terms of the size of a particular band-gap width normalized with respect to its midpoint frequency:

$$f(g) = \frac{max(min_{j=1}^{n_k}(\omega_{i+1}^2(k_j, g)) - max_{j=1}^{n_k}(\omega_i^2(k_j, g)), 0)}{(min_{j=1}^{n_k}(\omega_{i+1}^2(k_j, g)) + max_{j=1}^{n_k}(\omega_i^2(k_j, g)))/2}, \tag{3.3}$$

where $min_{j=1}^{n_k}(\omega_i^2(k_j, g))$ and $max_{j=1}^{n_k}(\omega_i^2(k_j, g))$ denote the minimum and maximum, respectively,

of the ith frequency ω_i over the entire discrete wave-vector set, $k_j, j = 1, \ldots, n_k$, tracing the border of the IBZ. The band gap exists only when the minimum of the $(i+1)^{th}$ branch is greater than the maximum of the ith branch; otherwise no band gap exists.

3.5 Unit cell optimization

We employ a genetic algorithm (GA) to maximize $f(g)$. A GA is a nature-inspired optimization technique that mimics biological evolution. It generally starts with a pool of candidate solutions (i.e., designs) according to a certain objective (fitness) function, then applies a group of operators, namely, selection, crossover, and mutation, in order to evolve to more fit designs (i.e., with higher objective function values). Compared to gradient-based methods, GAs are less likely to get trapped into local minima, especially for problems with vast search spaces, hyper dimensions, and a large number of variables [91], as is the case in our unit-cell optimization problem.

In our GA, the initial population of unit-cell designs is set up to be random to avoid any initial bias that might negatively affect the search. Since it is unlikely to have a band gap at the onset, we define the fitness function F_l, of the unit-cell design as follows:

$$F_o = H_o + \phi_1 f_o(g), \tag{3.4}$$

$$F_i = H_i + \phi_1 f_i(g), \tag{3.5}$$

$$F_c = H_o + \phi_1 f_o(g) + \phi_2 H_i + \phi_3 f_c(g), \tag{3.6}$$

$$F_f = H_f + \phi_1 f_f(g), \tag{3.7}$$

where the subscript l is equal to o, i or c to denote the wave type (i.e., either out-of-plane, in-plane, or combined), ϕ_{1-3} are constants equal to $10^4, 10^8, 10^{15}$, respectively, introduced to set priorities during the evolution process, and H_l is a step function defined as:

$$H_l = \begin{cases} 0 & \text{if } f_l(g) > 0 \quad \text{(band gap exists)} \\ A & \text{if } f_l(g) = 0 \quad \text{(no band gap)} \end{cases} \tag{3.8}$$

In Eq. (3.6) f_c denotes the objective function modified to represent the normalized band-gap size for the combined waves case. In Eq. (3.8) A represents a measure of the "area" in frequency-wavenumber space between the two consecutive dispersion branches of interest:

$$A = \sum_{j=1}^{n_k} \left[(\omega_{i+1}^2(k_j, g)) - (\omega_i^2(k_j, g)) \right] \tag{3.9}$$

The only condition enforced in the initial population is that adjacent pixels of the same material type appear in pairs in each row. Throughout the evolution, tournament selection and single-point crossover are the two types of operations applied on any given pair of "parent" unit-cell designs. Following the unit-cell symmetry constraint, the "offspring" mutates according to a specific probability using the following rule: Select random pixel x; if $\sum_{r=-1}^{1} g_{x+r} > 1$, set each of the three pixels to one, otherwise, to zero. The GA terminates when no further improvement in the objective function value is noted for a prescribed number of generations. At the end of the search, the final unit-cell topology passes through a simple one-point flip local search for fine tuning and smoothening.

3.5.1   Lead-follow algorithm

The combined out-of-plane and in-plane optimization problem poses a challenge in setting up the objective function because it is based on two sets of independent equations. Here we adopt a unique strategy, which we refer to as a *lead-follow* algorithm, whereby the search for a combined band gap is tackled in a two-stage fashion during the evolution process. The algorithm starts with a set of random designs and searches for a band gap for out-of-plane waves (the *leader*) between two prescribed branches guided by Eq. (3.9) for indication of design quality. Once the GA opens a gap, it shifts its focus to the in-plane waves (the *follower*), but now the branch numbers encompassing the band gap are not prescribed–they are determined by the same frequency range that spans the band gap of the leader wave type. The objective function for the follower wave type is also guided by the "area" as given by Eq. (3.9). This lead-follow process continues until a combined band gap is found, at which point the objective function effectively switches to being the actual value of the

normalized combined band gap. This process is automated through a generalized fitness function given in Eq. (3.6). We note that, in principle, the identity of the leader and the follower may be reversed.

3.6   Results

In applying the specialized GA we considered the following properties for isotropic silicon (λ and μ denote Lame's coefficients): $\rho_s = 2330$ kg/m^3, $\lambda_s = 85.502$ GPa, $\mu_s = 72.835$ GPa, and we used a resolution of $n = 32$. At this resolution, the total number of possible material distributions within the unit-cell domain is 8.7×10^{40}. This highlights the tremendously large search space that the GA needs to navigate through. At the end of each complete GA run, we doubled the resolution of the emerged topology to become 64×64 pixels, and then smoothened the topology (while keeping it pixelated) by following a few simple rules. For the third case (i.e., combined waves) a splines-based solid material distribution has been subsequently generated to represent a manufacturable design. Figure 1 presents the unit-cell topologies and band structures of the optimized unit cells for the four cases, and Table I lists the objective values obtained. In our results we identify a band-gap number by the number of the optical branch that borders it from the top.

Table 3.1: Normalized band-gap (BG) size for the optimized unit cells

Wave Type	Out-of-Plane		In-Plane	Combined		Flexural
BG number	1st	2nd	2nd	Lowest		1st
Representation	Pixels	Pixels	Pixels	Pixels	Splines	Pixels
Norm. BG size	1.2270	1.1132	0.7696	0.6259	0.6021	0.5758

The optimized unit-cell topologies for out-of-plane waves [Figs. 1(a) and (b)] show contiguous solid media approaching the limiting case of isolated square or circular inclusions. This limiting case represents the optimal conditions for sonic crystals which admits only pressure waves [92]. For the presented case, the thin connections shown are needed to support the propagation of the shear elastic waves. The optimized topology for the in-plane waves problem [Fig. 1(c)], on the other hand, shows a mostly solid material with delicately shaped voids. This is consistent with

the understanding in the literature that solid material with isolated voids represents the optimal conditions for band-gap opening for in-plane waves [92]. We note that no band gap appeared below the first optical branch due to the difficulty in preventing this branch from crossing through the acoustic branches. The optimal design for the combined case [Fig. 1(d)] appears to be a blend (although non-intuitive in shape) among the out-of-plane and in-plane design traits. We also note that for this design the band gap for in-plane waves is of size $f_i = 1.0979$, which is higher than the value we obtained in Fig. 1(c). This suggests that the lead-follow algorithm has utility for also single-wave type optimization. Upon appropriate size scaling to the frequency range of interest, all designs are amenable to fabrication by splines-based smoothening with minimal loss in objective value [as demonstrated in Fig. 1(e)]. For the thin-plate flexural waves case [Fig. 1(f)], the optimized design for the first band gap features a frame-like topology that is simple and manufacturable. To compare the performance of this design with the optimized, and manufacturable, thin plate unit cell configuration reported by Halkjaer *et al.* [30], we recomputed the frequency band structure using the same material ($\rho_p = 1200$ kg/m^3, $E_p = 2.3$ GPa, $\nu_p = 0.35$) and geometric ($h = 0.0909a$) properties they used. We found the normalized band gap size to be 0.5639 which is more than three times higher in value despite that fact that the present design is based on a square lattice and the design provided in Halkjaer *et al.* [30] is based on a hexagonal lattice (which is generally known to give larger band gaps).

3.7   Conclusions

We have conducted phononic crystal unit-cell topology optimization for the following modes of elastic wave propagation: (1) out-of-plane, (2) in-plane, (3) combined out-of-plane and in-plane, and (4) flexural (on the basis of Mindlin plate theory). When compared to corresponding solid-void PnC unit-cell configurations reported in the literature, each of the designs shown in [Fig. 1] represent a record value of normalized band-gap size in its category. While the focus in this work has been on phononic crystals, our search methodology is also applicable to the parallel problem of 2D PtCs optimization, where transverse-electric and transverse-magnetic waves may be considered
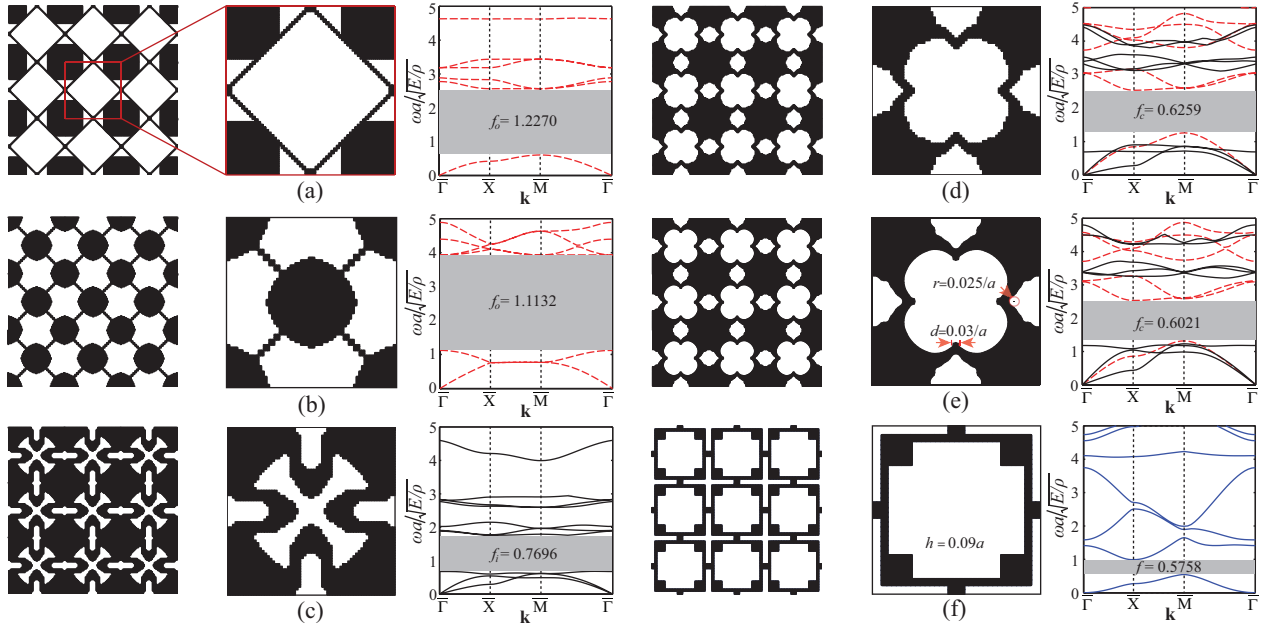
Figure 3.1: Optimized unit cell design and band structure for out-of-plane waves: (a) First band gap, (b) second band gap; in-plane waves: (c) second band gap; combined out-of-plane and in-plane waves, lowest band gap: (d) pixels, (e) splines; and (f) thin-plate flexural waves: first band gap. The minimum feature size, d, and minimum radius of curvature, r, are identified in (e). For the thin plate problem, the plate thickness is $h = 0.09a$ as shown in (f). All band gaps are shaded in gray.

separately [93] or in combination [94] .

Acknowledgment

Chapter 4

Trampoline metamaterials: Local resonance enhancement by springboards[1]

Abstract: We investigate the dispersion characteristics of locally resonant elastic metamaterials formed from the erection of pillars on the solid regions in a plate patterned by a periodic array of holes. We show that these solid regions effectively act as springboards leading to an enhanced resonance behavior by the pillars when compared to the nominal case of pillars with no holes. This local resonance amplification phenomenon, which we define as the *trampoline effect*, causes subwavelength band gaps to increase in size by roughly a factor of 4. This overcome facilitates the utilization of subwavelength metamaterial properties over exceedingly broad frequency ranges.

4.1   Introduction

Phononic crystals and locally resonant acoustic/elastic metamaterials have been the focus of extensive research efforts in recent years due to their attractive dynamical characteristics, such as the possibility of exhibiting band gaps. In a phononic crystal, band gaps are generated by Bragg scattering for which an underlying constraint is that the wavelength has to be on the order of the lattice spacing. [7, 9] In a locally resonant acoustic/elastic metamaterial, on the other hand, band gaps may be generated by the mechanism of hybridization between local resonances and the disperion properties of the underlying medium, and this in turn may take place at the subwavelength regime. [8]

---

[1] This chapter is drawn from Ref. [63] and has been adapted to suit the style and the notation of the dissertation.

While in principal periodicity is not a necessity in a metamaterial, the introduction of the locally resonant elements in a symmetric fashion enables intrinsic, unit-cell based, description of the wave propagation characteristics, in addition to attaining the benefits of order and compactness. The presence of periodicity, in itself, produces direction-dependent frequency bands and band gaps (caused by Bragg scattering). These unique dispersion properties may sufficiently be utlized in numerous applications involving wave filtering, [10, 11, 12] localization, [13, 14] guiding, [14, 15] focusing, [16, 17, 18] collimation, [19, 20] among others. The added feature of local resonance, however, gives rise to a qualitatively different type of dynamical behavior, such as negative effective elastic moduli and/or density, [95, 96, 97, 98] along with the possibility of generation of subwavelength band gaps.[8] The applications of locally resonant acoustic/elastic metamaterials are, in turn, far from conventional, e.g., subfrequency wave isolation, [21] subwavelength focusing and imaging, [22, 23] and cloaking, [25] to name a few. Crossing the boundaries of acoustics and elasticity, our group at CU-Boulder has recently proposed the utilization of locally resonant metamaterials for the control of heat in a semiconducting thin-film. [99] Regardless of the application, one of the generally desirable characteristics is for the metamaterial to exhibit a large band gap. While the problem of unit-cell optimization for maximum band-gap size has been actively pursued for phononic crystals, [28, 12, 62] less work has been done in exploring new approaches for band-gap enlargement in locally resonant acoustic/elastic metamaterials.

One of the practical realizations of locally resonant elastic metamaterials is the construction of a periodic array of pillars on a plate [100, 101]. In this configuration, the pillars by virtue of their dynamic stiffness serve as the local resonators as they are essentially rod/beam-like structures laid out on a flexural foundation. The diameter and height of the pillars determine their resonant frequencies, and the extent of coupling of the pillar modes with the foundational plate modes is dependent primarily on the plate stiffness and thickness as well as the lattice spacing of the pillars.

(a)

(b)

(c)

$t = a/5$
$d_\mathrm{h} = 5a/8$

$t = a/5$
$d_\mathrm{p} = 5a/8$
$h_\mathrm{p} = 3a/5$

$t = a/5$
$d_\mathrm{p} = d_\mathrm{h} = 5a/8$
$h_\mathrm{p} = 3a/5$

(d) Holes Only

(e) Pillars Only

(f) Trampoline

$\Delta\omega/\omega_c = 0.19$

$\Delta\omega/\omega_c = 0.48$
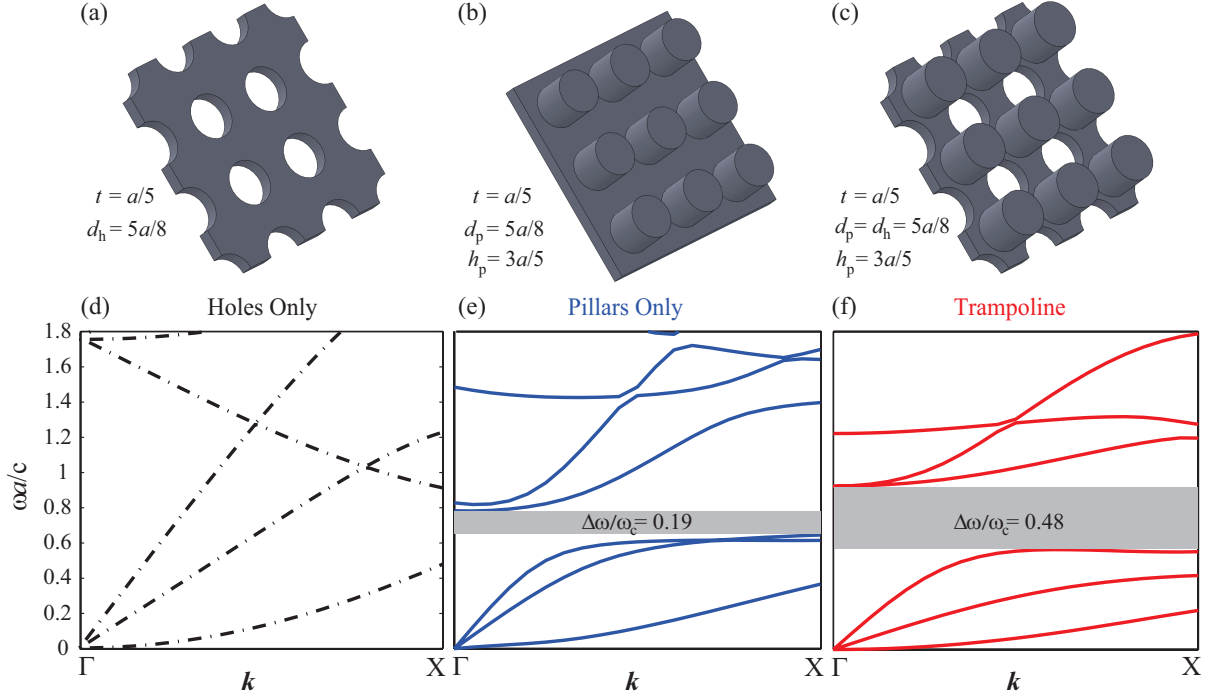
Figure 4.1: Illustration of the concept of a trampoline metamaterial. The top row displays schematics of (a) a standard phononic crystal (consisting of a periodic array of holes in a plate), (b) a standard pillared elastic metamaterial (consisting of a periodic array of pillars on a plate), and (c) a trampoline metamaterial (consisting of a periodic array of pillars on a plate intertwined with a periodic array of holes). The frequency band structure of the three configurations in the ΓX direction is shown in the bottom row. In the frequency range displayed, the phononic crystal has no band gaps (d), the standard pillared metamaterial exhibits a subwavelength band gap with a relative size of 0.19 (e), and the proposed trampoline metamaterial exhibits an enhanced subwavelength band gap with a relative size of 0.48.

4.2   Proposed concept

Driven by the desire for band-gap amplification, in this work we propose a configuration formed by merging a periodically pillared structure, based on a plate foundation (Fig. 4.1b), with a standard phononic crystal formed by removal of a periodic array of holes in a plate (Fig. 4.1a). The emerging configuration is a locally resonant elastic metamaterial consisting of pillars erected on the solid regions of a phononic crystal plate (Fig. 4.1c). In this configuration, each pillar is now rooted in a more compliant base due to the presence of the holes. This base effectively acts as a *springboard* that allows the pillars' resonant motion to be enhanced. Due to the analogy to a

recreational trampoline, we refer to this hybrid configuration as a *trampoline metamaterial* and to the underlying mechanism as the *trampoline effect.*

To examine the behavior of the proposed trampoline metamaterial, we investigate the band structure characteristics for the propagation of Lamb waves in the three types of periodic materials shown in Figs. 4.1a-4.1c. We choose silicon as the constitutive material ($\rho = 2330\ Kg/m^3$, $\lambda = 85.502$ GPa, $\mu = 72.835$ GPa) and for all configurations consider a plate thickness of $t = a/5$ where a is the lattice spacing. We set both the hole and pillar diameters as $d_h = d_p = 5a/8$, and the pillar height as $h_p = 3a/5$. Using the theory of elasticity, we set up the equations of motion for all three models in the form $\nabla \cdot \mathbf{C} : \nabla^{\mathrm{S}}\mathbf{u} = \rho\ddot{\mathbf{u}}$ where $\mathbf{u}$ is the displacement vector, $\mathbf{C}$ is the elasticity tensor, ρ is the density, ∇^{S} is the symmetric gradient operator defined as $\nabla^{\mathrm{S}} = \left(\nabla\mathbf{u} + \nabla(\mathbf{u})^{\mathrm{T}}\right)/2$ and the dot is the inner product symbol. Denoting the position vector by $\mathbf{x}$, the wavevector by $\mathbf{k}$, the frequency by ω and the time by t, we apply Bloch's theorem, $\mathbf{u}(\mathbf{x}, \mathbf{k}; t) = \mathbf{u}(\mathbf{x}, \mathbf{k})e^{i(\mathbf{k}^T\mathbf{x}-\omega t)}$, to the equations of motion and obtain [89]

$$\nabla.\mathbf{C} : \left[\nabla^S\tilde{\mathbf{u}} + \frac{i}{2}(\mathbf{k}^T \otimes \tilde{\mathbf{u}} + \mathbf{k} \otimes \tilde{\mathbf{u}}^T)\right] = -\rho\omega^2\tilde{\mathbf{u}}, \tag{4.1}$$

where $\tilde{\mathbf{u}}$ is the Bloch displacement vector and the symbol $\otimes$ denotes the outer product. With the application of periodic boundary conditions on $\tilde{\mathbf{u}}$, Eq. 4.1 forms the Bloch eigenvalue problem. We solve this problem using the finite element method and obtain the band structure for each of the three configurations, which we show also in Fig. 4.1 for the standard phononic crystal (Fig. 4.1d), the standard pillared elastic metamaterial (Fig. 4.1e) and the proposed trampoline metamaterial (Fig. 4.1f). In all our dispersion diagrams, the frequency is expressed as $\omega a/c$ where $c = \sqrt{E/\rho}$. We observe that the relative size of the locally resonant subwavelength band gap (along the ΓX direction) gets enlarged in size by a factor of approximately 2.5 when we compare the results of the trampoline metamaterial to the standard pillared elastic metamaterial. When examining the presence of a complete band gap along the ΓXMΓ path of the irreducible Brillouin zone, we find that the standard pillared elastic metamaterial has no band gap, whereas the trampoline metamaterial exhibits a band gap with a relative size of 0.026 (see Fig. 4.2). This outcome, for both the partial

and complete band gaps, is due to the increased compliance of the pillar foundation (i.e., the pillar's plate base) due to the presence of the holes. The holes cut through the elastic foundation, reducing its area, and consequently allow not only the main body of the pillars to resonate but also portions of the foundation—or root—that each pillar is attached to. As such, the segments of the plate material between the holes effectively act as springboards that allow each pillar to resonate more intensely as they themselves contribute to the resonant motion.
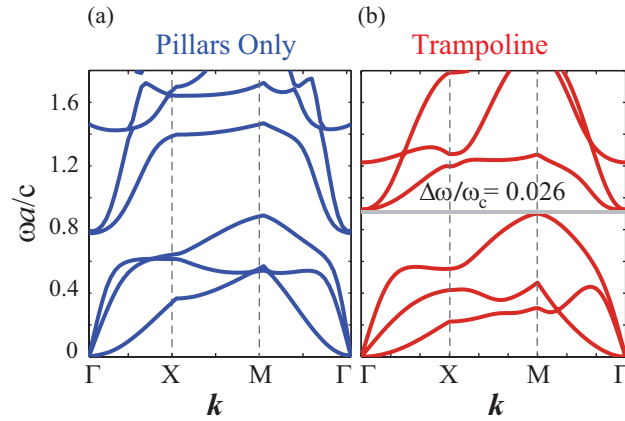
Figure 4.2: Band structure along the entire $\Gamma X M \Gamma$ path of the irreducible Brillouin zone for cases shown in Figs. 4.1b and 4.1c. The standard pillared elastic metamaterial has no complete band gap, while the trampoline metamaterials has a band gap with a relative size of 0.026.

4.3   Parametric optimization

To further examine the trampoline effect, we analyze the problems shown in Figs. 4.1b and 4.1c but now for a range of values of pillar height and hole diameter. Figure 4.3a presents a map of the size and location of the lowest band gap (also along the ΓX direction) as a function of pillar height for $d_h = 5a/8$. The same results are again presented in Fig. 4.3b but in the form of a plot of relative band-gap size, $\Delta\omega/\omega_c$, versus pillar height, where ω_c the band-gap central frequency. We focus our attention to $d_p/a \geq 0.4$ because at lower pillar heights the lowest resonance frequency is high enough to interact with the Bragg scattering regime (which is outside the scope of this Letter). The blue solid line in Fig. 4.3b is for the standard pillared elastic metamaterial. We observe that
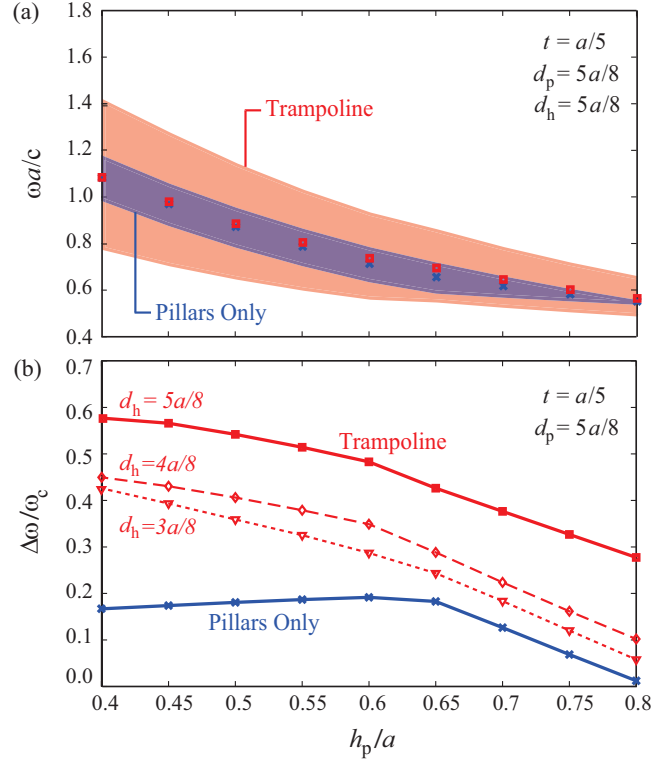
Figure 4.3: Map of absolute (a) and relative (b) band gap as a function of normalized pillar height for a trampoline metamaterial compared to a standard pillared metamaterial. The trampoline effect results in a magnification of the subwavelength locally resonant band gap by a factor ranging from roughly 2 to 4 for geometries where the original $\Delta\omega/\omega_c$ is greater or equal to 0.1.

as the pillar height for this "pillars only" case increases, the relative band-gap size also increases but only up to the point where $h_p/a = 0.65$, after which it descends in value. This non-monotonic behavior is due to the coupling of the pillar vibrations with the flexural motion of the base plate, which becomes more profound as h_p/a increases. The dotted, dashed and solid red lines represent the relative band-gap size for the trampoline metamaterial configuration for different values of d_h. In addition to $d_h = 5a/8$, two other hole diameters are considered, namely, $d_h = 3a/8$ and $d_h = 4a/8$ (noting a constant increment of $a/8$ between the three diameters). We observe that for the two additional trampoline metamaterial cases, the relative band-gap size is larger than the case of "pillars only". This shows that the trampoline effect is present also in the lower hole diameter cases. It is noteworthy, however, that the incremental enlargement of relative band-gap size is more significant at higher values of hole diameter, which is explained by the quadratic decrease in

springboard area as d_h is increased. We also observe that all three cases display a monotonic trend suggesting that the coupling between the pillars and the base plate is significant across the entire range of h_p/a considered, which is a characteristic of the trampoline effect. At h_p/a values less than 0.4, the relative band gap size for the trampoline metamaterials decreases, with this backward descend initiating at different points depending on d_h.

Most noticeable in Fig. 4.3 is the remarkable values of relative band gap size that are attainable by the trampoline metamaterials. For the parameter set of $d_h = 5a/8$ and $h_p/a = 0.4$, the size of the relative band gap is close to 0.6 (i.e., 60%). This is a significant improvement over reported relative band gap sizes in the literature for acoustic/elastic metamaterials in general and specifically for pillared metamaterials, which usually fall within the range of $20\% - 30\%$ for a partial band gap. [100, 101] Concerning the entire ΓX$M\Gamma$ wavevector path, we note that for all the h_p/a values considered in Fig. 4.3, there is a complete band gap for the standard pillared metamaterial, but only within the range of $0.40 \leq h_p/a < 0.50$ with a maximum relative size of 0.11 at $h_p/a = 0.40$. For the trampoline metmaterial, on the other hand, a complete band gap exists within the range $0.40 \leq h_p/a < 0.62$ with a maximum relative size of 0.17 at $h_p/a = 0.40$. Thus the trampoline effect both increases the size of the complete band gap and extends the h_p/a range of its existance$-$an outcome that is favorable for many subwavelength applications that require wave attenuation both at a broad frequency range and along all spatial directions.

The trampoline effect can be further examined by viewing the Bloch mode shapes. A thorough analysis on the changes to the Bloch mode shapes when pillars are added to a uniform plate has been done by Wu and coworkers [101]. Here we focus only on the effects of adding holes to an already pillared plate. Figure 4.4 displays Bloch mode shapes for the standard "pillars only" case (Fig. 4.4a) and the trampoline case (Fig. 4.4b) at $k_x = 0.62\pi/a$ (where k_x denotes the wavenumber along the ΓX direction) for the third acoustic branch shown in Figs. 4.1e and 4.1f. In the figure, the total displacement is normalized by its own maximum value and the colormap represents the spatial distribution of the von Mises stress (in log scale). It can be noticed that in the case of the standard pillared elastic metamaterial (Fig. 4.4a), the stress is concentrated within the main body

(a) Pillars Only (b) Trampoline
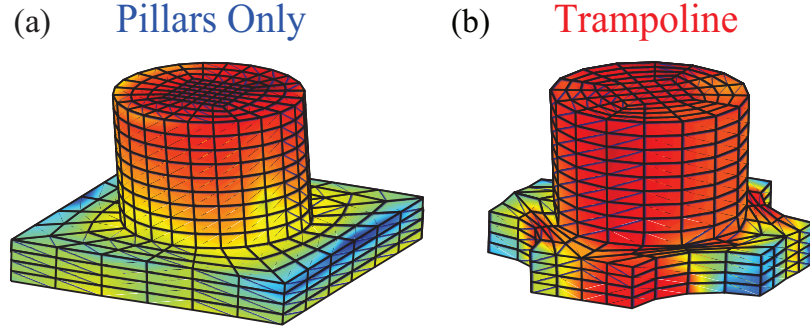
Figure 4.4: Bloch mode shapes at $k_x = 0.62\pi/a$ for (a) standard pillared metamaterial and (b) trampoline metamaterial. The colormap represents the spatial distribution of the von Mises stress (in log scale).

of the pillar with very moderate stress levels in the base plate. This implies that there is little motion in the pillar foundation, and that the resonant motion is taking place mostly in the main body of the pillar. On the other hand, in the case of the trampoline metamaterial (Fig. 4.4b), the stress distribution is high within both the main body of the pillar and in its foundation. This contrast in response confirms that the introduction of the holes indeed renders the plate base to act as a springboard, and this induces the trampoline effect and causes the band-gap enlargement observed in Fig. 4.1f and in Fig. 4.3.

4.4   Conclusion

The proposed concept of a trampoline metamaterial provides promising opportunities for the many applications that require large band gaps. While the focus here has been on pillared elastic metamterials and subwavelength band gaps, the concept is in principle applicable to other configurations (e.g., replacing the pillars with heavy inclusions) and to superwavelength band gaps. For higher frequency band gaps, a mixing between the hybridizaton and Bragg scattering mechanisms could lead to even larger amplifications in band-gap size. Furthermore, topology optimization [28, 62] of the trampoline foundation for different lattice symmetries could be utilized to incur yet further increases in band-gap size.

Chapter 5

Flow control using phononic materials[1]

5.1 Abstract

In this chapter, a new application of phononic materials is investigated, namely, flow control. The goal is to utilize a phononic material to induce a change in a flow field in a desired manner. The phononic material model, the fluid model (provided by professor S. Biringen's group) and the coupling scheme between both are outlined. The ability to control disturbances in a flow field is demonstrated for three different case studies: (1) single frequency two-dimensional disturbance control (2) multiple-frequency two-dimensional disturbance control and (3) three-dimensional non-linear disturbance control.

5.2 Introduction

Flow control is the ability to manipulate and alter a flow field in a favorable manner [37]. The potential impact for a passive, inexpensive and practical technology for flow control is substantial. It can facilitate the delay/advancement of transition, prevention/provocation of separation and the suppression/enhancement of turbulence. By controlling one or more of these flow phenomena, it is possible to achieve lift enhancement, mixing augmentation, noise suppression and drag reduction among other benefits. In particular, realizing drag reduction can bring about a significant decrease

---

[1] The results and figures presented in this chapter are drawn from Refs. [102, 103, 104] with appropriate adaptation to suit the style and the notation of the dissertation. O. R. Bilal's contributions are in performance of research and analysis of data following the advising of Professor Mahmoud I. Hussein with a focus mostly on the phononics aspects. The collaborating team of Professor Sedat Biringen was mostly responsible for the fluid dynamics aspects of the research.

in transportation costs.

Numerous approaches have been studied in the literature to provide an effective flow control technology such as heating or cooling of surfaces, addition of ribs on the surface [105], suction and blowing [106, 107, 108], surface coating with a compliant material [40, 109, 43], among others [37]. Regardless of the approach for stimulating a change in flow behavior, successful control may be realized when particular desirable/undesirable flow structures and mechanisms are identified and clearly understood. One such mechanism is flow transition in a boundary layer or a channel flow, where unstable modes/disturbances are introduced and permitted to grow.

Owing to their wave-like nature, obstruction of the growth rate of these flow disturbances (i.e., their stabilization) is possible and may be induced by wave interferences. In low disturbance environments, the transition in channel and boundary layer flows begins when a two-dimensional (primary) instability, also known as the Tollmien-Schlichting (TS) wave [110], is triggered and becomes susceptible to three-dimensional disturbances at some finite amplitude. This is known as a secondary instability and is characterized by the appearance of three dimensional disturbance patterns that typically scale on the frequency and wavelength of the TS wave.

In this work, a condensed-matter physics treatment to fluid-structure interaction is introduced and a phononic material is utilized for flow control. The validity of this approach of passive flow control is demonstrated by replacing a portion of the rigid wall of a channel with an elastic periodic medium (e.g., a phononic crystal), located at one or more points or regions of interest along the fluid-structure interface, as shown in Fig. 5.1. The proposed approach is shown to effectively control both two-dimensional and three-dimensional disturbances.

5.3 Methodology

Numerous analyses are conducted on a 1D phononic crystal in order to realize an adequate design prior to conducting a coupled fluid-structure simulation. Different unit cell configurations composed of aluminum and ABS polymer are utilized. Following an uncoupled solid-model analysis, a coupled fluid-structure simulation is conducted to assess the performance of the phononic crystal
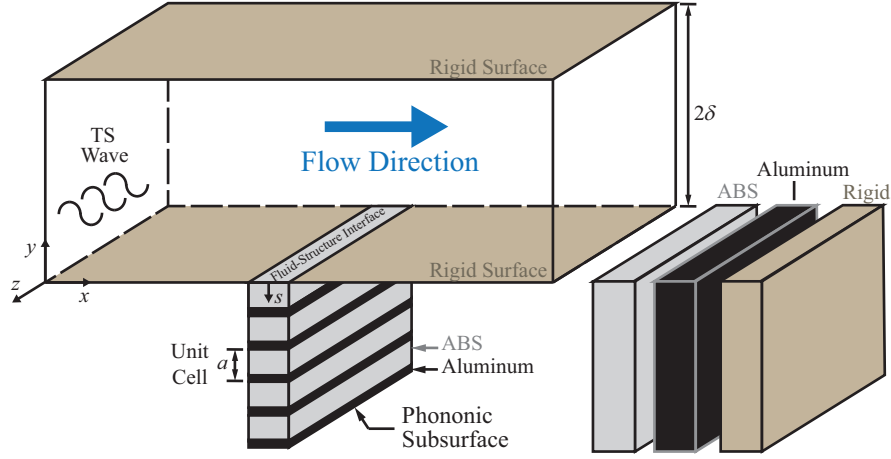
Figure 5.1: Schematic of plane flow channel with phononic subsurface covering a segment of the bottom wall. For comparison, replacement with a rigid wall or other materials are also considered.

in altering the flow characteristics as desired. To follow is a description of the solid and fluid models. In Section 5.4, the design approach and analyses are presented for the three different case studies considered. At the end of each case study, the design search space for the problem at hand involving the phononic crystal unit-cell design is presented.

5.3.1   Solid domain

The same modeling schemes outlined in Ch. 1, for dispersion, steady-state vibration and elastic wave propagation are implemented for a continuous periodic rod. The governing equation of motion for longitudinal wave propagation in a 1D heterogeneous linear elastic solid is

$$\rho_s \ddot{\eta} = (E\eta_{,s})_{,s} + f, \tag{5.1}$$

where $\eta = \eta(s,t)$, $f = f(s,t)$, $\rho_s = \rho(s)$ and $E = E(s)$ denote longitudinal displacement, external force, solid density and elastic modulus, respectively. The position coordinate and time are denoted by s and t, respectively. The operation $(.)_{,s}$ denotes differentiation with respect to position, while a superposed dot denotes differentiation with respect to time. The density, ρ_s and Youngs modulus, E, for each of these two constituent materials are: $\rho_{Al} = 2700$ Kg/m^3, $\rho_{ABS} = 1040$ Kg/m^3, $E_{Al} = 68.8$ GPa, $E_{ABS} = 2.4$ GPa.

To obtain the band structure for a given phononic subsurface unit-cell configuration, $f = 0$ is set in Eq. (5.1) and a Bloch solution in the form $\eta(s, t; \kappa) = \tilde{\eta}(s; \kappa)\mathrm{e}^{\mathrm{i}(\kappa s - \omega t)}$ is assumed, where $\tilde{\eta}$ is the Bloch displacement function, κ is the wavenumber, ω is the frequency, and $\mathrm{i} = \sqrt{-1}$, and periodic boundary conditions are applied, $\tilde{\eta}(s + L_{\mathrm{UC}}, \kappa) = \tilde{\eta}(s, \kappa)$, where L_{UC} is the unit-cell length.

For the finite structure problem, a boundary value problem (BVP) following Eq. (5.1) is set up for a finite phononic subsurface structure composed of n_c repeated unit cells of the type considered in the unit cell problem. The boundary conditions chosen are $\eta_{,s}(0, t) = 0$ and $\eta(l, t) = 0$ for the top and bottom ends, respectively, where $l = n_c L_{\mathrm{UC}}$. A harmonic forcing function is applied only at the top end, i.e., $f(0, t) = \bar{f}(0)\mathrm{e}^{\mathrm{i}\omega^* t}$ and $f(s, t) = 0$ for $s > 0$, where ω^* is the excitation frequency and $\bar{f}$ is the forcing amplitude. The harmonic displacement response is given by $\eta(s, t) = \bar{\eta}(s)\mathrm{e}^{\mathrm{i}\omega^* t}$, where $\bar{\eta}(s)$ is the response amplitude. Upon incorporation of the boundary conditions and the excitation function, and after substitution of the response function into Eq. (5.1), a frequency response function that describes the steady-state forced response of the structure is obtained. In this work, the number of unit cells is $n_c = 10$.

In addition, the finite structure is analyzed once again, but now as an initial boundary value problem (IBVP) whereby no assumptions are made on the temporal dependency of the displacement field. First, as an uncoupled system, the initial conditions $\eta(s, 0) = 0$ are considered and a harmonic force $f(0, t) = \bar{f}\sin(\omega^* t)$ is applied for the time interval $0 \leq t \leq t_{\mathrm{T}}$, where t_{T} is the total simulation time. As in the BVP, $f(s, t) = 0$ for $s > 0$. Second, for the coupled simulations, the same initial conditions are considered but no external force is applied; the forcing is induced by the interacting flow.

The 1D solid domain representing the phononic subsurface is numerically analyzed using the finite element (FE) method utilizing 1D 2-node iso-parametric elements. Upon discretization of the unit cell problem, a mass matrix, $\tilde{\mathbf{M}}$, and a stiffness matrix, $\tilde{\mathbf{K}}(\kappa)$ are obtained. Following the Rayleigh proportional damping model, the unit-cell damping matrix is defined as $\tilde{\mathbf{C}} = q_1 \tilde{\mathbf{M}} + q_2 \tilde{\mathbf{K}}$ where q_1 and q_2 are damping constants. The dispersion band structure is obtained by solving the eigenvalue problem $[-\omega^2 \tilde{\mathbf{M}} + \mathrm{i}\omega(q_1 \tilde{\mathbf{M}} + q_2 \tilde{\mathbf{K}}(\kappa)) + \tilde{\mathbf{K}}(\kappa)]\tilde{\mathbf{D}} = \mathbf{0}$, where $\tilde{\mathbf{D}} = [\tilde{d}_1 \ \tilde{d}_2 \ldots \tilde{d}_{n_m-1}]^{\mathrm{T}}$ is

the Bloch vector, for values of wavenumber in the range $0 \leq \kappa \leq \pi/L_{\mathrm{UC}}$. The number of nodes in the unit cell is denoted by n_m.

In the finite structure problems (BVP and IBVP), the FE method is used to spatially discretize the entire 10-unit-cell structure. For the IBVP, the second order Newmark scheme (presented in Ch. 1) is used for the time integration, with the incorporation of damping. The modified equations read as follow:

$$\mathbf{D}^{(i+1)} = \mathbf{D}^{(i)} + \Delta t \mathbf{V}^{(i)} + (\Delta t)^2 \left[\left(\frac{1}{2} - \beta \right) \mathbf{A}^{(i)} + \beta \mathbf{A}^{(i+1)} \right], \tag{5.2}$$

$$\mathbf{V}^{(i+1)} = \mathbf{V}^{(i)} + \Delta t \left[(1 - \gamma) \mathbf{A}^{(i)} + \mathbf{A}^{(i+1)} \right], \tag{5.3}$$

$$\mathbf{A}^{(i+1)} = \mathbf{T}^{-1} \left[-\mathbf{K} \mathbf{D}^{(i+1)} - \mathbf{C} \mathbf{V}^{(i)} - \frac{\Delta t}{2} \mathbf{C} \mathbf{A}^{(i)} + \mathbf{F}^{(i+1)} \right], \tag{5.4}$$

where $\mathbf{D}^{(i)}$, $\mathbf{V}^{(i)}$, $\mathbf{A}^{(i)}$, and $\mathbf{F}^{(i)}$ represent the displacement, velocity, acceleration, and force vectors at the ith time-step, respectively. Δt is the time step increment, and $\mathbf{T} = \mathbf{M} + \frac{\Delta t}{2} \mathbf{C}$. Here, $\mathbf{D}^{(i)} = [d_1^{(i)} \, d_2^{(i)} \ldots d_{n_s}^{(i)}]^{\mathrm{T}}$ and $\mathbf{F}^{(i)} = [f_1^{(i)} \, f_2^{(i)} \ldots f_{n_s}^{(i)}]^{\mathrm{T}}$. For the BVP, $\mathbf{F}^{(i)} = [\bar{f}_1 \, 0 \ldots 0]^{\mathrm{T}} \sin(\omega^* i \Delta t)$; for the IBVP, $f_1^{(i)}$ is obtained from the flow solution and all other terms in the $\mathbf{F}^{(i)}$ vector are set to zero.

Due to the incorporation of damping, $\mathbf{T}$ is generally not a diagonal matrix and thus obtaining $\mathbf{T}^{-1}$ is computationally expensive and introduces numerical errors, especially for large size matrices. However, utilizing the property that $\mathbf{T}$ is a tridiagonal matrix, the compact-storage Thomas algorithm is utilized – this is an efficient form of Gaussian elimination suited for tridiagonal systems. Finally, Eq. 5.3 is used to obtain the updated velocity. This process is repeated, allowing the simulation to march forward in time until it reaches t_{T}.

5.3.2   Fluid domain

Direct numerical simulations (DNS) have been executed to model the fluid domain and to examine the behavior of the proposed concept and its performance in altering the flow response. The initial flow excitation wave has been incorporated as a spatially evolving disturbance in a fully-developed plane Poiseuille (channel) flow driven by a mean pressure gradient. The channel is

formed by parallel walls at the bottom and at the top with periodic boundary conditions applied in the spanwise z-direction, and a buffer (sponge) layer is used to model the outflow. The base flow is an exact solution of the Navier-Stokes equation. Unstable spatial solution (eigenfunction) of the Orr-Sommerfeld equation is superimposed at the inflow boundary of the channel to perturb the parabolic base velocity, precisely modeling the conditions in typical laboratory experiments. Water is considered as the working fluid, a Reynolds number Re = 7500, and a range of non-dimensional unstable frequencies ω_R for each case study.

This work considers the time-dependent, three dimensional, incompressible continuity and the Navier-Stokes equation nondimensionalized by the channel half-height δ and the centerline velocity U_c. These equations read,

$$\frac{\partial u_i}{\partial x_i} = 0 \tag{5.5}$$

$$\frac{\partial u_i}{\partial t} + \frac{\partial u_j u_i}{\partial x_j} = \frac{2}{Re} - \frac{\partial p}{\partial x_i} + \frac{1}{Re}\frac{\partial u_i}{\partial x_j x_j} \tag{5.6}$$

Here, $Re = U_c \delta / \nu$, ν is the kinematic viscosity, and the vector $\mathbf{u} = \langle u, v, w \rangle$ represents the velocity components in the streamwise (x), wall-normal (y), and the spanwise (z) directions, respectively; also, p is the nondimensional pressure and t is nondimensional time. In Eqs. 5.5 and 5.6, the velocity vector can be decomposed into a base $\mathbf{u_b}$ and a fluctuating component $\hat{\mathbf{u}}$ such that

$$\mathbf{u} = \mathbf{u_b} + \hat{\mathbf{u}} \tag{5.7}$$

Using this decomposition, the initial/boundary conditions can be written as

$$\mathbf{u_b}(x = 0, 0 \leq y \leq 2, z, t) = \langle 1 - (1-y)^2, 0, 0 \rangle \tag{5.8}$$

$$\hat{\mathbf{u}}(x = 0, y, z, t) = A_{2D} Real[\mathbf{u}_{e2D}(y)e^{-i\omega_r t}] \tag{5.9}$$

$$\mathbf{u}(x, y = 0, 2, z, t) = 0 \tag{5.10}$$

where periodic boundary conditions are applied in the spanwise (z) direction. Equation 5.8 is the exact solution of the governing equations for laminar Poiseuille flow, where the dimensional channel height spans from $0 \rightarrow 2\delta$. For the spatially-evolving channel flow under consideration, the

outflow boundary conditions are imposed in the nonreflective buffer domain [111, 112, 108] where streamwise perturbations in the governing equations are smoothly brought to zero to ensure strictly outgoing waves.

In Equation 5.9, A_{2D} is the amplitude of the two-dimensional disturbance, $i = \sqrt{-1}$, ω_r is the real frequency and $\mathbf{u}_{e2D}$ is an eigenfunction obtained from the solution of the Orr-Sommerfeld equation, given as

$$(u_b - c)(\hat{v}'' - \alpha^2 \hat{v}) - u_b'' \hat{v} + \frac{i}{\alpha Re}(\hat{v}'''' - 2\alpha^2 \hat{v}'' + \alpha^4 \hat{v}) = 0 \tag{5.11}$$

where $()'$ represents differentiation in the wall-normal direction. In addition, the complex wave-speed, $c = -\omega_R/\alpha$ and $\alpha = \alpha_R + i\alpha_i$ represents the complex wavenumber.

Equation 5.11 constitutes an eigenvalue problem and is obtained from the linearized Navier-Stokes equation with the assumption of small disturbances. For spatially evolving channel flow, given real circular frequency ω_r and Re, Eq. 5.11 is solved for the complex eigenvalue α [113] where $-\alpha_i$ is the amplification rate of the corresponding eigenfunctions, u and v (Eq 5.9) which, in turn, are imposed as initial disturbances at the inflow boundary in the present simulations. Accordingly, disturbances will be unstable (growing in space) if $-\alpha_i > 0$.

A time-splitting procedure [111, 112, 108] is implemented to numerically integrate the governing equations where the Crank-Nicolson implicit method is used for the wall-normal direction diffusion term; all the other terms are treated explicitly with the Adams-Bashforth method. Spatial discretization is done by fourth-order central differences on a rectangular mesh system staggered and stretched along the wall-normal direction to accurately capture the fast flow field gradients. The time-splitting procedure first advances the velocity field, lagging the pressure gradient term. The corrector step then computes the pressure field satisfying continuity at the advanced time level. Using this method, excellent agreement with the linear theory is obtained, with a maximum deviation of 0.05% in the predicted perturbation energy growth [108].

In the coupled simulations, the structure extends in the spanwise, z, direction across the whole length of the computational domain without any spanwise variations, thus maintaining the

periodicity of the boundary conditions in that direction. At every time step, the dimensional wall pressure $p_{\text{w}} = p\rho_{\text{f}}U_{\text{c}}^2$ (where ρ_{f} is the fluid density) is calculated on the midpoint along the slot length on the fluid-structure interface. This pressure acts on the structure as a force and the resultant displacement, $\eta(0,t)$, and velocity, $\dot{\eta}(0,t)$, obtained from the integration of the solid domain model are imposed as flow field boundary conditions at the interface such that

$$\hat{u}(x_{\text{s}} \leq x \leq x_{\text{e}}, y = 0, z, t) = -\eta(0,t)\frac{du_{\text{b}}}{dy}, \tag{5.12a}$$

$$\hat{v}(x_{\text{s}} \leq x \leq x_{\text{e}}, y = 0, z, t) = \dot{\eta}(0,t). \tag{5.12b}$$

These boundary conditions are obtained assuming small displacements and allowing wall motion only along the wall-normal y-direction. Hence, it is critical that $\eta << \delta$ must be maintained throughout the computations. Additionally, the spanwise velocity, w, is zero at the fluid-structure interface.

5.4   Case study 1: single frequency two-dimensional disturbance control

In this case study, a two-layer unit-cell phononic crystal is used to reduce the amplitude of the primary mode in a channel undergoing transition when a single unstable TS wave is introduced. The entire structure is composed of 10 unit cells. For the results that follow, the physical domain lengths in the fluid are $L_x = 12\delta$, $L_y = 2\delta$, $L_z = 2\pi\delta$. The buffer domain extends from $12 \leq x \leq 20$ and encompasses 30% of the total channel length. The resolution for the rigid wall and control cases is $225 \times 8 \times 65$ in the streamwise (x), spanwise (z), and wall-normal (y) directions, respectively. The location of the phononic subsurface spans from $x_s = 6.96\delta$ to $x_e = 8.57\delta$ on the lower wall at $y = 0$. Outside of these bounds, the wall is assumed rigid and the boundary conditions on the wall then are no-slip.

The phase relation at a given excitation frequency ω^* between the force acting on the PnC subsurface, $\mathbf{f}$, and the displacement of the boundary between the solid and the fluid domains, $\mathbf{d}$, is used as an indicator of the degree of destruction (or construction) interference in the flow. The
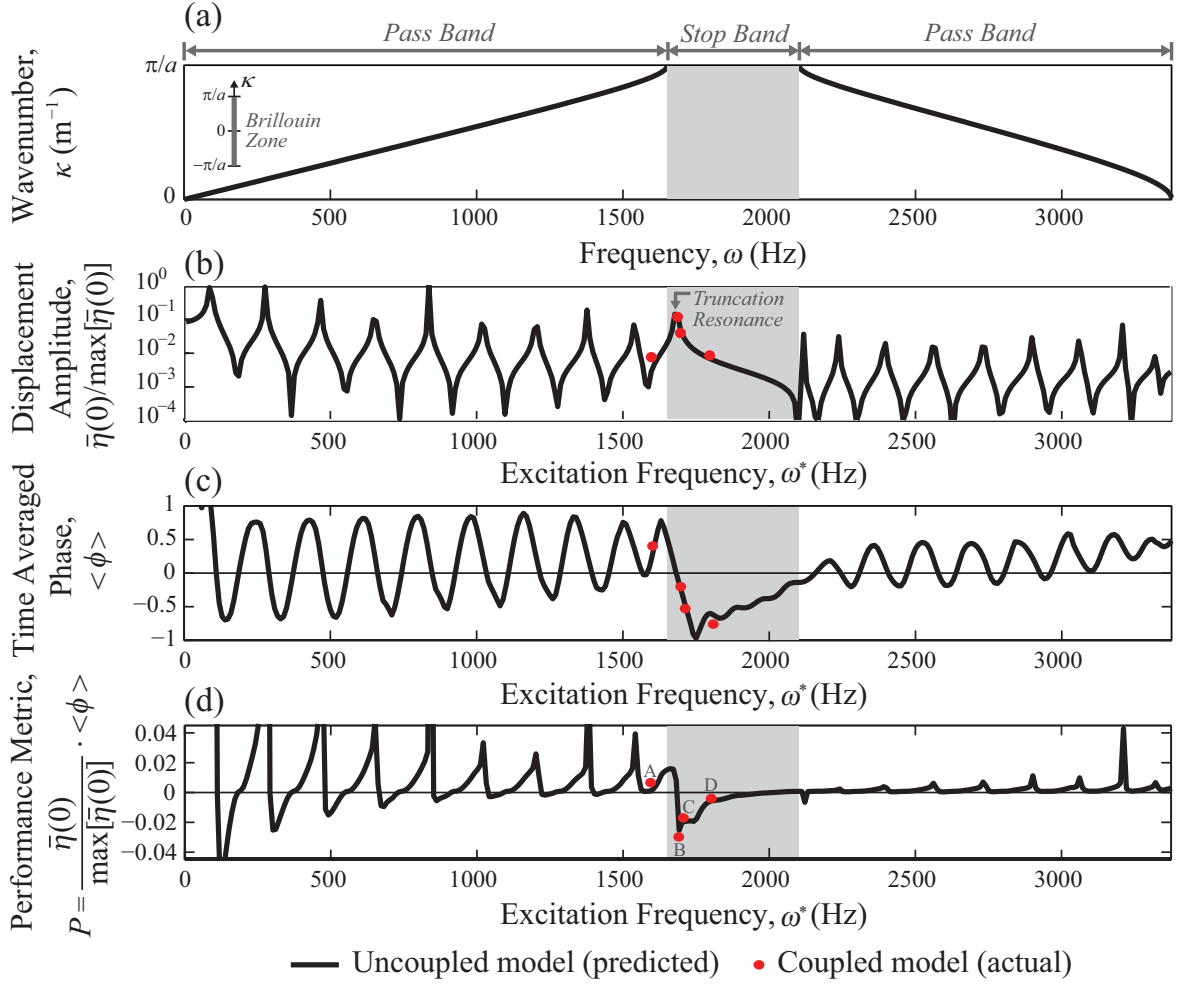
Figure 5.2: (a) Dispersion curves for the 1D phononic crystal from which the subsurface is composed. (b) Steady-state vibration response of phononic crystal top surface. (c) Time-averaged phase between force and displacement at the phononic crystal top surface. (d) Performance metric combining amplitude and relative phase between the force and the displacement at the phononic crystal top surface. Results from the coupled fluid-structure simulations are represented by red dots. In the coupled simulations, the phononic crystal top surface serves as the fluid-structure interface.

phase indicator is defined as the mean of the dot product between the two signals:

$$\phi(\omega^*) = \sum_{i=1}^{i=n} (\mathbf{f}_i(\omega^*)).(\mathbf{d}_i(\omega)^*)/n \tag{5.13}$$

where f_i is the force vector at time i, d_i is the displacement vector at time i, and n is the total number of time steps in the simulation time interval $\tilde{t} = [0, t_{\mathrm{T}}]$. The scalar value ϕ at a prescribed frequency, ω^*, is independent of t_{T} if n has a large enough value (i.e., the simulation time is long

enough to show the pass/stop band effect on the fluid field).

A performance metric, defined as $P = \langle \phi \rangle \cdot \bar{\eta}(0)/\max{[\bar{\eta}(0)]}$ is established, that incorporates both the phase and the intensity of the interface motion. Merging the isolated structure results given in Figs. 5.2(b) and 5.2(c), a prediction of the performance metric is obtained, namely, $P = P_{\mathrm{P}}$, which is plotted as a function of ω^* in Fig. 5.2(d). It is noticeable that the value of P is most negative at the truncation resonance frequency and retains its strong negative value over a substantial frequency range on the right side of $\omega_{\mathrm{Truncation}}$. The left side, to the contrary, experiences immediate positive P values that rise sharply and subsequently oscillate as the frequency decreases. While truncation modes are usually undesirable in conventional phononic crystals applications, here they provide a favorable effect. If the interest is to have a large frequency range for stabilization, then the unit cell should be designed to (1) exhibit the largest stop band possible encompassing the TS waves frequency range, and (2) have a truncation resonance located to the left of the TS waves frequency range and hence furthest to the left within the stop band to cover as wide a range as possible. If the interest is in destablization, then the unit cell should be designed to exhibit the highest possible value of $P-$in the positive domain$-$at or near the TS wave frequency (or frequency range).

Figure 5.2 shows the dispersion curves (a), the frequency response function (FRF) of the tip displacement (b), the phase between the forcing and tip displacement (c), and the time-averaged multiplication of the FRF normalized values with the phase values for the phononic crystal (d) (length = 0.4m, 90% ABS and 10% Al) – this provides a performance metric for the overall fluid-structure configuration. The black lines are obtained from uncoupled solid models, while the red dots represented the data acquired from coupled fluid-structure simulations at different frequencies (3 within a stop band 1690Hz, 1700Hz and 1800Hz and 1 in a pass band 1600Hz). Figure 5.2 demonstrates an excellent agreement between the coupled vs. the uncoupled models.

In Fig. 5.3, we show average quantities of the total energy, defined as:

$$\Psi(\omega^*; s, t) = \frac{1}{2} \left(E(\frac{d\eta}{ds})^2 + \rho_s \dot{\eta}^2 \right)$$

in the phononic subsurface from the coupled simulations. Figures 5.3a and 5.3b present a space-
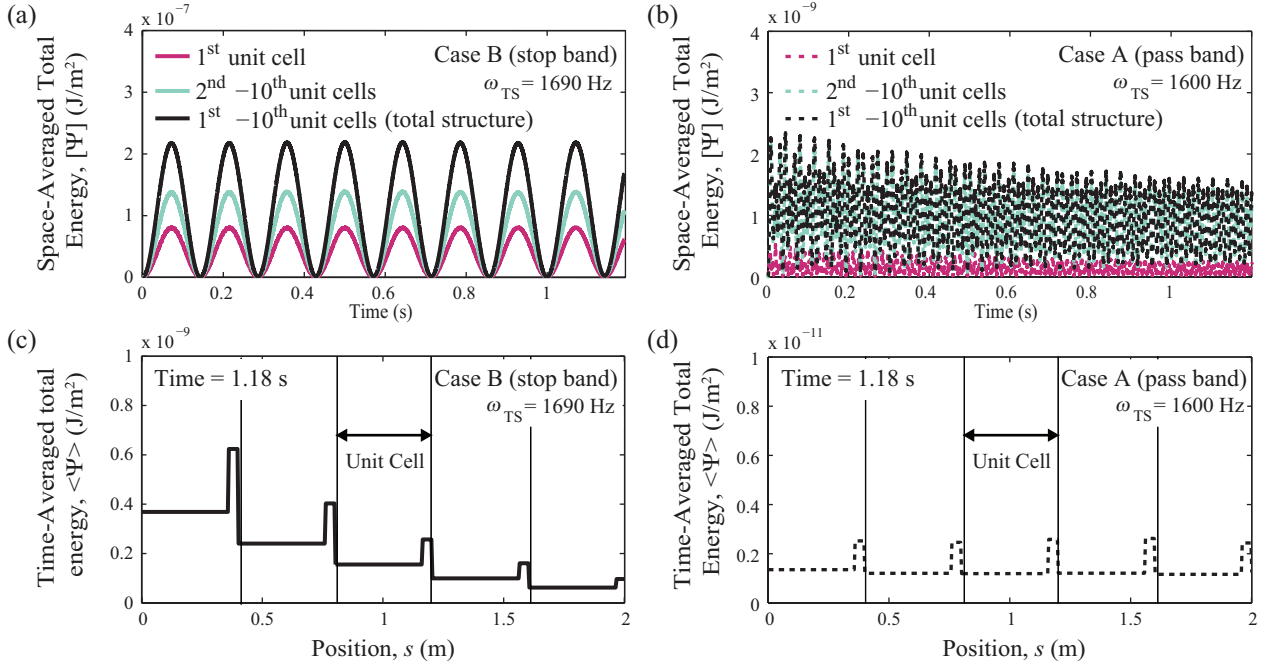
Figure 5.3: Average quantities of the total energy in the phononic subsurface for Case B ($\omega_{TS} = 1690$ Hz in a stop band) and Case A ($\omega_{TS} = 1600$ Hz in a pass band). The space-averaged total energy, defined as $\{\Psi(\omega^*, t)\} = \int_{s=0}^{s=l} [\Psi(\omega^*, t)] \, ds \approx \sum_{j=1}^{j=n_s} \Psi_j^{(i)}$, is shown in (a) for Case B and in (b) for Case A. The time-averaged total energy, defined as $\langle \Psi(\omega^*, t) \rangle = \int_{t=0}^{t=t_T} [\Psi(\omega^*, t)] \, dt \approx \sum_{i=1}^{i=n} \Psi_j^{(i)}$, is shown in (c) for Case B and in (d) for Case A. The unit cells are marked by vertical lines.

averaged total (kinetic and potential) energy for Case B (stop band) and Case A (pass band), respectively, displaying oscillating patterns and a two-orders of magnitude larger overall response for Case B as anticipated. Also noticeable is that in both cases the motion of the phononic subsurface, including the top end which interfaces with the flow, is stable−i.e., there is no occurrence of flutter. Figures 5.3c and 5.3d present a time-averaged total (kinetic and potential) energy for Case B and Case A, respectively, for the top half of the structure and over the full simulation time. The energy profile for Cases B and A are attenuating and non-attenuating, respectively, which is perfectly consistent with the stop-band/pass-band behavior, as predicted.

For the fluid analysis two quantities are plotted, the space-averaged time-dependent perturbation kinetic energy, T_f^* [in units of J (Joules)] and the time-averaged position-dependent perturbation kinetic energy, K_f^* [in units of J/m (Joules per meter)]. The former quantity, which

is based on a volume-integration, is given by:

$$T_{\mathrm{f}}^{*}(t^{*}) = \rho_{\mathrm{f}} \int_{0}^{L_z} \int_{0}^{\delta} \int_{0}^{L_x} \frac{1}{2} \left(\hat{u}^{*2} + \hat{v}^{*2} + \hat{w}^{*2} \right) dx^{*} dy^{*} dz^{*}, \tag{5.14}$$

where the vector $\mathbf{u} = (u, v, w)$ represents the velocity components in the streamwise, x, wall-normal, y, and the spanwise, z, directions, respectively, ρ_{f} is the fluid density, L_x and L_y are the channel-base dimensions, and δ is the channel half-height. The symbols $\hat{()}$ and $()^{*}$ are used to represent a fluctuating component of the velocity field and a dimensional quantity, respectively (see Appendix A for the detailed velocity decomposition formulation). The term $T_{\mathrm{f}}^{*}(t^{*})$ directly quantifies the instability wave kinetic energy in the bottom half of the channel as a function of dimensional time t^{*} (an asterisk is added here for convenience). The volume of integration over the bottom half of the channel is bounded by its physical domain, that is, the buffer domain is excluded from the integration. The K_{f}^{*}, on the other hand, is based on a time-area integration and is a function of the dimensional streamwise coordinate x^{*}. It is defined as:

$$K_{\mathrm{f}}^{*}(x^{*}) = \frac{\rho_{\mathrm{f}}}{(t_{\mathrm{end}}^{*} - t_{\mathrm{beg}}^{*})} \int_{t_{\mathrm{beg}}^{*}}^{t_{\mathrm{end}}^{*}} \int_{0}^{L_z} \int_{0}^{\delta} \frac{1}{2} \left(\hat{u}^{*2} + \hat{v}^{*2} + \hat{w}^{*2} \right) dy^{*} dz^{*} dt^{*}, \tag{5.15}$$

where t_{beg}^{*} denotes the beginning of the time-averaging window and t_{end}^{*} denotes the end of the time-averaging window. In the calculations, $t_{\mathrm{beg}}^{*} = 0.03$s and $t_{\mathrm{end}}^{*} = 1.17$s which represents a relatively long integration time (corresponding to approximately 1500 Tollmien-Schlichting-wave periods).

The T_{f}^{*} quantity is plotted in Figs. 5.4a and 5.4b. In the stop-band frequency case (Fig. 5.4a), the perturbation kinetic energy, while oscillating, is predominantly lower in value when a phononic subsurface is installed compared to all-rigid walls. In contrast, the two extreme arrangements of an all-ABS and all-aluminum subsurface display negligible effect. Fig. 5.4b show the corresponding results for the pass-band frequency case where we observe a predominantly positive increase in the perturbation kinetic energy (due to a positive P) and generally a significantly smaller effect overall (due to a low $|P|$). Also of significance is that neither the stop-band or the pass-band responses
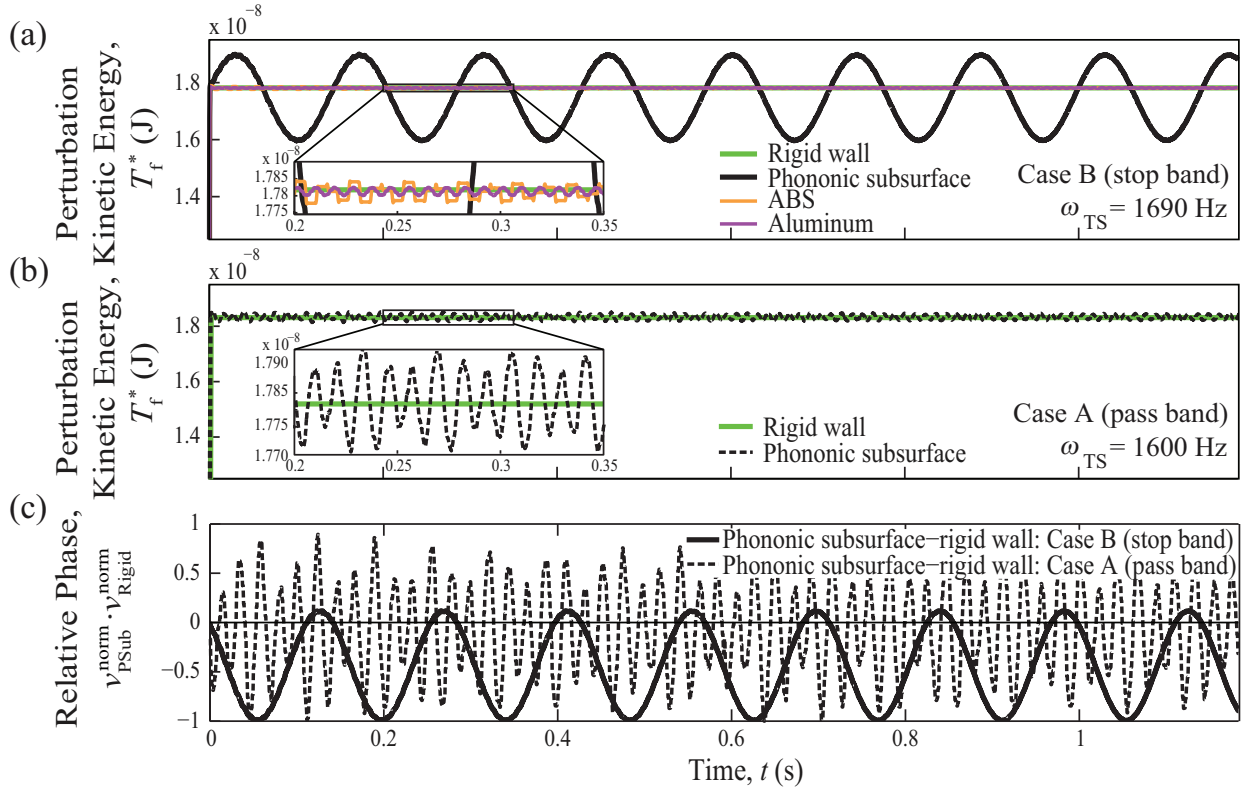
Figure 5.4: Time history of the kinetic energy of the disturbance field within the bottom half of the channel for (a) Case B (ω_{TS} = 1690 Hz in a stop band) and (b) Case A (ω_{TS} = 1600 Hz in a pass band). (c) Relative phase between flow vertical velocity when a phononic subsurface is installed compared to all-rigid walls (Rigid). Each velocity quantity is normalized with respect to its maximum value.

are decaying in time, thus the control mechanism takes effect in a steady-state and sustainable fashion. To explicitly examine the role of phase in the phenomenon observed, Fig. 5.4c monitors the relative phase between the flow vertical velocity right above the control segment at $y = 0.0108\delta$ when a phononic subsurface is installed compared to all-rigid walls. It can be see that in the stop-band case, the introduction of the phononic subsurface alters the phase significantly compared to the pass-band case where the phase is preserved on average. This result confirms the existence of destructive interferences in the vertical velocity components of the flow near the interface for Case B, and conversely, the existence of constructive interferences for Case A. [2] Hence the influence of

---

[2] The wave interferences subsequently also affect the horizontal components of the flow due to the inherent coupling between the components.

the band structure of the phononic subsurface is shown to have extended to the flow.
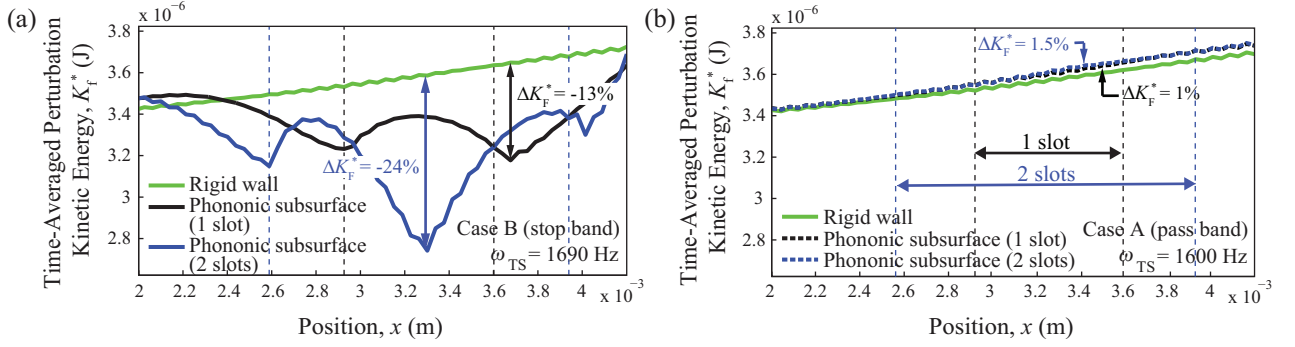
Figure 5.5: Streamwise spatial distribution of the kinetic energy of the disturbance field within the bottom half of the channel for (a) Case B ($\omega_{TS} = 1690$ Hz in a stop band) and (b) Case A ($\omega_{TS} = 1600$ Hz in a pass band). The plotted quantity represents the spatial intensity of the flow instability.

The time-averaged disturbance kinetic energy (KE) for (a) case B (stop band) and (b) case A (pass band) is presented in Fig. 5.5. The green line is the base case for an all-rigid bottom of the channel. The vertical dashed lines represent the position of the phononic subsurface with respect to the channel. The black and blue lines show the KE of the unstable frequencies incorporating a phononic subsurface. In the stop band case, a strong desired reduction is achieved as predicted. The phononic subsurface single slot stimulated a 13% reduction in perturbation ke and 24% is recorded by using two slots. In the pass band case, the expected destabilization is also shown to occur for both one and two slots.

5.4.1 Design search space

Case study 1 shows the ability of the phononic subsurface to effectively control a two-dimensional disturbance occurring at the most critical (i.e., least stable) frequency in the flow field. In principal this could be achieved either in a pass or stop band. The key is to position the targeted frequency to the left of the resonance frequency, when destabilization is desired or to the right of the resonance, if stabilization is the objective. Although the concept works for the entire frequency spectrum, resonance frequencies are sensitive to boundary conditions and fabrication

imperfections in pass bands. Therefore stop bands represent a robust and unique design target, as they emerge at the unit cell level.

Figure 5.6 presents the evolution of the 1st band gap in a two-layer unit cell design as the relative width of the plastic layer varies. The percentage of the band gap relative width is defined as:

$$BG \% = \frac{1}{2} * \frac{max(\omega_{UE} - \omega_{LE}, 0)}{(\omega_{UE} + \omega_{LE})/2}, \tag{5.16}$$

where ω_{UE} and ω_{LE} denotes the frequencies of the upper and the lower edge of the band gap, respectively. The band gap exists only when the ω_{UE} is greater than ω_{LE}; otherwise no band gap exists. The relative BG equation is multiplied by $1/2$ to ensure that the percentage lies between 0 and 1. The plot also shows the stabilization and the destabilization regions within the band gap calculated by:

$$BG_{stab} \% = \frac{1}{2} * \frac{max(\omega_{UE} - \omega_{Trunc}, 0)}{(\omega_{UE} + \omega_{Trunc})/2}, \tag{5.17}$$

$$BG_{destab} \% = \frac{1}{2} * \frac{max(\omega_{Trunc} - \omega_{LE}, 0)}{(\omega_{Trunc} + \omega_{LE})/2}, \tag{5.18}$$

Since case study 1 considers controlling one unstable frequency at a time, any design with $(BG_{stab}$ and/or $BG_{dest}) > 0$ should perform the desired function.

5.5   Case study 2: multiple-frequency two-dimensional disturbance control

The study described above is concerned with the control of a single unstable TS wave intentionally introduced to the flow field. However, in a more natural transition environment, a continuous range of unstable frequencies may be present in the flow field. In this case, it would be desirable to affect a desired range of frequencies that may be present in the flow for a given Reynolds number. That is, knowing the (approximate) Reynolds number of the flow, is it possible to design a phononic subsurface that can reduce the amplitude of a continuous range of unstable modes, without introducing other undesirable modes into the flow field. Here, the ability of using properly designed phononic subsurfaces to reduce the amplitude of a number of unstable modes artificially introduced in the flow field is demonstrated.
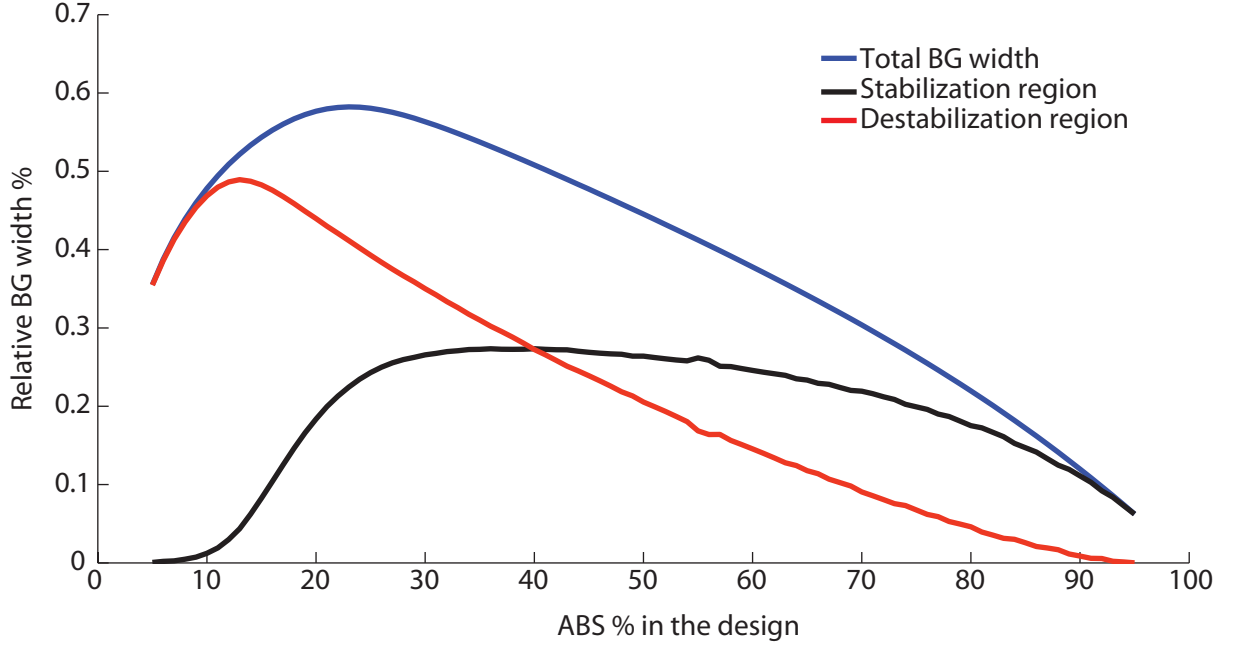
Figure 5.6: Design space for 1D phononic crystal composed of two layers. The y-axis shows the percentage of the band gap as the first layer of ABS plastic width vary within the unit cell.

The disturbances are introduced at the inflow using a linear superposition of modes that span the unstable range of frequencies for a fixed laminar Reynolds number. These disturbances are the eigenfunctions corresponding to the solution of the Orr-Sommerfeld equations, given previously in Eq. 5.9. This is illustrated in figure 5.7, where the span of unstable non-dimensional frequencies ranges between $0.205 < \omega_r < 0.285$ for a Reynolds number $Re = 7,500$. Note that the curve in figure 5.7 represents the neutral curve ($\alpha_i = 0$), where any frequency that lies inside the curve is unstable, and any frequency that lies outside the curve is stable. The unstable frequencies and their growth rates are summarized in table 5.1, and their location on the stability diagram is shown in figure 5.7.

ω^* [Hz]	ω_r	α_r	$-\alpha_i$
1487	0.22	0.9167	0.003733
1690	0.25	1.0003	0.006168
1893	0.28	1.0828	0.001307

Table 5.1: Selected unstable frequencies for $Re = 7,500$
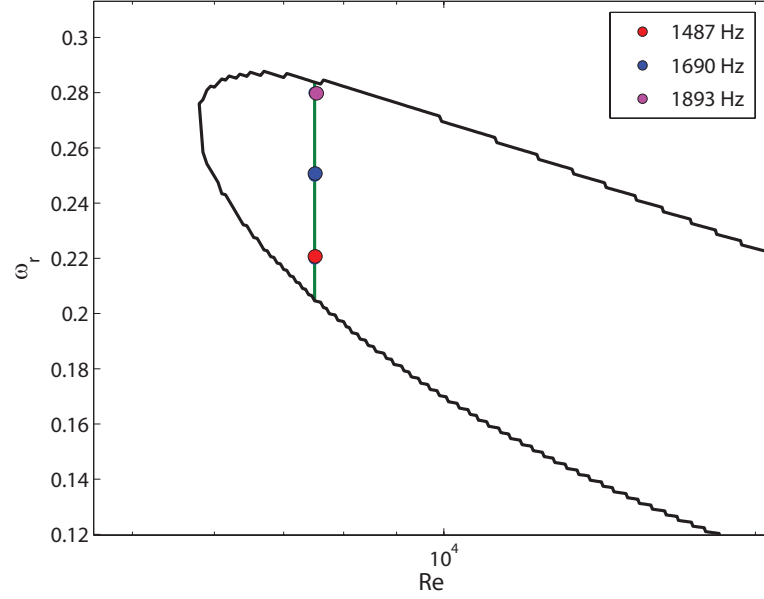
Figure 5.7: Neutral curve ($\alpha_i = 0$) for channel flow, selected frequencies corresponding to the dimensional excited frequencies in the coupled solid-fluid simulations.

In table 5.1, the dimensional frequency ω^* is obtained as

$$\omega^* = \frac{\omega_r}{2\pi} \frac{U_c}{\delta} \tag{5.19}$$

where either U_c or δ is prescribed for a given fluid viscosity ν and Re. For this particular simulation, $U_c = 17.8$ m/s, $\delta = 4.2 \times 10^{-4}$ m, and $\nu = 1 \times 10^{-6}$ m^2/s (water). These *dimensional* frequencies are used to design a phononic subsurface that mitigates a portion or all of the unstable frequencies in the flow field. Here, two different unit-cell designs are implemented. The band gap of the first design covers only half of the unstable frequency range, while the second design has a band gap that covers the entire unstable frequency range. The characteristics of theses two designs are shown in figures 5.2 and 5.9 respectively, with the range of unstable fluid frequencies superimposed on the frequency diagrams.

A summary of the two phononic subsurface designs is shown in table 5.2
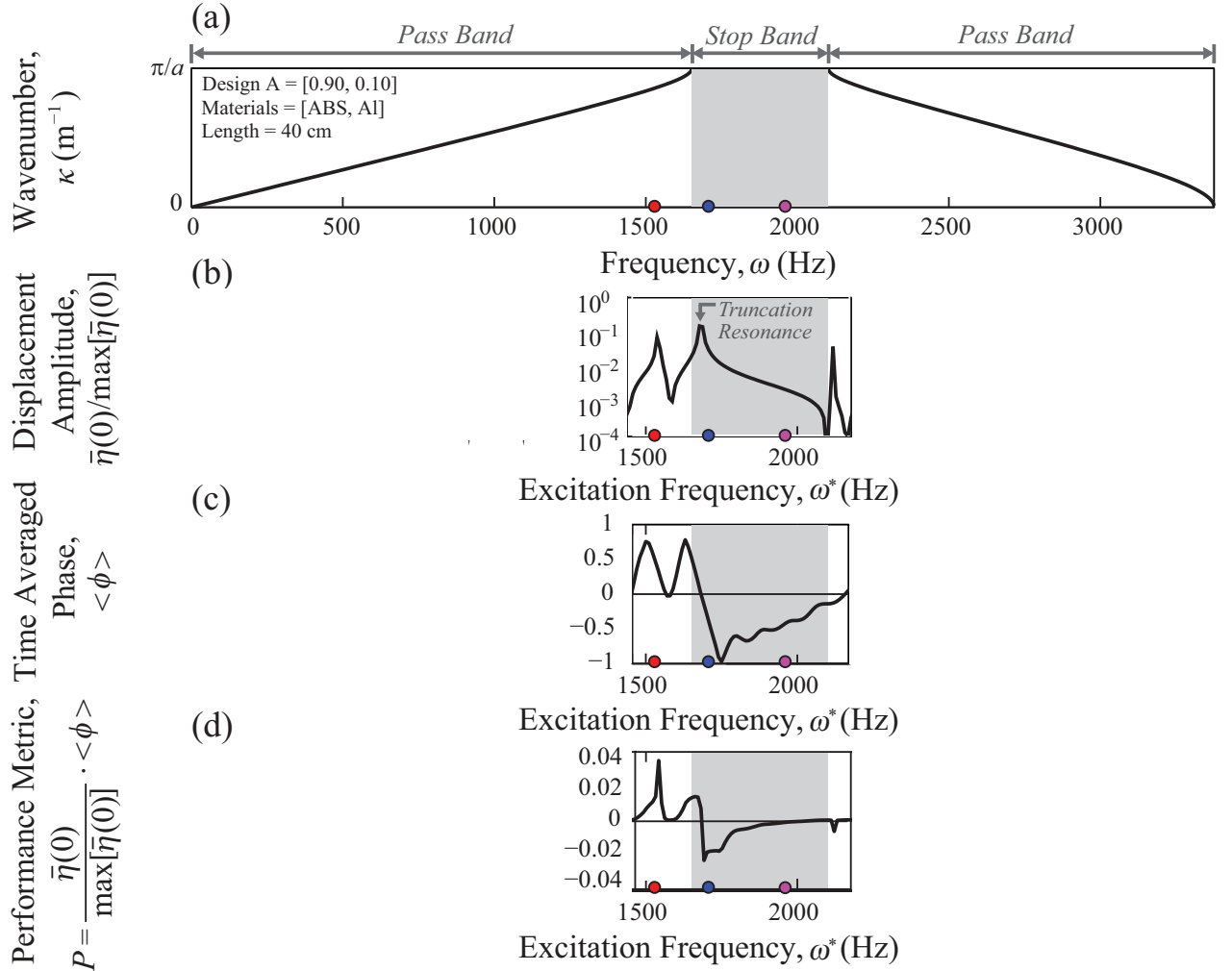
Figure 5.8: (a) Dispersion curves for the layered unit cell A composed of 2 layers (90% ABS and 10% Al). (b) Steady-state vibration response of design B. (c) Time-averaged phase between force and displacement at the phononic crystal top surface. (d) Performance metric combining amplitude and relative phase between the force and the displacement at the phononic crystal top surface. Excited frequencies in the coupled fluid-structure simulations are marked with dots. Structural analysis in (b),(c) and (d) is limited to the frequency range of interest

Design	Band Gap (Hz)	Unstable Fluid (Hz)	Truncation (Hz)
A	1652 → 2102	1383 → 1927	1684
B	1498 → 2493	1383 → 1927	1480

Table 5.2: Summary of the phononic subsurface designs
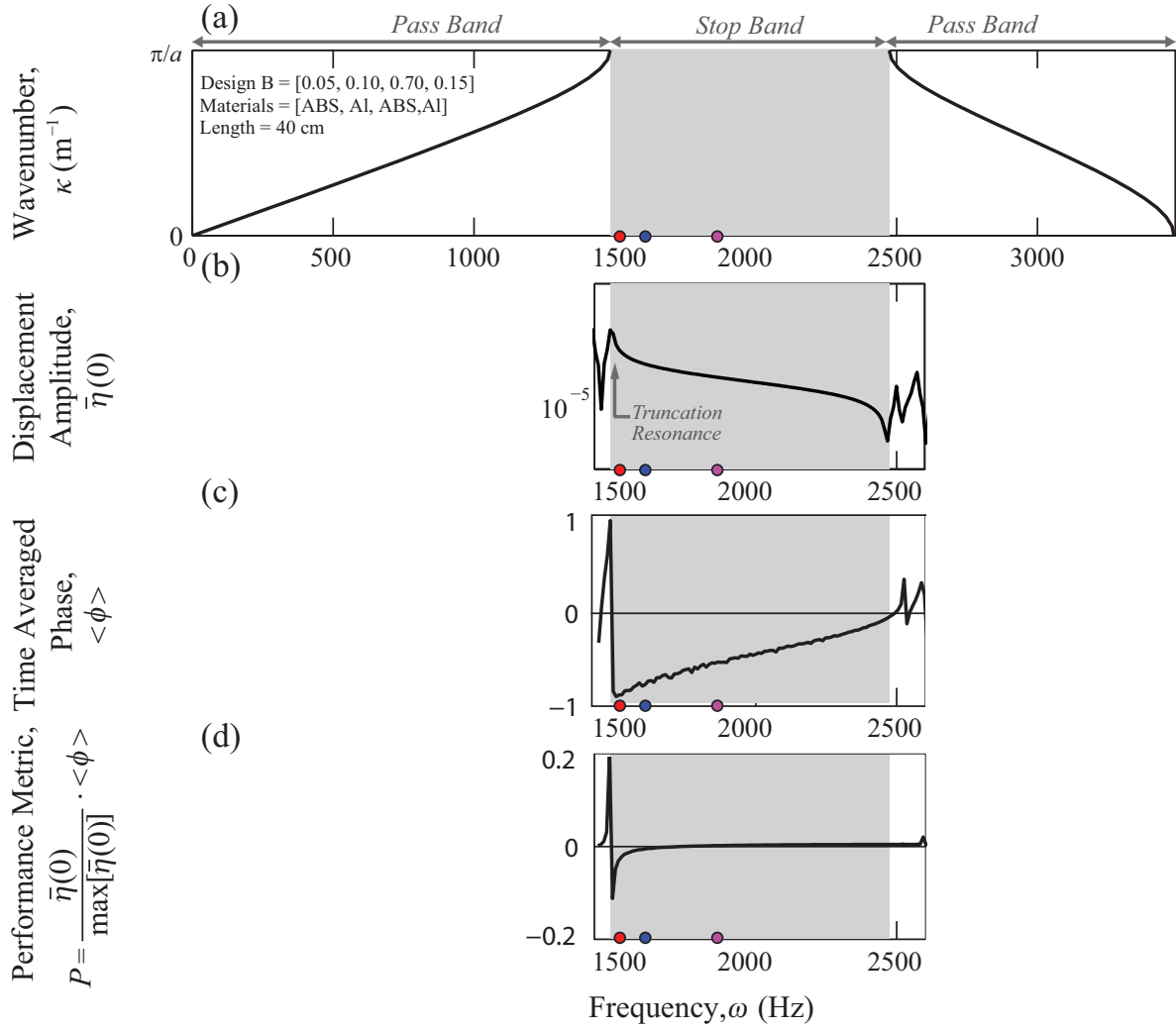
Figure 5.9: (a) Dispersion curves for the layered unit cell B composed of 4 layers with widths included in the inset. (b) Steady-state vibration response of design B. (c) Time-averaged phase between force and displacement at the phononic crystal top surface. (d) Performance metric combining amplitude and relative phase between the force and the displacement at the phononic crystal top surface. Excited frequencies in the coupled fluid-structure simulations are marked with dots. Structural analysis in (b),(c) and (d) is limited to the frequency range of interest

Figure 5.10 shows the perpetration KE in the flow for each of the excited frequencies. The dashed lines represent the rigid wall solution, and the solid lines represent the solution where the phononic subsurface replaces part of the rigid wall. The vertical dashed lines indicate the boundaries of the phononic subsurface. It is expected from figure 5.2(d) that any disturbance with a frequency falling to the left of the truncation frequency (1487 Hz) should grow in amplitude and

that any disturbance frequency to the right of the truncation frequency (1690 Hz and 1893 Hz) should decrease in amplitude as the disturbances pass over the phononic subsurface.

This prediction is in agreement with the results of the coupled simulations shown in figure 5.10(a), where both the 1690 Hz and 1892 Hz disturbance frequencies experience a decrease in amplitude and the 1487 Hz disturbance frequency experiences an increase in amplitude. As mentioned before, the strength of the effect is dictated by the placement of these frequencies relative to the truncation frequency (Fig. 5.2(d)), where the modes closest to this frequency will experience the greatest attenuation when the performance metric P is at a minimum.

Spectra for phononic subsurface B is presented in figure 5.10(b). The spectra behaves similar to figure 5.10(a), where 1690 Hz and 1892 Hz experience attenuation. However, 1487 Hz also experiences attenuation due to the design of this particular subsurface, where the band gap spans the entire range of unstable frequencies present in the fluid. That is, all three modes interact independently and favorably with the structure such that the phase between force and displacement at the fluid/surface interface ensures the attenuation of these disturbance waves.

The last figure in this section shows the aggregate perturbation KE for the different designs tested. Figure 5.11 demonstrates the ability of the two designs arranged consecutively downstream of one another to induce higher maximum reduction in the total integrated kinetic energy $K_f(x)$.

5.5.1   Design search space

Case study 2 shows the ability of the phononic subsurface to effectively stabilize a number of two-dimensional disturbances occurring within a range of critical (i.e., unstable) frequencies in the flow field. In contrast to case study 1, designing the unit cell to incorporate the entire range within the stabilization band gap is not straightforward. Given the range of frequencies for this particular Reynolds number, the relative BG stabilization percentage should exceed 22% to encompass the entire critical spectrum. Design A (90% ABS, 10% Al) cannot effectively cover the entire range as it has $\approx 11\%$ effective stabilization BG. Although, numerous designs with 2 layers posses the BG width needed for the problem defined in case study 2, the relative width of the BG for stabilization
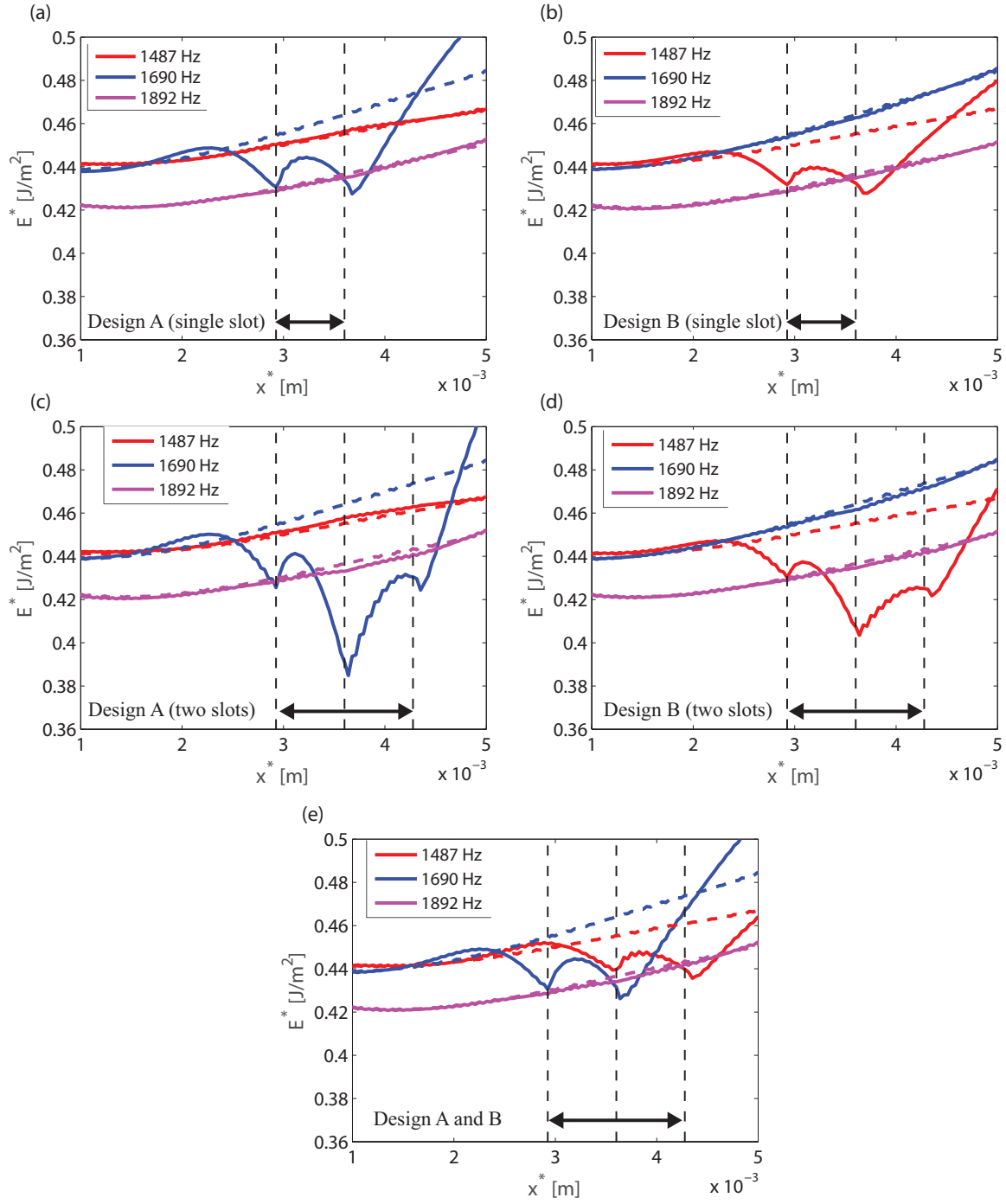
Figure 5.10: Streamwise modal spatial distribution of the kinetic energy of the disturbance field within the bottom half of the channel with different excitation frequencies for (a) Design A (single slot), (b) Design B (single slot), (c) Design A (two consecutive slots), (d) Design B (two consecutive slots) and (e) Design A&B (as two consecutive slots).
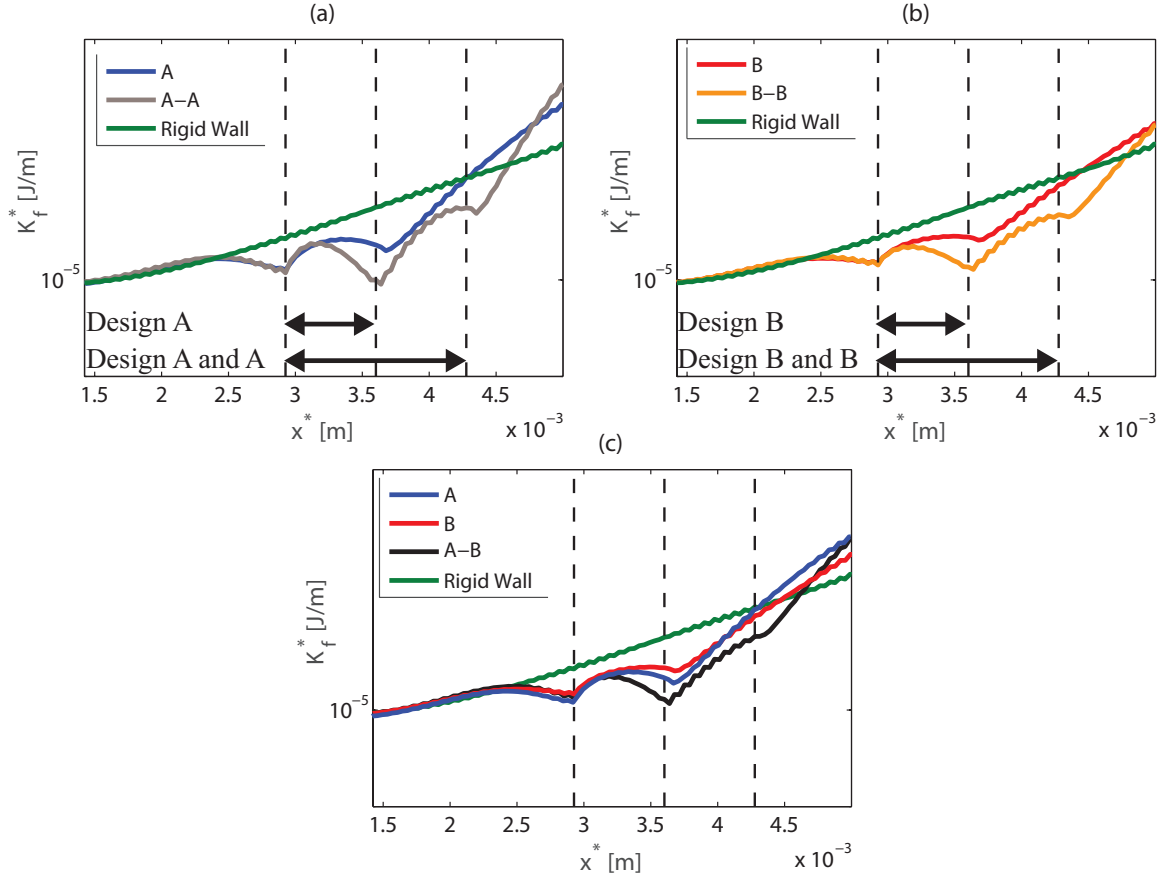
Figure 5.11: Streamwise total spatial distribution of the kinetic energy of the disturbance field within the bottom half of the channel with all excitation frequencies for (a) Design A (single and double contiguous slots), (b) Design B (single and double contiguous slot), (c) Single slots of design A, design B and A&B. The plotted quantity represents the spatial intensity of the flow instability. Green lines represent a rigid wall case. Vertically dashed lines indicate the upstream and downstream boundaries of the phononic subsurfaces.

is bounded by $\approx 30\%$. Therefore designs with more complex topologies (number of layers) are explored.

Figure 5.12 presents the evolution of the stabilization effective relative first band-gap in two and four-layer unit cell design as the percentage of the ABS plastic varying within the unit cell. For the four-layer designs, a minimum layer width is assumed (0.2%) with a discrete increment to each layer thickness. All the possible combinations that lead to a design with width = 1 are plotted in Fig. 5.12, with a few of them exceeding 50% effective operating frequency range.
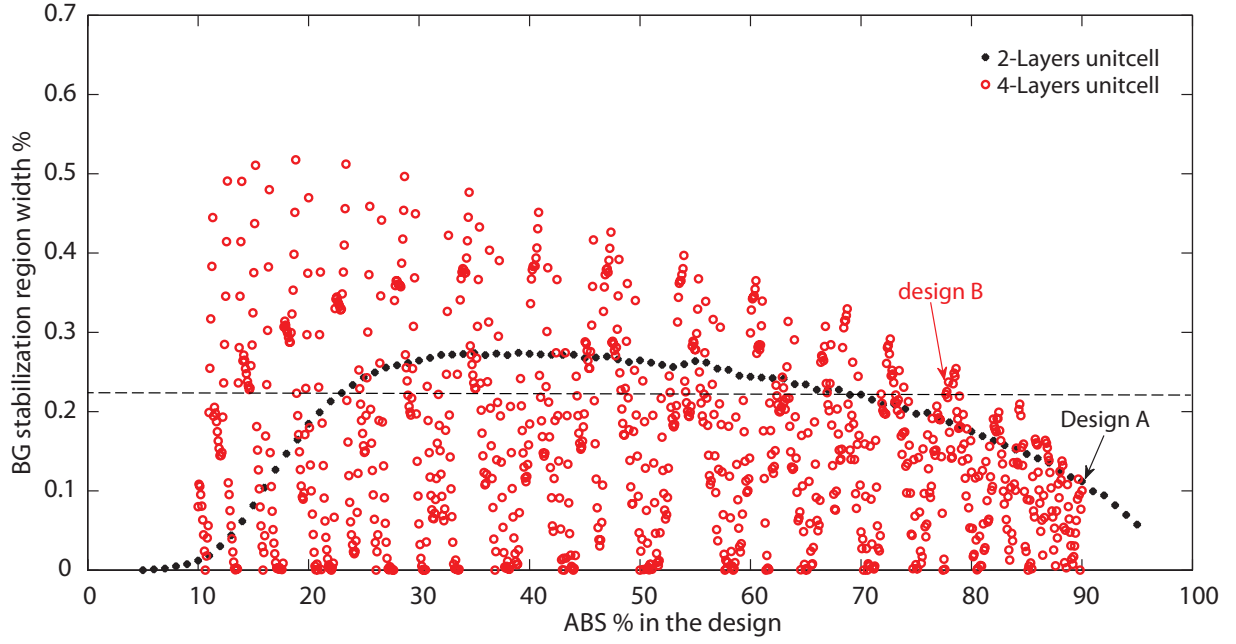
Figure 5.12: Design space for 1D phononic crystal composed of two layers (black) and four layers (red). The y-axis shows the percentage of stabilization effective band gap relative width as the percentage of ABS plastic content vary within the unit cell. The black dashed line represents the minimum relative width needed to cover the range of the unstable frequencies in the flow.

5.6   Case study 3: three-dimensional nonlinear disturbance control

In this section, the two-dimensional (primary mode) fluid instability problem is expanded to become susceptible to three-dimensional disturbances (secondary mode) at some finite amplitude [108]. The modes are defined as multiples of the real fundamental frequency ω_r and real spanwise wavenumber $\beta_r = 2\pi/L_z$ such that $\omega = n\omega_r$ and $\beta = m\beta_r$. This allows for defining modes as a pair (n, m) (e.g., a fundamental mode can be (1,m), its subharmonic is (0.5,m) and its superharmonic (2,m)). This means exciting the flow at a certain frequency ω^* and expecting a harmonic generation of $n\omega^*$ excitation as harmonics. Therefore, the phononic subsurface is designed to have two effective stabilization regions (i.e., falling within a band gap and to the right of the truncation resonance). Table 5.3 summarizes the range of the effective frequency ranges of the utilized design for this case study (design C). The layout of its unit cell is [0.48,0.02,0.42,0.08] with the first layer being ABS plastic.

Design	Band Gap (Hz)	Unstable Fluid (Hz)	Truncation (Hz)
C 1st BG	$1672 \rightarrow 1932$	1690	1684
C 2nd BG	$3236 \rightarrow 4052$	3380	3364

Table 5.3: Summary of the phononic subsurface design C

Figure 5.13.a presents the dispersion curves of design C with the band gaps highlighted in gray. The frequency response function for the structure composed of 10 unit cells is shown in Fig. 5.13.b. Two truncation resonances are present within the first and the second band gaps. In order to effectively control both the primary unstable frequency and its harmonic, both truncation resonances should be to the left of the critical frequencies, in the same time not too far away from it. This guaranties a negative value of the time averaged phase $< \Phi >$ at the critical frequencies Fig. 5.13.c. In addition, the value of the performance metric P is favorable (i.e., negative and is relatively large in the absolute sense) at both frequencies as reported in Fig. 5.13.d.

Similar to the previous case studied, the evolution of the perturbation KE over time is plotted in Figure 5.14. Since spanwise disturbances are allowed to vary in this model, the plotted quantity is integrated for each plane in the spanwise separately across the channel. For a clear comparison with the rigid wall case, the energy is subtracted from the base case of the rigid wall. The surface plot is mostly below zero, which translates to reduction in the total perturbation kinetic energy. Although the plotted energy fluctuates during the simulation time above the rigid wall values, the aggregate behavior is favorable. In other words it is inducing a stabilizing effect (i.e., mostly negative).

The streamwise evolution of selected modal contributions of perturbation kinetic energy (KE) is shown in Fig. 5.15(a). Compared to the reference all-rigid-wall case (dashed lines), it is observed that the perturbation KE decreases across the length of the phononic crystal interface for the primary mode (blue) However, this effect is reversed for the three other modes presented and may be explained by nonlinear interactions. This reversed effect is somewhat negligible, however, owing
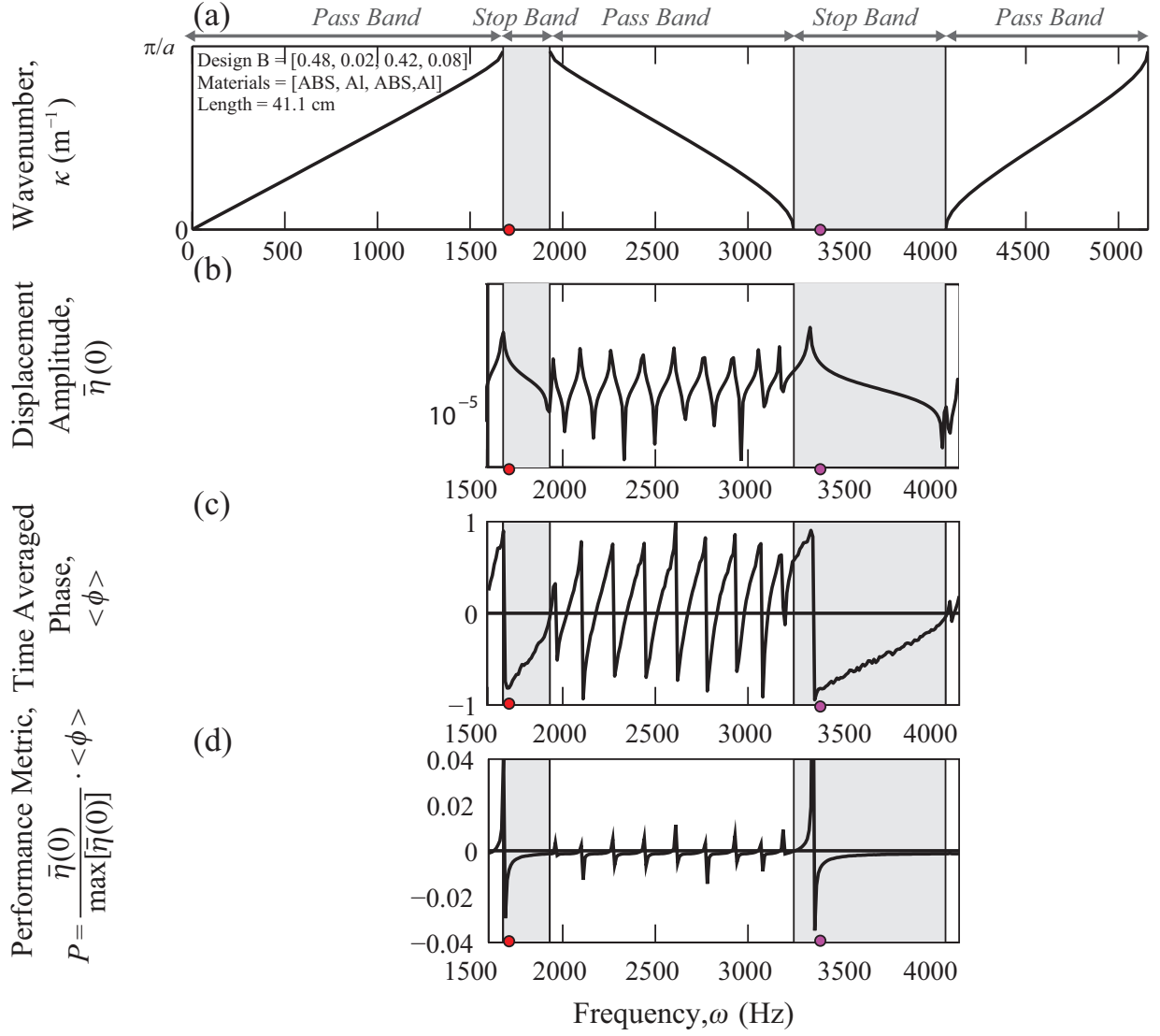
Figure 5.13: (a) Dispersion curves for the layered unit cell C composed of 4 layers with widths included in the inset. (b) Steady-state vibration response of design C. (c) Time-averaged phase between force and displacement at the phononic crystal top surface. (d) Performance metric combining amplitude and relative phase between the force and the displacement at the phononic crystal top surface. Red dots represent the excited frequency in the flow where purple ones represent its harmonic. Structural analysis in (b),(c) and (d) is limited to the frequency range of interest.

to the difference in the orders of magnitude of the modal energies. By stabilizing the primary mode only, a reduction of maximum 8% in the total perturbation kinetic energy (summed over all modes) is shown in Fig. 5.15(b). These results show the ability of the subsurface phononic crystal to stabilize the three-dimensional flow field via synchronized frequency-dependent wave interferences,
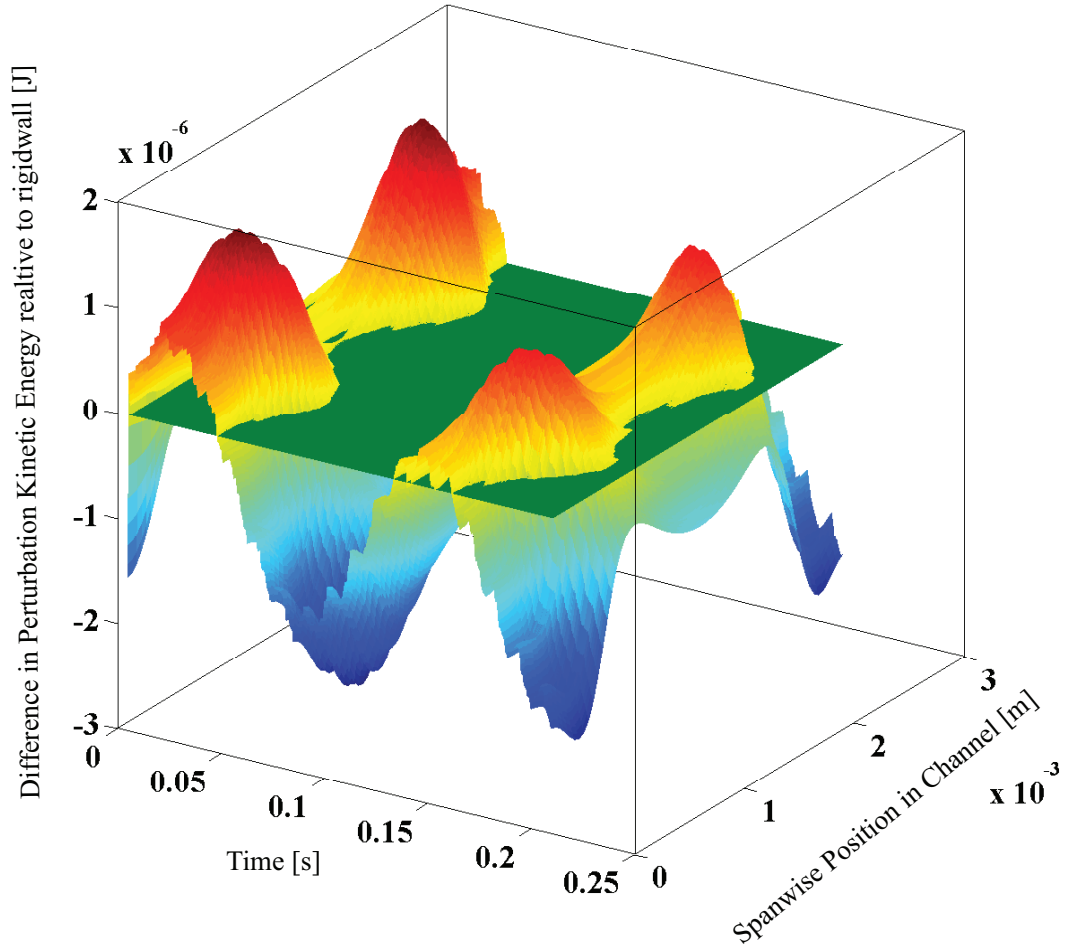
Figure 5.14: Difference in Kinetic energy as a surface plot for time history of the disturbance field within the bottom half of the channel when a phononic subsurface is installed.

even in the presence of nonlinearities.

5.6.1   Design search space

Case study 3 presents a challenge in the design process of the phononic subsurface unit-cell. In contrast to the previous case studies, the objective here is not limited to opening a band gap (from the dispersion curves) with a truncation resonance inside of it (from the frequency response function). The objective is not only to have two band gaps with two truncation resonances both
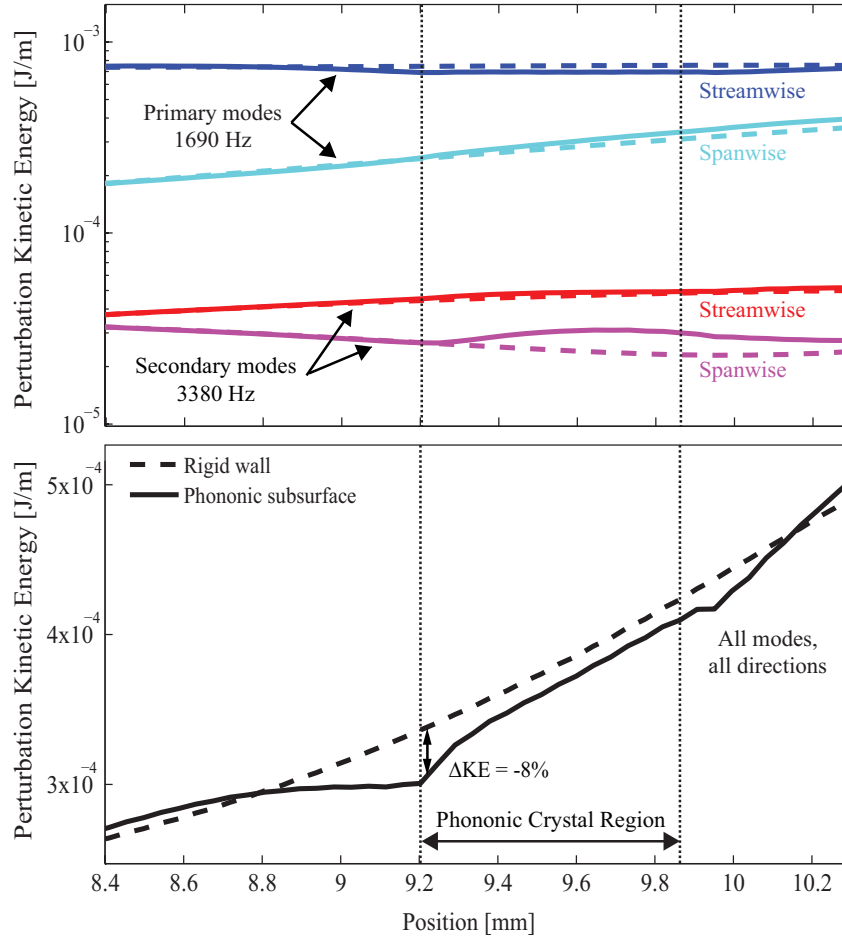
Figure 5.15: Streamwise spatial distributions of the kinetic energy of the disturbance field within the bottom half of the channel; the dotted lines represents the base model (i.e., with no control) and the continuous lines represent the model with the phononic crystal. The plotted quantity represents the spatial intensity of the flow instability.

falling to the right of the excitation frequency ω and its double 2ω but also to have the truncation resonances as close as possible to ω and 2ω. Figure 5.16.(top) shows the design search space for unit cells composed of 2 and 4 layers. The bottom part of the figure shows a zoom-in for the range where the designs can induce an effective control.

5.7   Conclusion

A direct numerical simulation of the fully time-dependent, three-dimensional Navier-Stokes equation in a spatially evolving plane-channel flow is performed to simulate the growth of instability
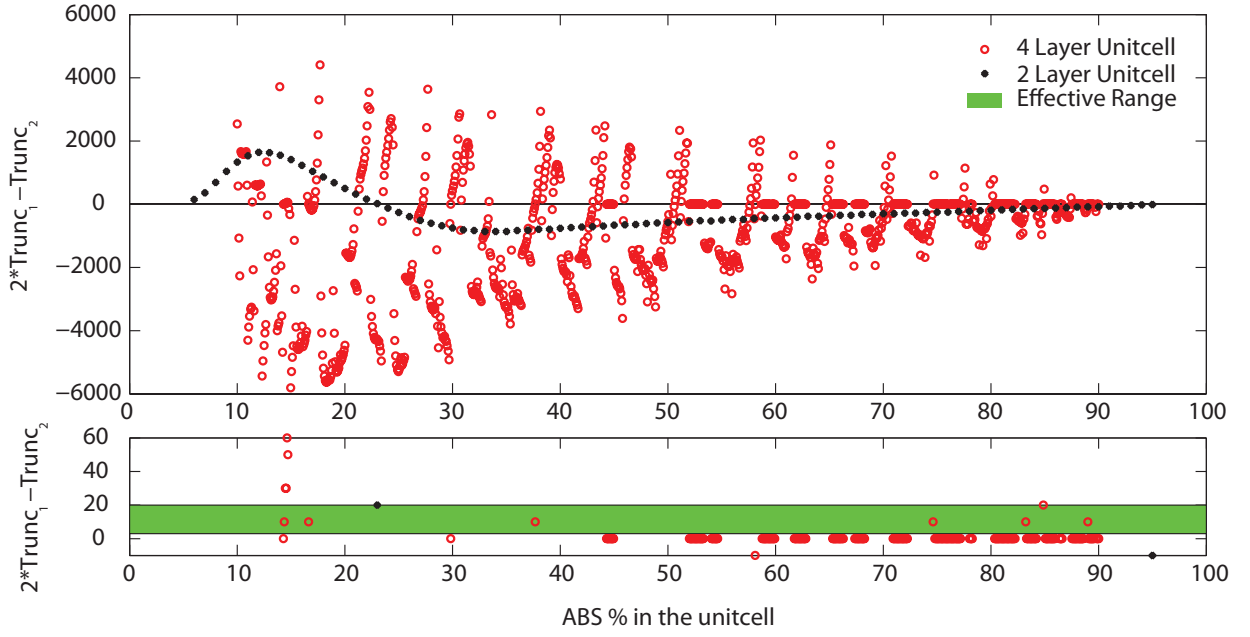
Figure 5.16: Design search space for 1D phononic crystal for stabilizing three-dimensional flow disturbances (top) and a zoom-in for the effective design range (bottom). $Trunc_n$ is the frequency of the truncation resonance in the nth band gap.

mechanisms. By replacing a part of the channel wall with a carefully designed phononic crystal, the kinetic energy of the unstable waves is shown to decrease. Computational experiments are carried out for three case (1) 2D single frequency disturbance (2) 2D multi-frequency disturbance (3) 3D nonlinear disturbance. These results open the way for the entry of phononics into the field of flow control.

Chapter 6

Conclusions and future work

6.1   Summary of dissertation

The contributions of this thesis are classified into three main subcategories; optimization of phononic crystals, design of elastic metamaterials and investigation of using phononic materials for flow control. Chapter 1 introduces the basic classification of phononic materials and highlights where the present work fits within the broader literature. Realizations of phononic materials in different scales and dimensions are illustrated. Mathematical models for simplified phononic systems -in the form of springs and masses- are formulated. The most important tools needed to analyze and elucidate the behavior of phononic materials, namely, the dispersion relation, the steady-state forced response and the wave propagation are presented. The challenges and benefits of the unit-cell topology optimization problem are discussed, as well as the potential impact of using phononic materials for flow control. The chapter then provides a literature synopsis pertaining to phononics and flow control in general. The chapter concludes with the thesis objectives and organization.

Chapter 2 starts by introducing the problem of 1D layered phononic crystal optimization. A deeper look into the relevant literature is presented. The dispersion calculation framework using the transfer matrix method is presented, and so is the optimization mathematical model. The unit-cell representation and its advantages are highlighted. Four different objective functions are then considered; these are defined as (1) maximum attenuation at a given frequency, (2) minimum transmissibility for a given frequency range, (3) maximum width of the first band gap relative to its central frequency, and (4) maximum sum of the width of the first ten band gaps relative to their

central frequencies. To follow, new genetic algorithm operators that better suit the given problems are developed and shown to produce better performing designs, compared to the literature, for the first two objectives. No relevant comparisons are conducted in the literature for objectives 3 and 4, particularly for a layered 1D phononic material. However, the results reported for objective 3 are surprisingly and qualitatively unexpected. The results of objective 4 follow a trend similar to objectives 1 and 2, which provide insights and raise interesting questions about the results of objective 3.

As a logical evolution of the work presented in Chapter 2, the problem of unit-cell optimization is investigated for both two and three-dimensions in Chapter 3. The related literature to the problem is discussed and a motivation for the selected objectives functions is drawn. A description of the models considered is then followed. The plane-strain and Mindlin plate models are used and attention is focused on high-symmetry square lattices. The governing equations for waves propagating in-plane, out-of-plane and flexural modes are provided. A newly developed *lead-follow* genetic algorithm, one that is optimized for the problem in hand, is thoroughly explained. Record values are obtained for relative band gap size for (1) in-plane waves, (2) out-of-plane waves, (3) combined in-plane and out-of-plane waves, and (4) flexural waves.

Chapter 4 addresses the second part of the thesis that relates to the design of elastic meta-materials with superior band-gap characteristics. The chapter starts with an introduction to the shortcomings of existing concepts to band gap opening in the subwavelength regime, followed by a brief survey of the literature on acoustic/elastic metamaterial in general. The proposed design concept, a *trampoline metamaterial*, is then introduced. This concept is based on increasing the compliance of the base of a pillared plate by adding holes to significantly increase the relative band-gap size. The advantage of this design approach is that it avoids the need to increase the total mass of the system, as mostly done in earlier studies based on plate-based locally resonant elastic metamaterials. Different hole sizes and pillar heights are investigated to compare the trampoline metamaterial performance to a conventional locally resonant elastic metamaterial. The proposed novel, yet simple, design concept leads to the opening of a full band gap in frequency ranges where

no band gap exists in the equivalent conventional metamaterials. It also increases the band gap size by a factor of four along a certain direction.

The third part of the thesis presents a new application for phononics. Chapter 5 investigates the use of phononic materials to induce a desirable change in the behavior of a wall-bounded fluid flow. This work is conducted as part of a collaboration between the groups of Professors M. I. Hussein and S. Biringen. The study consisted of two parts. The first is to design and analyze a phononic crystal in isolation from the flow following a criterion pertaining to the phase response within a stop band versus a pass band and the influence of symmetry breaking as the crystal is truncated. The main tenet of the criterion requires that a stop-band to be utilized for flow stabilization and a pass-band for flow destabilization. The second is to couple the designed phononic crystal to a channel flow via an elastic interface, and simulate the response of intentionally introduced unstable waves within the flow. Using direct numerical simulations and a conventional serial staggered approach for the coupling, excellent agreement between the uncoupled and coupled results is observed. The advantage of offline design and tunability provides a profound savings in computational cost which opens the door for practical research and development for industrial applications.

To demonstrate the validity of the approach, three cases regarding channel-flow instability control are investigated. In all three, a portion of the bottom wall of the channel is replaced with a *phononic subsurface.* The performance of each configuration is subsequently measured by the amount of reduction/increase in perturbation kinetic energy against a control case where the rigid wall is kept. In the first case, a 2D unstable disturbance (a Tollmien-Schlichting wave) is injected into a flow at a given frequency. A significant reduction of up to 24% in the perturbation KE is recorded when a phononic subsurface (design A) is installed following the prior specified design criterion. The ability to destabilize is also demonstrated. The second case extends the first problem to 2D multi-frequency control to mimic more realistic situations, where more than one unstable frequency is present. To account for the wide range of these unstable frequencies a new phononic crystal is designed (design B). Various combinations of designs A&B are tested and

their performance emerged exactly as predicted, demonstrating robustness in the analysis/design methodology. Case 3 is a natural progression of the previous two cases: three-dimensional nonlinear instability control. In this case, a variation of disturbances along the span of the channel is allowed thus making profound nonlinear frequency harmonic generation inevitable. Here, a new phononic crystal design is created to encompass the primary and the secondary unstable modes. Although, the secondary modes showed some spatial destabilization, an overall, aggregate reduction in the perturbation kinetic energy is observed. This collaborative study presents a road map for the utilization of phononic materials in flow control.

6.2   Future work

Although the work accomplished in this thesis fills some voids in the literature, it opens the door wide open for future work in different disciples and scales.

- The layered 1D optimization framework is highly applicable to both photonic and phoXonic crystals. After formulating the problem in a manner that produces globally optimal results, one can draw new conclusions about the physics of the problem.

- Although the 2D and 3D optimization studies revealed designs with record values, discrete representations of decision variables are subsets of the continuous design space. Therefore, combining a global optimization method with continuous variables has the potential to reveal the globally optimal unit cell design for each of the considered objectives.

- To prove the optimality of the emerged designs, one needs to formulate the mathematical bounds of the problem. One way to do so is to use the Rayleigh-Ritz approach and the method of intermediate eigenvalue problems.

- The proposed trampoline concept shall facilitate the utilization of metamaterials in mass-sensitive applications (e.g., aerospace industry). Therefore, for commercial implementation, a trade-off optimization study relating mass/load-bearing capacity/band gap size is a logical next step.

- The trampoline metamaterial configuration can serve as a fertile base model to study and understand the coupling and dispersion hybridization within different types of lattice symmetries, e.g., square versus hexagonal, and the possibility to influence Bragg-scattering and thus possibly open band gaps that mix with those associated with local resonances.

- The work presented in Chapter 5 only scratches the surface of flow control using sub-surface phononic crystals. From the solid prospective, the problem is begging for two- and three-dimensional unit cell designs. One natural step towards the commercialization of this approach is to use smaller designs by incorporating metamaterials concepts (e.g., trampoline). This should facilitate changing the designs in both the span- and streamwise directions.

- On the fluid side, different problems related to separation and turbulence control should be investigated. In addition, boundary layers and different configurations of the channel are viable problems to be explored. Finally, experimental verification will be needed and highly anticipated.

Bibliography

[1] Mahmoud I Hussein, Michael J Leamy, and Massimo Ruzzene. Dynamics of phononic materials and structures: Historical origins, recent progress, and future outlook. Applied Mechanics Reviews, 66(4):040802, 2014.

[2] Martin Maldovan. Sound and heat revolutions in phononics. Nature, 503(7475):209–217, 2013.

[3] Mahmoud I Hussein and Michael J Frazier. Metadamping: An emergent phenomenon in dissipative metamaterials. Journal of Sound and Vibration, 332(20):4767–4774, 2013.

[4] Osama R Bilal, Mohammed A El-Beltagy, and Mahmoud I Hussein. Topologically evolved photonic crystals: Breaking the world record in band gap size. In SPIE Smart Structures and Materials+ Nondestructive Evaluation and Health Monitoring, pages 834609–834609. International Society for Optics and Photonics, 2012.

[5] G Floquet. Sur les equations differentielles lineaires. Ann. ENS [2], 12:47–88, 1883.

[6] MM Sigalas and EN Economou. Elastic and acoustic wave band structure. Journal of Sound and Vibration, 158(2):377–382, 1992.

[7] Manvir S Kushwaha, P Halevi, L Dobrzynski, and B Djafari-Rouhani. Acoustic band structure of periodic elastic composites. Physical Review Letters, 71(13):2022, 1993.

[8] ZY Liu, XX Zhang, YW Mao, YY Zhu, ZY Yang, CT Chan, and P Sheng. Locally resonant sonic materials. Science, 289(5485):1734–1736, 2000.

[9] M Sigalas and EN Economou. Band structure of elastic waves in two dimensional systems. Solid State Communications, 86(3):141–143, 1993.

[10] Yan Pennec, B Djafari-Rouhani, JO Vasseur, Abdelkrim Khelif, and PA Deymier. Tunable filtering and demultiplexing in phononic crystals with hollow cylinders. Physical Review E, 69(4):046608, 2004.

[11] Mahmoud I Hussein, Gregory M Hulbert, and Richard A Scott. Hierarchical design of phononic materials and structures. In ASME 2005 International Mechanical Engineering Congress and Exposition, pages 163–172. American Society of Mechanical Engineers, 2005.

[12] M. I. Hussein, K. Hamza, G. M. Hulbert, R. A. Scott, and K. Saitou. Multiobjective evolutionary optimization of periodic layered materials for desired wave dispersion characteristics. Struct. Multidiscip. Optim., 31(1):60–75, 2006.

[13] MM Sigalas. Elastic wave band gaps and defect states in two-dimensional composites. The Journal of the Acoustical Society of America, 101(3):1256–1261, 1997.

[14] M Torres, FR Montero de Espinosa, D Garcia-Pablos, and N Garcia. Sonic band gaps in finite elastic media: Surface states and localization phenomena in linear and point defects. Physical Review Letters, 82(15):3054, 1999.

[15] A. Khelif, A. Choujaa, S. Benchabane, B. Djafari-Rouhani, and V. Laude. Guiding and bending of acoustic waves in highly confined phononic crystal waveguides. Applied physics letters, 84(22):4400–4402, 2004.

[16] F Cervera, L Sanchis, JV Sanchez-Perez, R Martinez-Sala, C Rubio, F Meseguer, C López, D Caballero, and J Sánchez-Dehesa. Refractive acoustic devices for airborne sound. Physical review letters, 88(2):023902, 2001.

[17] Xiangdong Zhang and Zhengyou Liu. Negative refraction of acoustic waves in two-dimensional phononic crystals. Applied Physics Letters, 85(2):341–343, 2004.

[18] S.X. Yang, J.H. Page, Z.Y. Liu, M.L. Cowan, C.T. Chan, and P. Sheng. Focusing of sound in a 3d phononic crystal. Physical Review Letters, 93:024301, 2004.

[19] Liang-Shan Chen, Chao-Hsien Kuo, and Zhen Ye. Acoustic imaging and collimating by slabs of sonic crystalsmade from arrays of rigid cylinders in air. Applied physics letters, 85(6):1072–1074, 2004.

[20] J. Christensen, A I. Fernandez-Dominguez, F. de Leon-Perez, L. Martin-Moreno, and F J. Garcia-Vidal. Collimation of sound assisted by acoustic surface waves. Nat. Phys., 3(12):851–852, 2007.

[21] Kin Ming Ho, Chun Kwong Cheng, Z Yang, XX Zhang, and Ping Sheng. Broadband locally resonant sonic shields. Applied physics letters, 83(26):5566–5568, 2003.

[22] Sébastien Guenneau, Alexander Movchan, Gunnar Pétursson, and S Anantha Ramakrishna. Acoustic metamaterials for sound focusing and confinement. New Journal of physics, 9(11):399, 2007.

[23] Muralidhar Ambati, Nicholas Fang, Cheng Sun, and Xiang Zhang. Surface resonant states and superlensing in acoustic metamaterials. Physical Review B, 75(19):195447, 2007.

[24] Steven A Cummer and David Schurig. One path to acoustic cloaking. New Journal of Physics, 9(3):45, 2007.

[25] D. Torrent and J. Sánchez-Dehesa. Acoustic cloaking in two dimensions: A feasible approach. New J. Phys., 10:063015, 2008.

[26] M. I. Hussein, G. M. Hulbert, and R. A. Scott. Tailoring of wave propagation characteristics in periodic structures with multilayer unit cells. In Proc. 17th American Soc. Composites Tech. Conf., West Lafayette, Indiana, pages CD–ROM 1–9, October 2002.

[27] O. Sigmund. Microstructural design of elastic band gap structures. In Proceedings of the 2nd World Congress on Structural Multidisciplinary Optimization, Dalian, China, pages CD–ROM. Liaoning Electronic Press, Liaoning, China, 2001.

[28] O. Sigmund and J.S. Jensen. Systematic design of phononic band-gap materials and structures by topology optimization. Philosophical Transactions: Mathematical, Physical and Engineering Sciences, pages 1001–1019, 2003.

[29] A. R. Diaz, A. G. Haddow, and L. Ma. Design of band-gap grid structures. Struct. Multidiscip. O., 29(1):418–431, 2005.

[30] S. Halkjaer, O. Sigmund, and J. S. Jensen. Maximizing band gaps in plate structures. Struct. Multidiscip. O., 32:263–275, 2006.

[31] G. A. Gazonas, D. S. Weile, R. Wildman, and A. Mohan. Genetic algorithm optimization of phononic bandgap structures. Int. J. Solids Struct., 43(18-19):5851–5866, 2006.

[32] M.I. Hussein, K. Hamza, G.M. Hulbert, and K. Saitou. Optimal synthesis of 2D phononic crystals for broadband frequency isolation. Waves in Random and Complex Media, 17:491–510, 2007.

[33] L. Shen, Z. Ye, and S. He. Design of two-dimensional photonic crystals with large absolute band gaps using a genetic algorithm. Physical Review B, 68(3):1864, 2003.

[34] S. Preble, M. Lipson, and H. Lipson. Two-dimensional photonic crystals designed by evolutionary algorithms. Applied Physics Letters, 86:061111, 2005.

[35] M.A. El-Beltagy and M.I. Hussein. Design space exploration of multiphase layered phononic materials via natural evolution. In Proceedings of IMECE. ASME International Mechanical Engineering Congress and Exposition, Chicago, Illinois, 2006.

[36] Osama R Bilal and Mahmoud I Hussein. Topologically evolved phononic material: Breaking the world record in band gap size. In Society of Photo-Optical Instrumentation Engineers (SPIE) Conference Series, volume 8269, page 12, 2012.

[37] M Gad-el Hak. Flow control: Passive, active and reactive flow management, 2000.

[38] Maurizio Quadrio. Drag reduction in turbulent boundary layers by in-plane wall motion. Philosophical Transactions of the Royal Society A: Mathematical, Physical and Engineering Sciences, 369(1940):1428–1442, 2011.

[39] William S Saric, Andrew L Carpenter, and Helen L Reed. Passive control of transition in three-dimensional boundary layers, with emphasis on discrete roughness elements. Philosophical Transactions of the Royal Society A: Mathematical, Physical and Engineering Sciences, 369(1940):1352–1364, 2011.

[40] Max O Kramer. Boundary-layer stabilization by distributed damping, 1957.

[41] T Brooke Benjamin. The threefold classification of unstable disturbances in flexible surfaces bounding inviscid flows. Journal of Fluid Mechanics, 16(03):436–450, 1963.

[42] E. F. Blick C. W. Bert T. D. Reed R. W. Walters R. N. Wares. Aerodynamic drag reduction using compliant coatings. Proc. Okla. Acad. Sci, 1968.

[43] PW Carpenter and AD Garrad. The hydrodynamic stability of flow over kramer-type compliant surfaces. part 1. tollmien-schlichting instabilities. Journal of Fluid Mechanics, 155:465–510, 1985.

[44] PW Carpenter and AD Garrad. The hydrodynamic stability of flow over kramer-type compliant surfaces. part 2. flow-induced surface instabilities. Journal of Fluid Mechanics, 170:199–232, 1986.

[45] Q. Du, V. Faber, and M. Gunzburger. Centroidal voronoi tessellations: Applications and algorithms. SIAM review, 41(4):637–676, 1999.

[46] KS Yeo. The stability of boundary-layer flow over single-and multi-layer viscoelastic walls. Journal of Fluid Mechanics, 196:359–408, 1988.

[47] BN Semenov. On conditions of modelling and choice of viscoelastic coatings for drag reduction. In Recent developments in turbulence management, pages 241–262. Springer, 1991.

[48] Peter W Carpenter. Optimization of multiple-panel compliant walls for delay of laminar-turbulent transition. AIAA journal, 31(7):1187–1188, 1993.

[49] K-S Choi, X Yang, BR Clayton, EJ Glover, M Atlar, BN Semenov, and VM Kulik. Turbulent drag reduction using compliant surfaces. Proceedings of the Royal Society of London. Series A: Mathematical, Physical and Engineering Sciences, 453(1965):2229–2240, 1997.

[50] Christopher Davies and Peter W Carpenter. Numerical simulation of the evolution of tollmien–schlichting waves over finite compliant panels. Journal of Fluid Mechanics, 335:361–392, 1997.

[51] L Sirovich and S Karlsson. Turbulent drag reduction by passive mechanisms. Nature, 388(6644):753–755, 1997.

[52] Jens HM Fransson, Alessandro Talamelli, Luca Brandt, and Carlo Cossu. Delaying transition to turbulence by a passive mechanism. Physical review letters, 96(6):064501, 2006.

[53] Kwing-So Choi. Near-wall structure of a turbulent boundary layer with riblets. Journal of fluid mechanics, 208:417–458, 1989.

[54] Douglas C Chu and George Em Karniadakis. A direct numerical simulation of laminar and turbulent flow over riblet-mounted surfaces. Journal of Fluid Mechanics, 250:1–42, 1993.

[55] D Goldstein, R Handler, and L Sirovich. Direct numerical simulation of turbulent flow over a modeled riblet covered surface. Journal of Fluid Mechanics, 302:333–376, 1995.

[56] Brian Dean and Bharat Bhushan. Shark-skin surfaces for fluid-drag reduction in turbulent flow: a review. Philosophical Transactions of the Royal Society A: Mathematical, Physical and Engineering Sciences, 368(1929):4775–4806, 2010.

[57] Philippe R Spalart and J Douglas McLean. Drag reduction: Enticing turbulence, and then an industry. Philosophical Transactions of the Royal Society A: Mathematical, Physical and Engineering Sciences, 369(1940):1556–1569, 2011.

[58] Sheng Xu, D Rempfer, and J Lumley. Turbulence over a compliant surface: Numerical simulation and analysis. Journal of Fluid Mechanics, 478:11–34, 2003.

[59] PR Bandyopadhyay, C Henoch, JD Hrubes, BN Semenov, AI Amirov, VM Kulik, AG Malyuga, K-S Choi, and MP Escudier. Experiments on the effects of aging on compliant coating drag reduction. Physics of Fluids (1994-present), 17(8):085104, 2005.

[60] BN Semenov, AI Amirov, VM Kulik, and AG Malyuga. Experimental studies of compliant coatings for reduction of turbulent friction. Thermophysics and Aeromechanics, 14(1):133–142, 2007.

[61] Osama R Bilal, Mohammed A El-Beltagy, and Mahmoud I Hussein. Optimal design of periodic timoshenko beams using genetic algorithms. In 52nd AIAA/ASME/ASCE/AHS/ASC Structures, Structural Dynamics and Materials Conference, 2011.

[62] Osama R Bilal and Mahmoud I Hussein. Ultrawide phononic band gap for combined in-plane and out-of-plane waves. Physical Review E, 84(6):065701, 2011.

[63] Osama R Bilal and Mahmoud I Hussein. Trampoline metamaterial: Local resonance enhancement by springboards. Applied Physics Letters, 103(11):111901, 2013.

[64] M.I. Hussein and M.A. El-Beltagy. Optimization of phononic filters via genetic algorithms. In Journal of Physics: Conference Series, volume 92, page 012110. Institute of Physics Publishing, 2007.

[65] A. J. H. McGaughey, M. I. Hussein, E. S. Landry, M. Kaviany, and G. M. Hulbert. Phonon band structure and thermal transport correlation in a layered diatomic crystal. Phys. Rev. B, 74:104304, 2006.

[66] E. S. Landry, M. I. Hussein, and A. J. H. McGaughey. Complex superlattice unit cell designs for reduced thermal conductivity. Phys. Rev. B, 77:184302, 2008.

[67] C. Chen, A. Sharkway, S. Shi, and D. Prather. Synthesis of 2-dimensional photonic crystals. Optics Express, 11(4):317–323, 2003.

[68] M.A. El-Beltagy and M.I. Hussein. Evolutionary scale-preserving and repair-free operators for the design of layered composite materials for vibration and shock isolation. In Proceedings of the 7th International Conference on Production Engineering and Design for Development, Ain Shams University, Cairo, Egypt, pages 277–287, 2006.

[69] Osama R Bilal and Mahmoud I Hussein. Optimization of phononic crystals for the simultaneous attenuation of out-of-plane and in-plane waves. In ASME 2011 International Mechanical Engineering Congress and Exposition, pages 969–972. American Society of Mechanical Engineers, 2011.

[70] M. I. Hussein, G. M. Hulbert, and R. A. Scott. Dispersive elastodynamics of 1d banded materials and structures: design. J. Sound Vib., 307:865–893, 2007.

[71] I. El-Kady, R. H. Olsson III, and J. G. Fleming. Phononic band-gap crystals for radio frequency communications. Appl. Phys. Lett., 92:233504, 2008.

[72] S. Mohammadi, A. A. Eftekhar, W. D. Hunt, and A. Adibi. High-q micromechanical resonators in a two-dimensional phononic crystal slab. Appl. Phys. Lett., 94:051906, 2009.

[73] X. F. Li, X. Ni, L. A. Feng, M. H. Lu, C. He, and Y. F. Chen. Tunable unidirectional sound propagation through a sonic-crystal-based acoustic diode. Phys. Rev. Lett., 106:084301, 2011.

[74] M. Eichenfield, J. Chan, R. M. Camacho, K. J. Vahala, and O. Painter. Optomechanical crystals. Nature, 462(7269):78–82, 2009.

[75] N. Cleland, D. R. Schmidt, and C. S. Yung. Thermal conductance of nanostructured phononic crystals. Phys. Rev. B, 64:172301, 2001.

[76] J. K. Yu, S. Mitrovic, D. Tham, J. Varghese, and J. R. Heath. Reduction of thermal conductivity in phononic nanomesh structures. Nat. Nanotechnol., 5(10):718–721, 2010.

[77] P. E. Hopkins, C. M. Reinke, M. F. Su, R. H. Olsson III, E. A. Shaner, Z. C. Leseman, J. R. Serrano, L. M. Phinney, and I. El-Kady. Reduction in the thermal conductivity of single crystalline silicon by phononic crystal patterning. Nano Lett., 2011.

[78] R. H. Olsson III and I. El-Kady. Microfabricated phononic crystal devices and applications. Meas. Sci. Technol., 20:012002, 2009.

[79] S. J. Cox and D. C. Dobson. Maximizing band gaps in two-dimensional photonic crystals. SIAM J. Appl. Math., 59:2108–2120, 1999.

[80] M. Burger, S. J. Osher, and E. Yablonovitch. Inverse problem techniques for the design of photonic crystals. IEICE T. Electron., E87C:258–265, 2004.

[81] J. S. Jensen and O. Sigmund. Topology optimization for nano-photonics. Lasers & Photonics Rev., 5:308–321, 2011.

[82] C. J. Rupp, A. Evgrafov, K. Maute, and M. L. Dunn. Design of phononic materials/structures for surface wave devices using topology optimization. Struct. Multidiscip. O., 34(2):111–121, 2007.

[83] A. El-Sabbagh, W. Akl, and A. Baz. Topology optimization of periodic mindlin plates. Finite Elements in Analysis and Design, 44(8):439–449, 2008.

[84] M. Maldovan and E. L. Thomas. Simultaneous localization of photons and phonons in two-dimensional periodic structures. Appl. Phys. Lett., 88:251907, 2006.

[85] C. M. Reinke, M. F. Su, R. H. Olsson III, and I. El-Kady. Realization of optimal bandgaps in solid-solid, solid-air, and hybrid solid-air-solid phononic crystal slabs. Appl. Phys. Lett., 98:061912, 2011.

[86] Osama R Bilal, Mohammed A El-Beltagy, Mohammed H Rasmy, and Mahmoud I Hussein. The effect of symmetry on the optimal design of two-dimensional periodic materials. In Informatics and Systems (INFOS), 2010 The 7th International Conference on, pages 1–7. IEEE, 2010.

[87] R D. Mindlin. Influence of rotatory inertia and shear on flexural motions of isotropic, elastic plates. J. Appl. Mech., 18:31–38, 1951.

[88] E Reissner. The effect of transverse shear deformation on the bending of elastic plates. J. Appl. Mech., 12:68–77, 1945.

[89] M. I. Hussein. Reduced bloch mode expansion for periodic media band structure calculations. Proc. R. Soc. A, 465(2109):2825, 2009.

[90] Qiong Guo, Osama R Bilal, and Mahmoud I Hussein. A fast method for electronic band structure calculations. In ASME 2011 International Mechanical Engineering Congress and Exposition, pages 575–579. American Society of Mechanical Engineers, 2011.

[91] D. fE. Goldberg. Genetic algorithms in search, optimization and machine learning. Addison-Wesley, 1989.

[92] M. S. Kushwaha. Classical band structure of periodic elastic composites. Int. J. Mod. Phys. B, 10(9):977–1094, 1996.

[93] O. Sigmund and K. Hougaard. Geometric properties of optimal photonic crystals. Phys. Rev. Lett., 100:153904, 2008.

[94] N. Men, N. C. Nguyen, R. M. Freund, K. M. Lim, P. A. Parrilo, and J. Peraire. Design of photonic crystals with multiple and combined band gaps. Phys. Rev. E, 83:046703, 2011.

[95] Jensen Li and CT Chan. Double-negative acoustic metamaterial. Physical Review E, 70(5):055602, 2004.

[96] Nicholas Fang, Dongjuan Xi, Jianyi Xu, Muralidhar Ambati, Werayut Srituravanich, Cheng Sun, and Xiang Zhang. Ultrasonic metamaterials with negative modulus. Nature materials, 5(6):452–456, 2006.

[97] Artur Ávila, Georges Griso, Bernadette Miara, and Eduard Rohan. Multiscale modeling of elastic waves: theoretical justification and numerical simulation of band gaps. Multiscale Modeling & Simulation, 7(1):1–21, 2008.

[98] Yiqun Ding, Zhengyou Liu, Chunyin Qiu, and Jing Shi. Metamaterial with simultaneously negative bulk modulus and mass density. Physical review letters, 99(9):093904, 2007.

[99] Bruce L Davis and Mahmoud I Hussein. Nanophononic metamaterial: Thermal conductivity reduction by local resonance. Physical review letters, 112(5):055505, 2014.

[100] Y Pennec, B Djafari-Rouhani, H Larabi, JO Vasseur, and AC Hladky-Hennion. Low-frequency gaps in a phononic crystal constituted of cylindrical dots deposited on a thin homogeneous plate. Physical Review B, 78(10):104105, 2008.

[101] Tsung-Tsong Wu, Zi-Gui Huang, Tzu-Chin Tsai, and Tzung-Chen Wu. Evidence of complete band gap and resonances in a plate with periodic stubbed surface. Applied Physics Letters, 93(11):111902, 2008.

[102] Hussein M. I., Biringen S., Bilal O. R., and Kucala A. Flow stabalization by subsurface phonons. Proceedings of the Royal Society of London. Series A: Mathematical, Physical and Engineering Sciences, Accepted 2015.

[103] Bilal O. R., Kucala A., Biringen S., and Hussein M. I. Three-dimensional flow control using phononic crystals. In preparation, 2015.

[104] Kucala A., Bilal O. R., Biringen S., and Hussein M. I. Multi-frequency flow control using phononic crystals. In preparation, 2015.

[105] MJ Walsh and AM Lindemann. Optimization and application of riblets for turbulent drag reduction. American Institute of Aeronautics and Astronautics, 1984.

[106] S. Biringen. Active control of transition by periodic suction-blowing. Physics of Fluids, 27(6):1345–1347, 1984.

[107] S. Biringen, W. E. Nutt, and M. J. Caruso. Numerical study of transition control by periodic suction blowing. AIAA Journal, 25(2):239–244, 1987.

[108] A. Kucala and S. Biringen. Spatial simulation of channel flow instability and control. J. Fluid Mech., 738:105–123, 2014.

[109] Dennis M Bushnell, Jerry N Hefner, and Robert L Ash. Effect of compliant wall motion on turbulent boundary layers. Physics of Fluids (1958-1988), 20(10):S31–S48, 1977.

[110] Walter Tollmien. Über die entstehung der turbulenz. 1. mitteilung. Nachrichten von der Gesellschaft der Wissenschaften zu Göttingen, Mathematisch-Physikalische Klasse, 1929:21–44, 1928.

[111] G. Danabasoglu, S. Biringen, and C. L. Streett. Spatial simulation of instability control by periodic suction blowing. Phys. of Fluids A, 3(9):2138–2147, 1991.

[112] E. M. Saiki, S. Biringen, G. Danabasoglu, and C. L. Streett. Spatial simulation of secondary instability in plane channel flow: Comparison of K- and H-type disturbances. J. Fluid Mech., 253:485–507, 1993.

[113] W. C Reynolds. Orrsom: A Fortran-IV program for solution of the OrrSommerfeld equation. Technical report, Stanford University, 1969.